THE GEOMETRY OF TERRESTRIAL LASER SCANNING

IDENTIFICATION OF ERRORS, MODELING AND MITIGATION OF SCANNING GEOMETRY

THE GEOMETRY OF TERRESTRIAL LASER SCANNING

IDENTIFICATION OF ERRORS, MODELING AND MITIGATION OF SCANNING GEOMETRY

Proefschrift

ter verkrijging van de graad van doctor
aan de Technische Universiteit Delft,
op gezag van de Rector Magnificus prof. ir. K. C. A. M. Luyben,
voorzitter van het College voor Promoties,
in het openbaar te verdedigen op 5 januari 2016 om 12:30 uur

door

Sylvie Shoba SOUDARISSANANE (DIJKSTRA)

Master of Science in Digital Communications
Master of Science in Telecommunications and Signal Processing
geboren te Orléans, France.

Dit proefschrift is goedgekeurd door de:

Promotoren: Prof. Dr. Dr.h.c. ir. P. J. G. Teunissen en Prof. Dr. M. Menenti
Copromotor: Dr. R. C. Lindenbergh

Samenstelling promotiecommissie:

Rector Magnificus,	voorzitter
Prof. Dr. Dr.h.c. ir. P. J. G. Teunissen,	Technische Universiteit Delft
Prof. Dr. M. Menenti,	Technische Universiteit Delft
Dr. R. C. Lindenbergh,	Technische Universiteit Delft

Onafhankelijke leden:

Prof. Dr. PEng D. Lichti,	University of Calgary
Prof. Dipl. -ing. Dr. techn. N. Pfeiffer,	Technische Universität Wien
Prof. Dr. ir. P. J. M. van Oosterom,	Technische Universiteit Delft
Prof. Dr. ir. J. Stoter,	Technische Universiteit Delft
Dr. H. Ledoux,	Technische Universiteit Delft

Keywords: Terrestrial Laser Scanning, scanning geometry, incidence angle, range, point cloud, quality, error budget, placement algorithm

Printed by: GILDEPRINT

Front & Back: Abstract illustration of the visibility polygons from instruments viewpoints.

ISBN 978-94-6233-203-4

An electronic version of this dissertation is available at
`http://repository.tudelft.nl/`.

Contents

Preface

> “It is good to have an end to journey toward; but it is the journey that matters, in the end.”
>
> Ernest Hemingway

This great (long) journey comes to an end ... and what a journey!

It all started with a phone interview that took place when I was in a train to go to Stockholm during the cold winter of 2006. From that moment on, I knew this journey was going to be the most amazing experience of my life. And I can say it now .. it is really the most amazing! In March 2007, I started my PhD studies at TU Delft, The Netherlands, right after successfully defending the thesis of my second MSc degree in Chalmers University of Technology, Sweden. I was young, and not yet ready to start a career in a company as an engineer. I wanted to stay in the academic world. I knew there was still a lot for me to learn. This PhD study not only taught me a great deal on Laser Scanners and error budgeting, but also a lot on a personal level. Throughout my studies I traveled around the world to gain knowledge in my field and extend my network. The results of the research of my PhD during the few years that passed since this phone interview are described in this booklet. I am proud to share the knowledge I gained in such a concise way.

The journey to the completion of my PhD was not the most straightforward and easy. Many people have made a contribution to this thesis, directly and indirectly, which enabled me to successfully finish this work. I am sincerely grateful to all of them.

First of all, I would like to thank my daily supervisor: Dr. Roderik Lindenbergh. He is an exceptional supervisor, teacher and researcher, a model to be followed. His dedication and commitment are definitely out of normal, and I am forever thankful for that. He was always available to answer any of my questions. His scientific knowledge and advices put me back to the right path when I would go wild on my ideas. He often helped me seeing the light when everything was dark. We had a lot of fun working together on various projects. Roderik, thank you for your help, encouragement and support during all those years.

I would like to thank my promotor Prof. Dr. Massimo Menenti for his support and guidance during this research. His experience with dealing with PhD students proved to be extremely valuable with my own PhD thesis. His structured way of thinking and broad range of knowledge made our discussions insightful. He could always organize my thoughts so I could structure them better in my thesis. Massimo, thank you.

I also want to thank my promotor Prof. Dr. Peter Teunissen. I was able to pursue my research with great freedom, with not so many objections from him. He often challenged me with difficult questions that made me think for a long time. His undoubted knowledge on Least-Squares and adjustment theory was valuable to my research. Peter, thank you.

I am also thankful to 'hidden helpers', as Rebeca Domingo and Lidwien de Jong. They arranged all the administrative paperworks seamlessly, and all the multiple extension contracts of my PhD. Of course, I wish to also thank all my (PhD) colleagues with whom I shared nice coffees and lunch breaks, the list is very long so I only mention a few here: Jochem, Corne, Kourosh, Elena, Prabu, Joana, Ali, Mahmut, Gert-Jan, Freek. Thank you all for making these few years as a PhD student so pleasant and fun!

A big thank you to all my friends here and there around the world, who followed my journey with the same passion as I did: Jean-Sebastien, Berenice, Lionel, Astrid, Helen, Thomas, Bas, Calvin, Jelmer, Care. Thank you for hearing all my complaints and supporting me in my quest for the diploma.

Without the unconditional love and support of my parents, I would never have been able to be who I am now. Thank you Maman and Papa for believing in me and for supporting me, no matter what. At the end, I almost reach this dream I always had ... BAC+19! Thank you for sacrificing everything you had so we could grow and reach out for the best.

To my beloved kids Lakshmi and Sanjay, who spent most of their 'mama-dag' at the creche, while I was working at the university: sorry that I didn't spend that much time with you, and thank you for being such treasures. Je vous aime.

The last person I would like to thank, is the most important person in my life. Arne, my best friend, soul-mate and love, thank you for your love and support during all these years. You lived this PhD journey as intensely I did. You were always able to cheer me up when I felt down. You sacrificed so much and gave me everything you could so I could complete this PhD. Thank you my dear love.

Summary

Over the past few decades, Terrestrial Laser Scanners are increasingly being used in a broad spectrum of applications, from surveying to civil engineering, medical modeling and forensics. Especially surveying applications require on one hand a quickly obtainable, high resolution point cloud but also need observations with a well described quality, from which it is possible to reliably derive the quality of the end-product. As any measurement, TLS scans are subject to measurement noise. Currently, the manufacturers provide documentation containing only global technical specifications including precision of measurements performed on reference surfaces under laboratory conditions.

After brief introduction of the principal of Laser Scanning, in this thesis an overview of the major quality influencing factors is provided, grouped in four main categories: (i.) scanner mechanism, (ii.) atmospheric conditions and environment, (iii.) object properties and (iv.) scanning geometry. In many cases, the user has limited control on the scanner mechanism, the atmospheric conditions or the object properties. The only factor on which the user has control on is the scanning geometry, as the user determines the scan location and thereby the view-point of a point cloud. This dissertation presents the research on the influence of scanning geometry on the point cloud quality. This thesis proposes a theoretical study of the scanning geometry effects on individual point quality, as well as practical assessments.

The impact of scanning geometry on individual point quality is analyzed, based on local planar features. The quality investigated in this thesis relates to the random errors or precision of individual points and does not deal with systematic errors or biases. Different planar fitting techniques are presented and compared. The quality of each local fit is described using a Least Squares estimation. The main quality describers used in this work are presented for each method.

By using these quality describers, the influence of the scanning geometry on the point quality is characterized both quantitatively and qualitatively. The scanning geometry is defined using two parameters: the incidence angle and the range. The incidence angle is defined as the angle between one laser beam vector and the normal vector to the surface. The range is defined as the distance between the scanner and the surface. It is shown that and how the received signal strength of the measurements decreases with increasing incidence angle and range. The presented approach allows the quantification of the contribution of noise induced by the scanning geometry, based solely on point cloud data. No additional or external measurements are needed. The contribution of the two scanning geometry parameters on the point quality has been quantified using contribution coefficients.

The effect of scanning geometry on the point quality is quantified and tested on a reference test board and two point clouds sampling a standard room. It is shown that the theoretical models developed are consistent with this experimental assessment. It is shown that it is possible to reduce the total error of the measurements by placing the scanner at another position in the room, which is not necessarily an obvious position.

Inspired by these results, a new method that determines near optimal view-points in a scene based on terrestrial laser scanner capabilities is presented. Using a simple approach, an improvement of the measurement set-up can be easily achieved using a small amount of computation, memory and time.

Samenvatting

De laatste decennia worden terrestrial laserscanners steeds vaker toegepast in steeds meer toepassingen. Van landmeting in de civiele techniek tot gebruik voor medische en forensische doeleinden. Met name landmeetkundige toepassingen vragen aan de ene kant om een snel verkrijgbare, hoge resolutie puntenwolk, maar aan de andere kant om waarnemingen met een goed gedocumenteerde kwaliteitsbeschijving die het mogelijk maakt ook de kwaliteit van afgeleide producten te beschrijven. Zoals elke meting, zijn ook laser scans onderhevig aan meetfouten. Momenteel verstrekken producenten slechts algemene technische specificaties, gebaseerd op metingen verricht op referentievlakken onder laboratorium condities.

Na een korte introductie van de beginselen van laserscannen, geeft dit proefschrift een overzicht van de belangrijkste factoren die de kwaliteit van een scan beïnvloeden. Dit overzicht is onderverdeeld in vier groepen: (i.) mechaniek van de scanner, (ii.) atmosferische condities en de omgeving, (iii.) eigenschappen van het object en (iv.) scangeometrie. In de meeste gevallen kan de gebruiker slechts beperkt invloed uitoefenen op het mechaniek van de scanner, de atmosferische condities of de eigenschappen van het te scannen object. De enige factor die de gebruiker wel kan beïnvloeden, is de scangeometrie, doordat de gebruiker de opstelplaats van de scanner bepaald en daarmee de positie van de scanner ten opzichte van de te scannen objecten. Dit proefschrift presenteert het onderzoek dat is verricht naar de invloed van de scangeometrie op de kwaliteit van de verkregen puntenwolk. Dit onderzoek beschrijft de theoretische effecten van de scangeometrie op de kwaliteit van individuele punten, en verifiëert deze effecten in de praktijk.

De invloed van de scangeometrie op de kwaliteit van een individueel punt wordt geanalyseerd op basis van de lokale eigenschappen van het gescande oppervlak. De kwaliteit die in dit proefschrift onderzocht wordt, heeft betrekking op zogenaamde toevallige meetfouten en niet op systematische meetfouten. Verschillende methodes voor het schatten van vlakken worden gepresenteerd en met elkaar vergeleken. De kwaliteit van elke lokale schatting wordt beschreven met behulp van kleinste kwadraten.

Door het gebruik van deze kwaliteitsaanduidingen wordt de invloed van de scangeometrie op de kwaliteit van de puntenwolk getypeerd, zowel kwantitatief als kwalitatief. De scangeometrie wordt gedefinieerd op basis van twee parameters: de invalshoek en het bereik. De invalshoek wordt gedefinieerd als de hoek tussen de vector van de laserstraal en de normaalvector van het oppervlak. Het bereik wordt gedefinieerd als de afstand tussen de scanner en het oppervlak. Er wordt aangetoond dat en hoe de terugontvangen sterkte van het meetsignaal afneemt wanneer de invalshoek en het bereik toenemen. De gepresenteerde aanpak maakt het mogelijk de invloed van de scangeometrie op de meetonnauwkeurigheid te kwantificeren. Deze aanpak is uitsluitend gebaseerd op de data

verkregen uit de puntenwolk. Additionele metingen of metingen met andere instrumenten zijn daarbij niet nodig. De invloed van de twee parameters op de kwaliteit van de punten wordt gekwantificeerd door middel van twee specifieke coefficienten.

Het effect van de scangeometrie op de kwaliteit van de punten wordt gekwantificeerd en getest op puntenwolken verkregen door het scannen van een testopstelling en een standaard kamer. Er wordt aangetoond dat de ontwikkelde theoretische modellen overeenkomen met de verrichte experimenten. Er wordt ook gedemonstreerd dat het mogelijk is de totale meetfout te reduceren door de scanner op een andere, niet altijd voor de hand liggende locatie in de kamer te plaatsen.

In navolging van deze resultaten wordt een nieuwe methode gepresenteerd waarmee bijna-optimale scanlocaties in een ruimte kunnen worden bepaald, afhankelijk van de prestaties van de gebruikte laserscanner. Door het volgen van een eenvoudige methode kan gemakkelijk een betere meetopstelling worden verkregen, zonder dat hier veel rekenkracht en rekentijd voor nodig is.

CHAPTER 1

Introduction

> *"Those who know, do. Those that understand, teach."*
>
> Aristotle

1.1 Laser scanning: background and applications

Traditional geodetic surveying instruments such as *e.g.* total station theodolite and Global Navigation Satellite System (GNSS) provide the acquisition of 3D coordinates of an object. However, these commonly used techniques often provide single measurements with a relatively slow acquisition process, and are often very limited in the range of applications. For instance, GNSS techniques cannot be used in indoor surveys as a clear visibility of satellites is required. When using a theodolite, the measurement of a fixed prism in the scene is required to obtain a precise measurement.

Light Detection And Ranging (LiDAR) systems such as Terrestrial Laser Scanners (TLS) are remote sensing systems that determine the distance to an object by analyzing a laser light return on an object's surface. This new generation surveying technique allows for extremely rapid acquisition of large amounts of 3D coordinates of objects' surfaces, with an unprecedented level of precision. A TLS makes possible to remotely survey areas that are complex or inaccessible to traditional surveying techniques.

Within a matter of minutes, a TLS mounted on a tripod captures the relative position of objects' surfaces in its line of sight as a 3D point cloud consisting of millions of (xyz) points and their respective intensity value i. In the past decade, this technology is increasingly being used in various engineering fields, see Table 1.1. However, the actual quality of a 3D point cloud is often not known. A variety of products are derived from

3D point clouds. The quality of these derived products depends on the quality of the acquired point clouds.

Civil Engineering	Infrastructure (bridge, road, building, indoor/outdoor, pipelines ...) Renovations (modification, additions, removal ...) 3D City models Deformation analysis (tunnels, bridges, dikes, buildings, ...)
Medical Engineering	Deformation analysis of body parts before/after surgery Orthodontia, prosthesis reconstructions and implants
Forensics	Crime scene documentation
Mechanical Engineering	Robotic control (scene scan for next position determination, indoor/outdoor navigation ...) Small mechanical parts quality control
Remote sensing	Deformation analysis (erosion, deposit of sediments, nature as forest, beach, ...) Change detection Classification
Film and game industry	3D models of real life objects for animation
Archeology	Archive scanning (Historical monuments and cultural heritage preservation/documentation ...) 3D visualisation models of archaeological sites

Table 1.1: *Examples of Terrestrial Laser Scanning applications.*

Two different measurement techniques are currently available [85, 44, 126], which basically use pulse or phase based measurements. An example of a laser scanner is shown in Fig. 1.1. A TLS is typically composed of two main parts: a rotating motor and a rotating mirror. The combination of two rotating elements enables the acquisition of panoramic views. In the case of the FARO LS880 as shown in Fig. 1.1(a), the head motor rotates 180° horizontally and the mirror motor rotates 180° vertically. The resulting point cloud covers almost 360° in both horizontal and vertical directions in the spherical domain.

At each horizontal angular rotation step, the mirror rotates with a regular vertical angular step and deflects laser beams towards a defined direction. The return of each laser ray that hits the surface of an object is measured in the direction of the emitted beam, as shown in Fig. 1.1(b). This way of measuring the position of an object surface provides huge amounts of data within a very short period of time. For instance, the TLS FARO LS880 captures about 125 000 points per second. The resulting point cloud is usually given in unorganized, *i.e.* not gridded, Cartesian coordinates. This particular scanner can be upgraded with a single-lens reflex (SLR) camera to enable the coloring of its point clouds. The software tool provided by the manufacturer corrects as much as possible the parallax and matches pixels obtained from the camera to the individual points in the 3D point cloud. Nowadays TLSs have integrated cameras located as close as possible to the laser emitting unit, which make the acquisition of colored point clouds very easy and almost seamless.

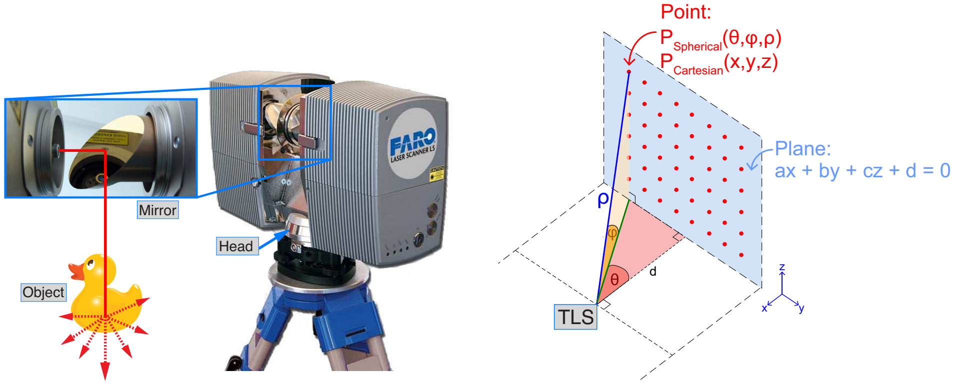

(a) FARO LS880 Phase based Terrestrial Laser Scanner

(b) Schematic representation of a point cloud acquisition. A point P is measured at the angular positions (θ,φ), with a range ρ.

Figure 1.1: *Terrestrial Laser Scanner example and principle.*

The terrestrial laser scanning technology is increasingly being used for representing and analyzing 3D objects in a wide range of surveying applications. One of the main applications of the terrestrial laser scanner is the visualization of 3D objects. The range of such 3D objects is extremely wide, going from a simple pipe in a oil rig to an entire city model. The TLS portability, combined with its ease of use, makes the number of applications that make use of TLSs growing fast.

An example of a 3D point cloud is shown in Fig. 1.2. In this view, the (x, y, z) points are colored following the intensity values i $(0$ to $1)$ measured by the TLS, and rendered following a custom RGB colormap to facilitate a better visualization. The TLS captures surfaces in its line-of-sight, which results in occluded areas, as shown in Fig. 1.2. In this example, one inevitable occlusion is shown: the TLS itself. Indeed, the scanner cannot scan surfaces right underneath itself as the head motor and tripod are always obstructing the view of surfaces located below the scanner. This obstruction is shown in Fig. 1.2 as the big occlusion circle on the floor. As another occlusion example, in Fig. 1.2, the person standing acts as an obstacle obstructing the view towards the containers in the background. Surfaces not in the direct line-of-sight of the TLS from one view-point can often be captured from a different view-point where they become visible to the TLS. As the full measurement of a scene is not instantaneously captured, moving objects are captured as-is at the moment a laser ray hits their surface, as shown in Fig. 1.2. In this example, a person was walking in the same direction as the TLS was rotating horizontally, which affects the shape of the person captured on the scan.

Especially surveying applications require on one hand a quickly obtainable, high resolution point cloud but also need observations with a known and well described quality, from which it is possible to reliably derive the quality of the end-product. A TLS is a very handy tool when modeling and monitoring man made structures like buildings, bridges, road infrastructures or tunnels, but also natural structures like trees, beaches or shallow water environments. As an example of use, to investigate the scale of morphodynamic changes affecting the beach topography, an experiment was designed to quantify sand transport

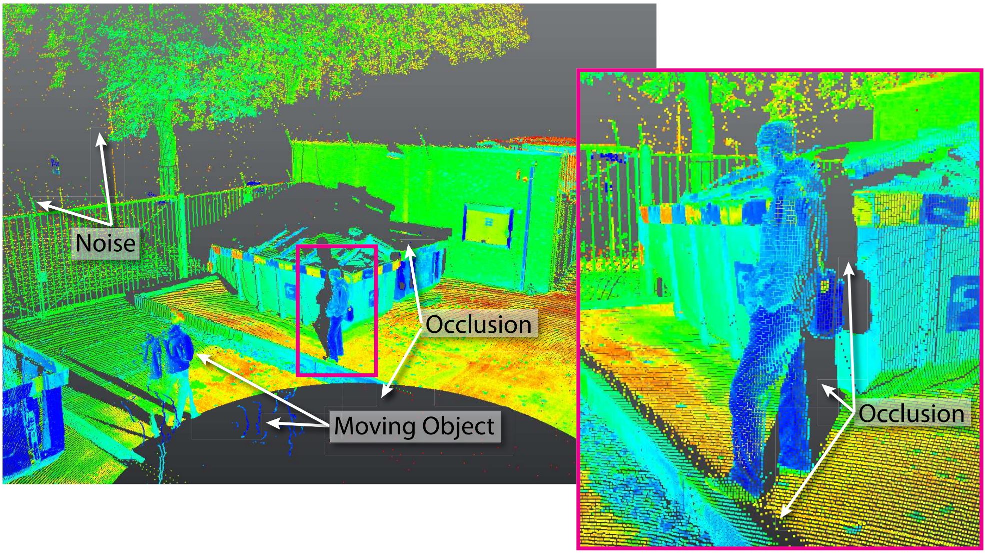

Figure 1.2: *Example of a* 3*D point cloud obtained with a TLS FARO LS880.*

as shown in Fig. 1.3. The experiment took place at a sandy beach about 15 km south of the city of The Hague in The Netherlands, at a location called Vlugtenburg. As shown in Fig. 1.3(a), at approximately 100 m from the high water line, a screen (10 m long and 1 m high) was erected. The topography was measured with the terrestrial laser scanner Faro Photon 120 during a period of 88 hours [99] as shown in Fig. 1.3(b). Various analyses of the point clouds were performed among which the sand volume changes per cubic meter as shown in Fig. 1.3(c).

1.2 Factors influencing the point cloud quality

As any measurement, TLS scans are subject to measurement noise. Currently, the manufacturers provide documentation containing only global technical specifications including precision of measurements performed on reference surfaces under laboratory conditions [85, 44, 126].

In practice, the scanning process can be affected by many influencing factors as shown in Fig. 1.4, which can be grouped in the following four main factors: (i.) scanner mechanism, (ii.) atmospheric conditions and environment, (iii.) object properties and (iv.) scanning geometry.

(i.) Scanner mechanism. This includes the hardware components misalignments, calibration, settings and the variations of the emitted laser beam properties and its detection process.

(ii.) Atmospheric conditions and environment. This incorporates the errors related to atmospheric conditions, *e.g.* humidity, temperature, and pressure variation. It also

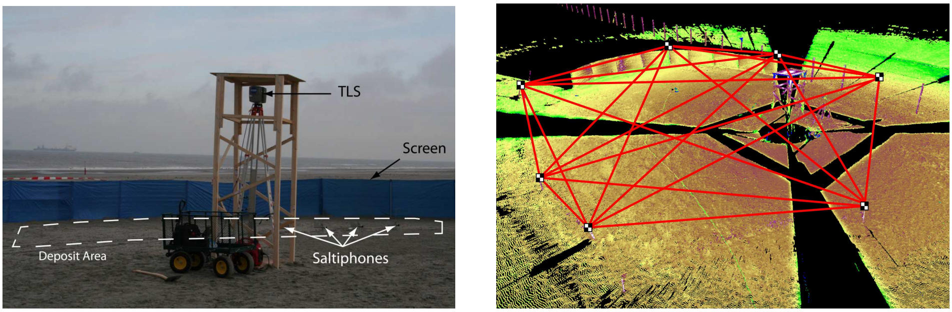

(a) Experiment setup: sand particles transported towards the plastic screen and the wooden house protecting the terrestrial laser scanner Faro Photon 120.

(b) Typical scanning geometry of a screen scan, point cloud colored with intensity, with the paper target locations and their respective baselines in red.

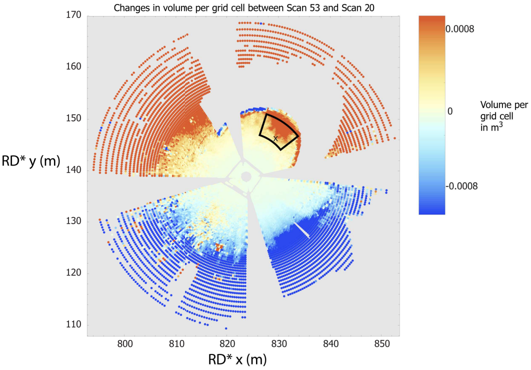

(c) Changes in volume in m^3 per grid cell between scan 53 at hour 48.3 and scan 20 at hour 16.

Figure 1.3: *Eolian beach sand transport monitored by TLS.*

takes into account the presence of ambient lighting in the scene, *e.g.* total darkness, artificial light or natural sunlight. The scanning environment is also taken into account, *e.g.* indoors, outdoors.

(iii.) Object properties. This influencing factor refers to the surface properties, *e.g.* reflectivity and roughness of the surface material with respect to the wavelength of the scanner.

(iv.) Scanning geometry. This influencing factors deals with the placement of the TLS relative to the location and orientation of the scanned surface, which determines the local incidence angle, the local range and the local point density of the laser points sampling the surface.

Additionally, automatic post-processing often realized during the capture, *e.g.* removing or filtering points according to a criterion, may also affect the quality of the overall point cloud. Further processing steps such as registration, segmentation or change detection will all profit from a sound quality description that allows for appropriate error propagation.

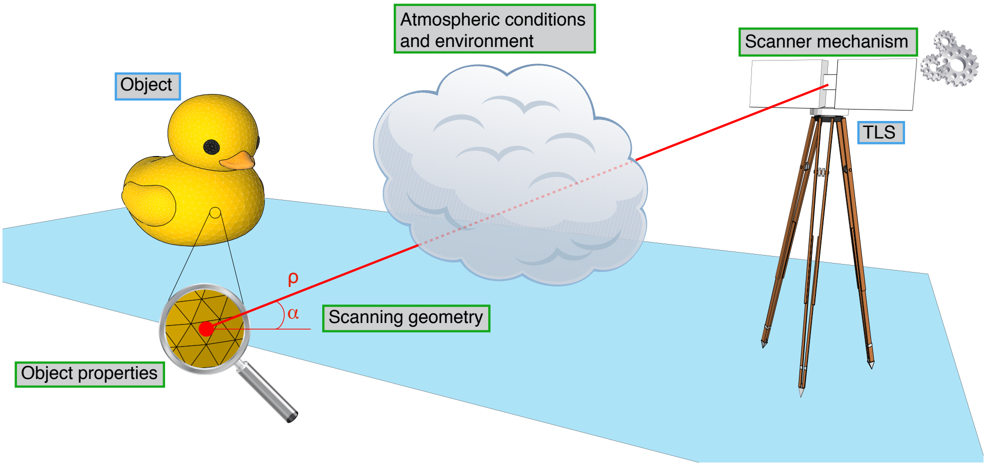

Figure 1.4: *3D point quality influencing factors. A single laser beam is depicted traveling through some atmospheric and environmental conditions and hitting the surface of an object at a distance ρ and incidence angle α from the TLS.*

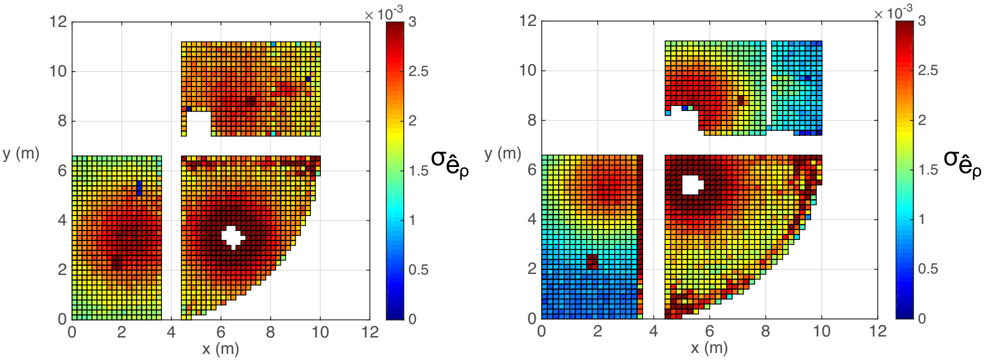

Figure 1.5: *Example of two placements of a TLS in one room. Net-view of Cartesian patches of 20×20 cm colored with noise level per patch.*

As a result, the noise level in a point cloud is different for every single point. To illustrate this, the example of a simple room is shown in Fig. 1.5, which is further discussed and analyzed in Chapter 5. The net-view of the acquisition of the room from two different view-points is shown, one in the center of the room and another one in the corner of the room. The points in each point cloud are first divided into small patches of 20×20 cm. A noise level per patch is derived by using planar fitting techniques. It is seen that by considering the same room, scanned with the same instrument at almost the same time (about 20 minutes apart), but from different view-points, the quality of the obtained point clouds is different.

1.3 Scope and limitations

All the presented factors influence the measurement of individual points, by possibly adding noise or distorting the intensity and shape of the emitted signal. To characterize the effects of the scanner mechanism on the point quality, the user should perform a thorough instrument calibration procedure, which is often costing a lot of time and is often not an easy procedure to follow. The calibration is most likely to be performed in near laboratory conditions, by means of reference objects like special coated calibrated surfaces or reference targets. In most engineering projects, the instrument is assumed to be properly calibrated and stable during a longer period of use. The TLS is assumed to be usable as-is and measures the surroundings following the specifications provided by the manufacturer.

The atmospheric and environmental conditions of the measurement set-ups are often very hard factors to regulate and predict. The user has very little or no control on this factor. The impact of this factor on the measurement quality can however become problematic for the acquisition process itself under extreme circumstances *e.g.* rain or very cold/hot temperatures as the TLS has physical measurement limitations. For instance, water droplets in rain or fog affect the laser beam light properties which results in wrongly measured points. Using the scanner in a too cold or too warm environment with respect to the specifications given by the manufacturer is not advised. However, some projects still require the acquisition of 3D point clouds under those extreme conditions, *e.g.* deformation monitoring on wet sandy beaches all year long, or historical monument mapping in a high ambient temperature.

The object properties are also an influencing factor on which the user has very little or no control. There exists coating sprays which cover the outer surface of an object with calibrated material such as Spectralon coating. In this way, specular surfaces such as objects made of glass or mirror-like metal, could be better scanned as the reflection on coated surface becomes more diffuse. However in practice, in most of the cases it is not possible to modify the material properties of an object. When scanning an old church for instance, the user cannot spray coat the entire building before scanning it.

In many cases, the user has limited control on the scanner mechanism factor, the atmospheric factor or the object properties factor. The only influencing factor on which the user has control is the scanning geometry, as the user determines the scan location and thereby the view-point of a point cloud. This dissertation presents the investigation of the identification, modeling and mitigation of one major point cloud quality influencing factor: the scanning geometry. This thesis proposes a theoretical study of the scanning geometry effects on individual point quality, as well as practical assessments of the developed contribution models.

In 2006, TU Delft acquired a laser scanner of its own: a FARO LS880. Most of the results presented in this thesis are based on scans obtained with this scanner. The focus of this thesis is placed on phased based scanners, although most of the theory presented here is applicable to most types of TLSs.

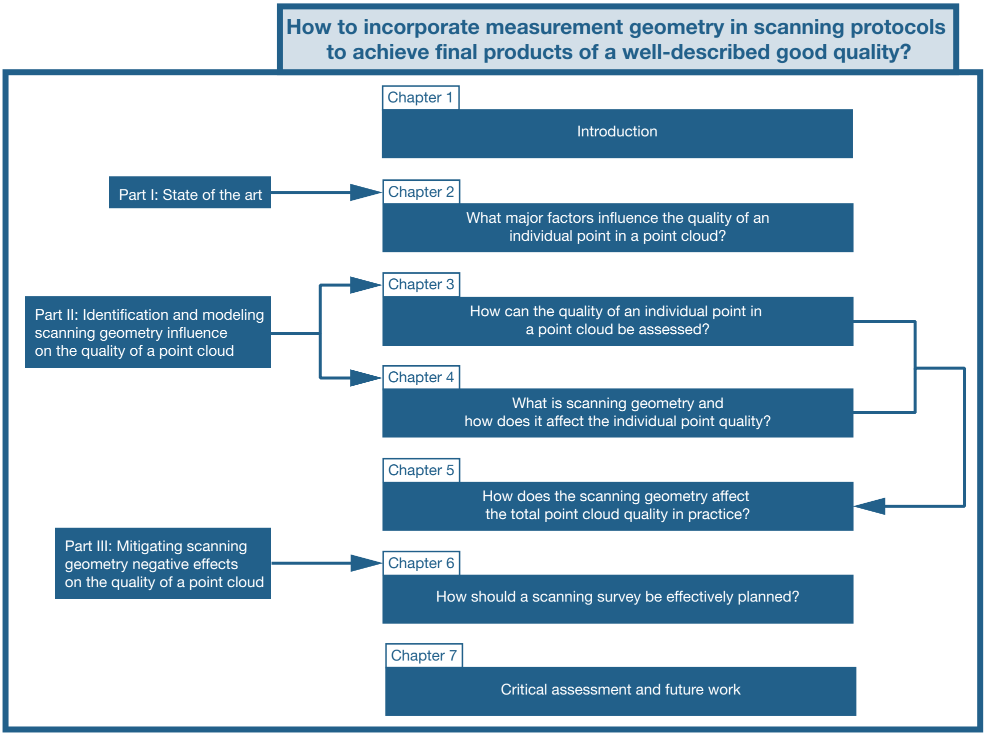

Figure 1.6: *Diagram of the thesis outline and the subquestions answered per chapter.*

1.4 Research Question

The main research question of this dissertation reads as follows:

> How to incorporate measurement geometry in scanning protocols to achieve final products of a well-described good quality?

The following subquestions are derived from the main research question:

(1.) What major factors influence the quality of an individual point in a point cloud?

(2.) How can the quality of an individual point in a point cloud be assessed?

(3.) What is scanning geometry and how does it affect the individual point quality?

(4.) How does the scanning geometry affect the total point cloud quality in practice?

(5.) How should a scanning survey be effectively planned?

1.5 Methodology in a nutshell

The investigation of the influence of the scanning geometry on the point cloud quality follows four main modules:

(i.) Identification. The major influencing factors on the point cloud quality as presented in Sec. 1.2 are investigated. The global impact of influencing factors on existing post-processing methods is presented in Chapter 2. The point cloud quality is being defined by using planar fitting methods as shown in Chapter 3.

(ii.) Modeling. The scanning geometry is first defined as being the range and incidence angle to the surface of an object in Chapter 4. A general approach to modeling negative effects due to the scanning geometry is provided based on planar features defined in Chapter 3.

(iii.) Quantification. The models of incidence angle and range are applied in real-life cases in Chapter 5. The quantification of the total errors is presented in a controlled set-up as well as a regular indoor room. The total error is significantly changing by moving the scanner from one view-point to another.

(iv.) Mitigation. A method is presented to determine necessary view-points that cover 2D areas of interest with a small number of view-points based on the floor plan of the area of interest in Chapter 6. The negative effects of scanning geometry presented in Chapter 4 are incorporated into this method as constraints. From those view-points, the area of interest is being fully covered given a maximum allowed range and incidence angle.

1.6 Thesis organization

An overview of the thesis organization and the relation of the chapters to the subquestions is presented in Fig. 1.6. The state of the art and general background on laser scanning is presented in Chapter 2. In this chapter, the principles of laser scanning as the range determination process and typical surveying procedures are presented. Major point cloud quality influencing factors are also presented. In Chapter 3, the assessment of the quality of a point cloud is presented using planar features. After presenting the propagation of errors of individual points, several planar fitting methods are presented. Chapter 4 proposes a definition of the scanning geometry and its implications on the amount of received signal. It also provides an approach that allows to quantify the contribution of noise induced by the scanning geometry, based only on point cloud data. The application of the proposed models is presented in Chapter 5, where real-life point clouds are analyzed. Chapter 6 presents an original method to determine near optimal view-points in a scene based on terrestrial laser scanner capabilities. The view-point of the laser scanner are determined such that the negative impact of scanning geometry on the point quality is minimized as much as possible. Chapter 7 concludes the thesis and provides recommendations on future work remaining to achieve a full error budget of Terrestrial Laser Scanning.

Part I

State of the art

Chapter 2

Principle of laser scanning

> *"Le savant doit ordonner ; on fait la science avec des faits comme une maison avec des pierres ; mais une accumulation de faits n'est pas plus une science qu'un tas de pierres n'est une maison."*
> "The Scientist must set in order. Science is built up with facts, as a house is with stones. But a collection of facts is no more a science than a heap of stones is a house"
>
> Henri Poincaré, Science and Hypothesis

Laser scanning is a remote sensing technology that allows 3D measurements of real-world objects. Distance measurements using laser light have already been in use since the 1970's [84]. However, the range determination methods used at that time were very expensive, unreliable and often realized on small-scale objects. Laser scanning technology became popular in the late 1990's thanks to the advances made in the field of computer sciences, notably the increase of data storage and processing capabilities, as well as more reliable and accurate range measurement techniques [62, 87]. These advances resulted in better laser scanners, with unprecedented acquisition time and large spatial coverage.

In this chapter, the following research question is investigated and answered:

What are the major influencing factors on the
quality of an individual point in a point cloud?

First, the principles of laser scanning will be introduced, followed by a presentation of typical applications of this technique. An overview of influencing factors on the individual point quality is given at the end of this chapter.

2.1 Laser Scanner: What is it?

A terrestrial laser scanner (TLS) provides a 3D point cloud of the surroundings by determining the position of visible surfaces using the reflection of laser light. Several types of laser scanners are in use and each have strengths and weaknesses depending on the application. The three main scanners in use are the triangulation-based scanners, the time-of-flight scanners and the phase-based scanners [161].

Detailed modeling and precise surface measurements are achieved using the so-called triangulation method, implemented in for example hand-held laser scanners or triangulation 3D scanners using single or double CCD cameras. Triangulation based scanners provide very accurate measurements, in the order of tens of micrometers. This method is however only applicable to small surface areas (in the order of centimeters size objects to few meters) and at close ranges (in the order of one to few meters). As this method is restricted in terms of object size and range to the object, and because the usual measurement set-up is far more complex for this method than for the two following methods presented in this thesis, the triangulation method is further not discussed. More references can however be found, on calibration of scanners that implement this principle [135, 163] and on applications on cultural heritage documentation [37, 16].

Time-of-flight of a laser pulse is a broadly used method, both in airborne and terrestrial laser scanning. Time-of-flight scanners emit a narrow laser beam pulse in a known direction and measure the backscattered signal reflected by the object surface. As depicted in Fig. 2.1, by determining the round-trip time of the emitted pulse, it is possible to determine the distance to an object in a known direction. This technique allows to scan objects over a larger range of distances, from few meters to kilometers. The maximum measurement rate depends on the user defined maximum distance. Indeed, the pulse travel time increases with increasing distance to the object. The scanner must wait for the return of the pulse, or for a time-out before sending out another pulse. Higher scanning distances involve higher waiting times, and therefore lower measurement rate. For longer distances, the acquisition time of the time-of-flight technique is relatively high. The 3D point accuracy achieved with this method is dependent on the accuracy of the round-trip time determination [74, 75], and is reported for example by Faro [44], Riegl [126] and Leica [85] to often be in the order of some millimeters.

In the past ten years, another type of scanner has been increasingly used: the phase-shift laser scanners. The principles of measurements are very similar to the time-of-flight scanners. Phase-based scanners emit a continuous amplitude modulated wave, often modulated with a combination of several different wavelengths. Among others, the shortest wavelength determines the precision that can be achieved and the longest wavelength defines the ambiguity of the measurements. As depicted in Fig. 2.1, the

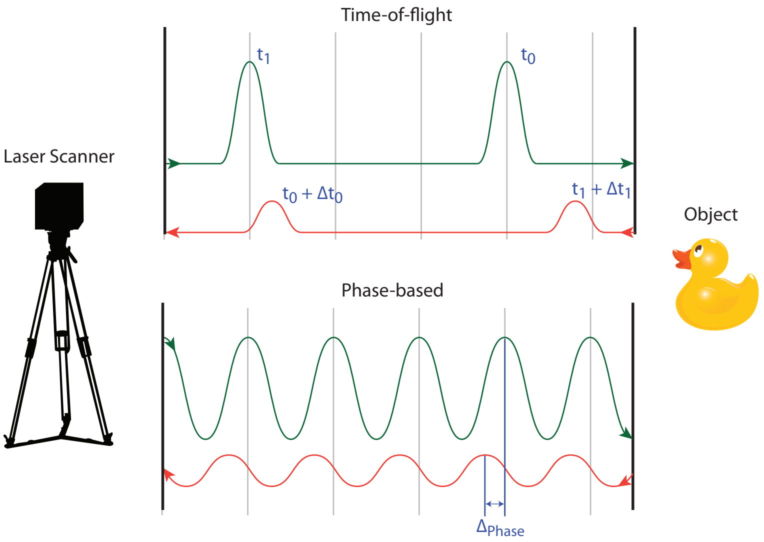

Figure 2.1: *Distance measurement principle of time-of-flight laser scanners (top) and phase based laser scanners (bottom).*

distance to an object is determined by measuring the phase shift between the emitted signal and the received signal. Because the phase-based laser scanners emit a continuous wave, it enables greater measurement rates [85, 44]. Moreover, phase-based scanners achieve slightly better measurement precision, mostly due to the multiple wavelength amplitude modulation and more accurate phase shift determination.

2.1.1 Laser beam and footprint

The common feature of all laser scanners is the laser light and the determination of a distance from the reflection of the light on an object surface. In general, the laser beam is assumed to have an ideal Gaussian intensity distribution, which means that the energy is normally distributed across the beam [68, 3]. This assumption approximates the laser light propagation to an ideal plane light wave propagation, which corresponds to a fundamental Transverse Electromagnetic Mode TEM_{00}. Due to diffraction, the laser beam tends to diverge as it propagates away from the emitter. The propagated beam first expands from a minimum beam width w_0, commonly known as the beam waist, see Fig. 2.2(a). For longer propagation distance (*i.e.* $z \to \infty$), the laser beam asymptotically approaches a cone of beam divergence γ_0 as defined in Eq. (2.1).

$$\gamma_0 = \frac{\lambda}{\pi w_0} \tag{2.1}$$

where λ denotes the wavelength of the laser light.

The radius $w(z)$ of the laser beam after the emission is given as a function of the distance propagated z, the wavelength of the laser light λ and the beam waist w_0, as shown in

Eq. (2.2).

$$w(z) = w_0\sqrt{1+\left(\frac{\lambda z}{\pi w_0^2}\right)^2} \tag{2.2}$$

The beam divergence of the Gaussian beam becomes relatively high for larger distances, and cannot be neglected. A larger beam radius results in larger footprint on the surfaces to be measured. Laser scanners aim at a smaller footprint, which enables a better measurement of the object surface. As an example, consider a laser source of typical beam waist size of $w_0 = 0.34$ mm and wavelength $\lambda = 785$ nm. The resulting beam divergence is equal to $\gamma_0 = 0.83$ mrad. At a distance of $z = 50$ m, the radius of the laser beam becomes $w(50) = 41.6$ mm. The convenience of the assumption of a Gaussian intensity profile is that the beam's intensity profile remains Gaussian after refraction of optical devices. For this particular application, the emitted laser beam is first expanded, then collimated by means of lenses and other optical elements, resulting in a coherent, directional and low-divergent laser beam, as depicted in Fig. 2.2(a). The beam divergence γ and the beam diameter after collimation d_0 are often calibrated and provided by the manufacturer of the laser scanner.

The footprint is defined as the intersection area between a surface and the laser beam. The shape of the footprint varies with two factors: i) the topography or shape of the surface, *e.g.* planar, spherical, ii) the scanning geometry, *i.e.* the angle at which the laser beam hits the surface. The local geometry depends on the distance and the orientation of the scanned surface, relative to the position of the scanner. The beam diameter $d(z)$, after collimation, is given as in Eq. (2.3). It also defines the diameter of the footprint of a laser beam hitting perpendicularly on a flat surface.

$$d(z) = d_0 + 2z\tan(\gamma) \tag{2.3}$$

Using the same laser source as described in the previous example, a collimated laser beam with a given beam divergence of $\gamma = 0.16$ mrad and a beam diameter at the exit of the collimator of $d_0 = 3$ mm results in a beam radius size of $d(50)/2 = 9.5$ mm at a distance of $z = 50$ m.

When beams are emitted on surfaces that are slanted with respect to the laser source and when assuming that the surface is planar relative to the size of the footprint, the resulting footprint is elongated, as depicted in Fig. 2.2(b), and is defined as an ellipse often described by its major axis $d_M(z)$ and minor axis $d_m(z)$, as given in Eq. (2.4) [140].

$$\begin{cases} d_M(z) = d_0 + 2z\dfrac{\sin(2\gamma)}{\cos(2\alpha)+\cos(2\gamma)} \\ d_m(z) = d_0 + 2z\dfrac{\sin(2\gamma)}{\cos(\alpha)\left(1+\cos(2\gamma)\right)} \end{cases} \tag{2.4}$$

where z is the distance of the planar surface to the origin, α is the incidence angle of the laser beam with respect to the surface and γ is the beam divergence after collimation. The footprint elongation $d_M(z)$ increases for larger ranges at higher incidence angles, as seen in Fig. 2.3.

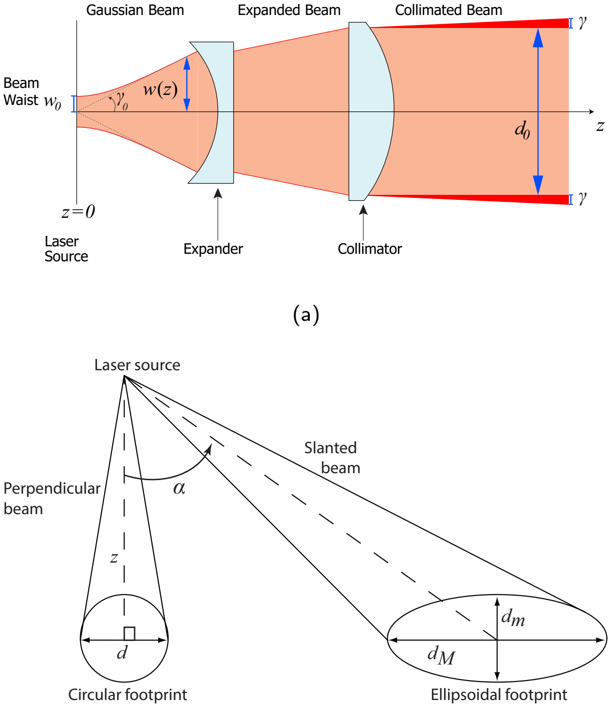

(a)

(b)

Figure 2.2: *Gaussian beam propagation and footprint shape.* ***(a)*** *Gaussian beam propagation expanded and collimated resulting in a coherent, directional and low-divergent laser beam. The beam waist w_0 is represented at the propagation distance $z = 0$ m. $w(z)$ represents the expansion of the emitted Gaussian beam, with beam divergence γ_0. d_0 defines the laser beam diameter at the exit of the collimator. For longer propagation distance (i.e. $z \rightarrow \infty$), the laser beam after collimation asymptotically approaches a cone of angular radius γ.* ***(b)*** *A laser beam hitting perpendicularly a surface placed at a distance z from the source results in a circular footprint of diameter d. A beam hitting a surface at an incidence angle α yields in an ellipsoidal footprint, defined by its major axis d_M and minor axis d_m.*

2.1.2 Emission of laser beams and detection

A laser scanner is an opto-mechanical measurement system, meaning that the laser beam after collimation is deflected on a set of mirrors towards a defined direction. The laser light being the carrier signal, in most of the current TLS systems, the emitted laser signal and the received echo of that signal are considered to determine the range to an object's surface. The point cloud acquisition process depends on the TLS in use. Different deflection mechanisms are currently in use, which produce different point cloud patterns and involve different detection systems.

Some mechanisms can scan bidirectionally (front and back), by using for example a rotating mirror, as shown in Fig. 2.4. In the case of a rotating mirror, the emitted beam

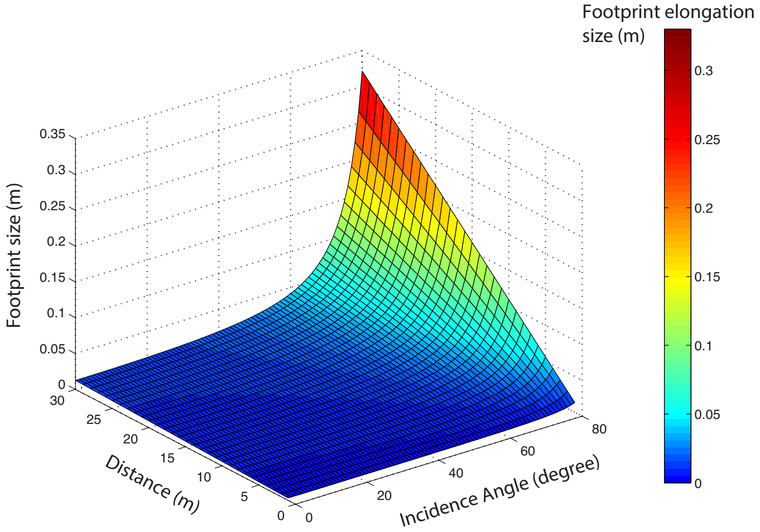

Figure 2.3: *Footprint size increases with increasing range and increasing incidence angle.*

is deflected 90° on the rotating mirror. The rotating mirror is inclined 45° and rotates by means of a motor which partially defines the resolution of the point cloud [88]. A slower mirror rotation combined with a high laser beam emission rate results in a large number of points per unit area. In the same way, a faster rotation of the mirror results in less points measured per unit area.

The mirror rotates at a defined speed, which defines the vertical angular step Δ_φ between each laser beam emitted. A full rotation of the mirror results in a plane of beams regularly spaced with Δ_φ over 360°, perpendicular to the emitted beam after collimation. These type of line scanners are used to measure profiles of objects, or can be integrated in a mobile mapping system.

By adding a motor to the scanning head that rotates in the horizontal plane at a defined speed, a horizontal angular step Δ_θ is added, which provides the third dimension to the point acquisition. By rotating in both horizontal and vertical directions, the laser scanner can acquire a spherical 3D point cloud of the surroundings, ideally with $360° \times 360°$ of field of view. In practice, the field of view of such a scanner is limited by the obstruction due to the fixation of the laser head on a tripod, usually of a cone of around 20°. In most laser scanning systems, the orientations of both the mirror and the scanner head are registered using angle encoders, which measurement accuracy can be up to 1 arcsecond. Other deflection systems can be used, *e.g.* multi-facets mirrors, prisms, oscillating mirrors, glass fibers. As extensive literature is already available on each specific system [168, 115], such as ALS systems [12, 165] and TLS systems [52], they will not be presented in this thesis.

The laser beam after deflection travels towards a defined direction through the atmosphere and bounces on objects surfaces that are present in the beam direction. In addition to coordinates, for each point in the point cloud an intensity value is provided. Depending on the object surface reflectance properties, a fraction of the emitted signal will scatter

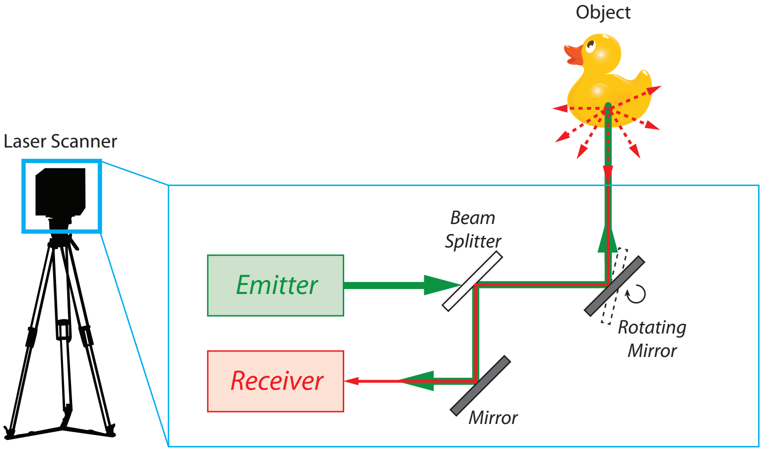

Figure 2.4: *Scanning mechanism: deflection of emitted laser light and received signal on sets of mirrors. The emitted beam is split using a beam splitter. A part is directed towards a direction, and the other part is used as reference. The difference between the reference and the echo signals define the distance to the surface.*

back to the laser scanner. This intensity value represents the amount of light received back at the scanner relative to amount of emitted light. The intensity value is often an uncalibrated product. According to the manufacturers of laser scanners, the original intensity values are rescaled such that the final values correspond to the perceptual sensitivity of a human eye. In this way, an intensity 'image' of a scan is produced that resembles a well-balanced black and white photo of the scanned scene. The intensity measurement has been well studied in many different fields of work [2, 116, 117, 114]. Many studies focus on correcting the intensity value [65] to make use of it in further calibration or post processing [69, 70, 71].

The strength of the signal received back at the scanner depends on the scattering behavior of the surface. Six main types of reflectivity are distinguished, as illustrated in Fig. 2.5. Specular reflection occurs on a mirror-like smooth surface: light from a single incoming direction is reflected into a single outgoing direction. In contrast to the specular reflection, Lambertian reflectance appears when the surface scatters the light diffusely in all directions [124]. In practice, the scattering behavior of a surface is often described by mixed models as the Minnaert model or the Henyey-Greenstein model that both result from combining the Lambertian with the specular model depending on the surface properties. Real surfaces are often more complex than these models. The anisotropy of the scattering as well as the surface roughness must be taken into account for each specific type of surface. An empirical model can be derived for a particular surface by analyzing it under all possible incidence angles.

The spreading of light that is reflected by a surface is described by the Bidirectional Reflectance Distribution Function (BRDF) that gives the ratio between the incoming and outgoing radiance [124]. As depicted in Fig. 2.6, a laser beam of radiation of flux density F (power crossing the unit area normal to the propagation direction) hits the surface at an incidence angle i and an azimuthal angle α_i. The irradiance or the total incident emitted power per unit area E at the surface is given by $E = F \cdot cos(i)$. The radiance or the

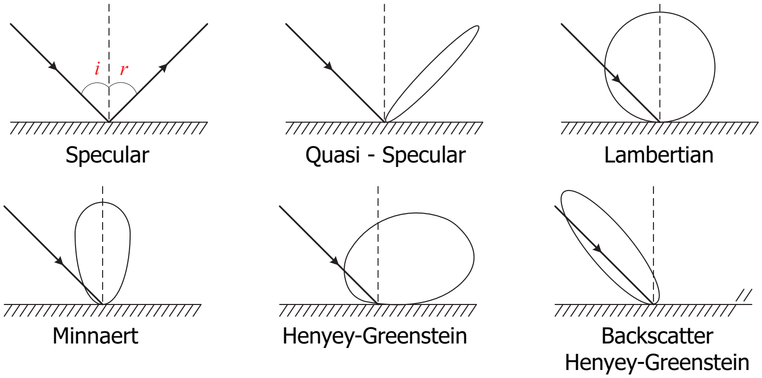

Figure 2.5: *Different surface scattering models.[124]*

total incident reflected power per unit area of the scattered radiation in direction (r, α_r) is denoted as L. The BRDF describes the physical reflection properties of the surface and it is defined as the ratio of the directional reflected radiance to the directional incident irradiance in Eq. (2.5):

$$BRDF(i, \alpha_i, r, \alpha_r, \lambda) = \frac{L(i, \alpha_i, r, \alpha_r, \lambda)}{E(i, \alpha_i, \lambda)} \tag{2.5}$$

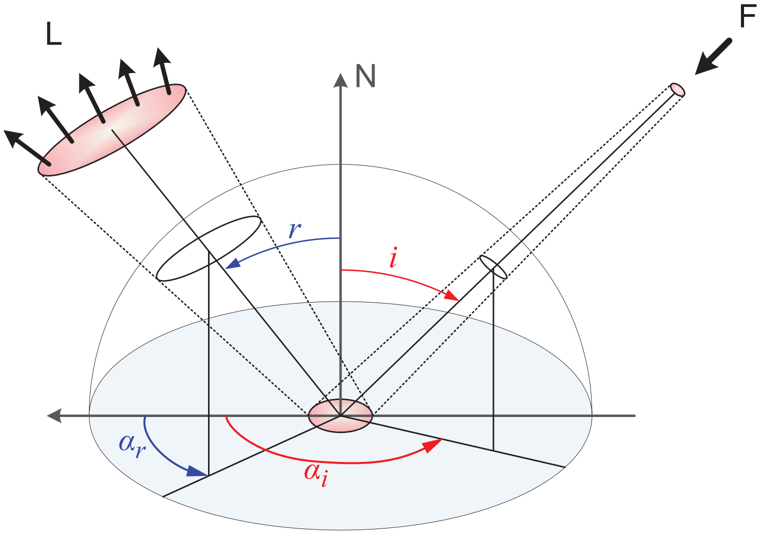

Figure 2.6: *Reflection geometry of a laser beam on a surface for the definition of the* $BRDF$.

A photodetector in the receiver unit detects the backscattered signal, which is then amplified and further analyzed to determine the distance.

2.1.3 Range determination

A laser scanner is a Light Detection And Ranging (LiDAR) system. The laser light is transmitted, either modulated as a pulsed wave or as a continuous wave with a predefined set of wavelengths. The laser beam after collimation is often split in two beams by means of a beam splitter as seen in Fig. 2.4. One beam is sent towards the sets of mirrors, the other beam is sent to the receiver unit. By comparing the original emitted signal and the received echo, the distance to a surface can be determined. As mentioned before, two main technologies are used: the time-of-flight laser scanners and the phase based laser scanners. The time difference Δt definition depends on the technology in use. As this time difference represents a back and forth travel, the actual time difference used to compute the distance to an object is $\Delta t/2$. For both technologies, the distance is determined using Eq. (2.6).

$$\rho = c\frac{\Delta t}{2} \tag{2.6}$$

where c is the speed of light.

Time-of-flight A pulse of few nano second is emitted regularly in time, often assumed to be Gaussian in shape and perpendicular to the propagation direction, as shown in Fig. 2.1. A fraction of this emitted beam is analyzed, where the time of the emitted pulse is defined as t_e. The measured echo, after amplification, is sent to a constant fraction discriminator, which determines the maximum of the pulse. The received pulse time is then defined as t_r. The difference in time between the emitted pulse and the received pulse is computed as Eq. (2.7):

$$\Delta t = t_r - t_e \tag{2.7}$$

The distance to an object ρ_{pulse} is computed from Eq. (2.6) and is given as Eq. (2.8) for time-of-flight laser scanners.

$$\rho_{pulse} = c\frac{t_r - t_e}{2} \tag{2.8}$$

This type of system needs to wait for the return signal before sending a new pulse to another direction. Therefore, the longer the distance to measure, the longer the measurement time. For measuring a maximum distance of 300 m, the back and forth signal travel time is $\Delta t = 2 \times 10^{-6}$ sec. Therefore the maximum measuring rate would be 500000 points/sec if the emission/receiving devices were ideal. In practice, this rate is not easily achievable since some time buffers are needed for the devices to rotate or analyze the signals. For a smaller maximum distance of 120 m, the back and forth signal travel time is $\Delta t = 0.8 \times 10^{-6}$ sec and the measurement rate increases to 1250000 points/sec. The accuracy of the range depends mainly on the detection unit, *i.e.* the photodector, and the time determination, *i.e.* the constant fraction discriminator. A clear study on the time-of-flight laser range determination topic is provided by [59] and [125].

Phase based A phase based laser scanner emits a continuous wave, which enables much higher measurement rates as the device does not need to wait for the return signal before sending the next one. Moreover, the modulation of such a continuous wave enables to achieve a accuracy in the order of millimeters, which is often better than the time-of-flight scanners. The laser light being the carrier signal is modulated, often using sinusoidal signals with several wavelengths amplitude modulation. The received signal is an echo of the emitted signal with a time delay, in the same principle as for the time-of-flight scanners. Assuming that the emitted signal consists of a simple modulation, *i.e.* a sinusoidal signal using one wavelength, the time difference Δt is related to the phase difference $\Delta\varphi$ between the emitted and the received signal, and the signal period λ/c, as defined in Eq. (2.9).

$$\Delta t = \frac{\Delta\varphi}{2\pi}\frac{\lambda}{c} \tag{2.9}$$

The distance R_{phase} is obtained from Eq. (2.8) and is defined for the phase based laser scanners as Eq. (2.10):

$$R_{phase} = \frac{\Delta\varphi}{4\pi}\lambda \tag{2.10}$$

As the signal is sinusoidal, the measurement of the phase difference can be ambiguous, meaning that there can be an uncertainty in the number of periods measured. To avoid this ambiguity, multiple wavelengths are used for the amplitude modulation. The longest wavelength defines the longest distance that can be measured, as a longer distance can be considered longer or shorter than what it actually is since the number of periods of the signal is not known. The shortest wavelength defines the range resolution, *i.e.* the ability to differentiate two objects on the same line of sight. Modulations with more wavelengths enable to enhance the signal to noise ratio of the received signal, so that the distance can be better determined. However, the more wavelengths are used, the more time is consumed to demodulate the signal and retrieve the range. In most current laser scanners, three wavelengths are used. The current systems can scan up to $\lambda_{long}/2 = 150$ m, with a short wavelength of $\lambda_{short}/2 = 1.2$ m.

As opposed to the time-of-flight systems, a phase based scanner has theoretically no limitations to the number of points it can acquire. However, in practice the number of points acquired is limited by the signal processing times in detection and demodulation.

The acquisition process of phase based scanners can be compared to the one in Global Navigation Satellite System (GNSS), where a carrier signal is modulated with multiple frequencies to resolve the unknown integer ambiguities, known as integer bootstrapping [153].

2.1.4 Relation between Cartesian and spherical coordinate systems

The scanner mechanism can be considered to operate in a spherical coordinate system [122], with a regular horizontal angle increment (Δ_θ) and vertical angle increment (Δ_φ) [95]. The TLS detects the returned signals of reflections on a surface and records the horizontal angle θ, the vertical angle and computes the range ρ to the object surface, regarding the TLS as the center of the coordinate system. In spherical coordinates, the point cloud is defined at regular intervals of θ and φ. In most current systems, a point cloud of n acquisitions is expressed in Cartesian coordinates, which are computed from the measured spherical coordinates as described in Eq.2.11.

$$\begin{bmatrix} x_i \\ y_i \\ z_i \end{bmatrix}_{i=1\cdots n} = \begin{bmatrix} \rho_i \cos\varphi_i \cos\theta_i \\ \rho_i \cos\varphi_i \sin\theta_i \\ \rho_i \sin\varphi_i \end{bmatrix}_{i=1\cdots n} \tag{2.11}$$

The 3D point cloud in Cartesian coordinates representation is unorganized. Reversely, the spherical coordinates of the point cloud are obtained from the Cartesian coordinates as described in Eq.2.12.

$$\begin{bmatrix} \theta_i \\ \varphi_i \\ \rho_i \end{bmatrix}_{i=1\cdots n} = \begin{bmatrix} \tan^{-1}\left(\frac{y_i}{x_i}\right) \\ \tan^{-1}\left(\frac{z_i}{\sqrt{x_i^2+y_i^2}}\right) \\ \sqrt{x_i^2+y_i^2+z_i^2} \end{bmatrix}_{i=1\cdots n} \tag{2.12}$$

Current laser scanners capture point position information. The points color (RGB) information is captured by an external camera, and is then mapped during post processing to the points. The point cloud can be viewed in different ways depending on the application. If the 3D positions are expressed in spherical coordinates as in Eq. (2.12), the point cloud can be viewed as a 2D image, where the horizontal angles θ_i are mapped on the horizontal axis and the vertical angles φ_i are mapped on the vertical axis. Each pixel of this 2D image can be colored with a defined feature. For instance, an intensity image (θ_i,φ_i,I_i) represents the light intensity I_i received per point (θ_i,φ_i). Another type of image is the range image $(\theta_i,\varphi_i,\rho_i)$ where each pixel value corresponds to the range ρ_i of a measurement. A range image is a 2.5D representation of the dataset, meaning that the 2D image is represented with a depth information.

2.2 Laser Scanning: A technology for surveying and 3D modeling

A laser scanner provides point clouds consisting of millions of points measured on the surface of objects. By capturing several point clouds around the object of interest, 3D models can be made, which can be further used, such as for visualization or further computations. The process of "stitching" multiple scans together is called registration and is presented below. An important step in the processing of the point clouds is to detect and identify objects within the points. This process is often called classification or segmentation and is also presented in this section.

2.2.1 A typical TLS surveying procedure

Surveying is the well-known technique that determines the position of objects accurately and depicts them in known forms, *e.g.* 3D Cartesian coordinates. The aim is to capture the reality as well as possible and represent it virtually. For many years, few different techniques were in use, *e.g.* total stations, leveling, photogrammetry. The surveying procedures of these techniques are very well documented [4, 143] and are still the predominant techniques in use. However, these methods are often consisting of single point measurements or 2D images. The post-processing of data such as 2D images enables to obtain a 3D point clouds. These techniques often do not provide massive 3D data at the capture. Since a decade, the terrestrial laser scanning technique has been more and more used to create data with a greater level of detail, more accurate and in 3D with shorter acquisition times. A survey using terrestrial laser scanners produce massive amounts of data in a very short time, therefore a proper surveying methodology needs to be defined.

To avoid collecting too many data, or missing important measurements, a thorough surveying procedure needs to be defined. At first, the requirements of the project needs to be well defined. What is the area of interest? What are the objects to be scanned? What is the scale of the total measurement area? What is the required measurement rate (*e.g.* hourly, daily, yearly)? At this first stage of investigation, it can be decided whether a TLS is suitable for the project. For example, a project that involves scanning water or glass windows is not suited for TLS technology, because the laser wavelengths in use yields a weak reflection back to the scanner. In those types of projects, the windows would have to be coated with a more reflective material, or the water would need some clay addition to opacify. For specific types of surfaces, photogrammetry would be a technique that is better suited. Another example is a project where data has been acquired continuously on a very small area. The laser scanner needs time to scan the same spot again, as the head of the scanner and the mirror rotate at regular increments. For point measurements, it would be better to make use of a total station.

A second step of the survey plan is to define the level of detail needed, the accuracy and precision of the measurements (see Sec. 3). What is the minimum feature size of the object of interest? What is the minimum point spacing needed? How accurate should be the point measurements? During this phase of planning, the resolution of the point cloud is defined. For instance, the maximum distances to be measured can be roughly estimated so a corresponding laser scanner can be selected. Table 2.1 provides a list of popular laser scanners used in 2014.

Manufacturer	Model	Type	Max. Range	Single point accuracy	Max. Scan rate (pts/sec)
FARO	Focus 3D	Phase	0.6m - 120m	±2mm	976000
Leica	P-20	Pulse/WFD [1]	0.1m - 120m	±3mm	1000000
Leica	HDS-7000	Phase	0.3m - 187m	±1.2mm	1016727
Leica	C-10	Pulse	0.1m - 300m	±6mm	50000
Topcon	GLS-1500	Pulse	1m - 330m	±4mm	30000
Riegl	VZ-6000	Pulse	5m - 6000m	±15mm	37000

Table 2.1: *Laser scanners specifications*

Unless the project consists in scanning a very simple object with one scan, usually a scanning survey consists in acquiring multiple scans over the area to obtain a full coverage. To register the scans together, the measurement set-up has be planned beforehand, for instance by estimating the maximum range a scanner can scan and making sure that two

---

[1] WFD refers to Waveform Digitizing technique used to determine the range. These types of scanners are still time-of-flight laser scanners, enhanced with a waveform digitizing technique. This type of scanner is supposed to be faster than a normal time-of-flight scanner, and should provide point clouds with low noise.

acquisitions would have enough overlap. The stand-points of the scanner in the scenery have to be planned, as well as targets placement in the scenery. Depending on the scanner in use, certain types of targets are more suited than others. For instance, a black and white checkerboard target is better suited for phase based scanners. Targets with different reflectivity materials are better for time-of-flight scanners.

Usually when surveying, several techniques of measurement can be combined to achieve a better dataset of the area of interest. Some of the above mentioned scanners have an integrated color camera, usually a few mega-pixel resolution camera. Pictures of the scenery are taken and later on registered with the point cloud, so both the point cloud and the pictures are expressed in the same coordinate frame (see Sec. 2.2.2). The closest pixel to a point provides the color information of the 3D point. This process is usually performed as post-processing, as it takes too much time to be performed while scanning. Another technique used in parallel to scanning is to measure points in the scenery with GPS to reference the whole dataset on a map. Usually, the positions of targets or stable features of the area are measured using Real Time Kinematic GPS. These measurements are then integrated in post-processing so all measurements are expressed in an unified coordinate frame.

Once the scans are registered and referenced, either using an arbitrary coordinate frame or geo-referenced, the data can be analyzed and further processed according to the project's needs, *e.g.* surface modeling [120, 159] or classification [64, 42, 164, 33]. Registered scans are often used to perform deformation monitoring of man-made structures such as buildings [53, 51, 167, 136], or tunnels [98, 57] and to monitor natural areas [129, 99]. The quality of the point cloud acquisitions shows to be a crucial aspect when considering the monitoring and deformation analysis [67, 111, 6].

2.2.2 Registration

The process of registration consists in overlaying scans of a same scenery, either captured from different stand points, and/or from different times. The scans are overlaid in such way that they represent the scene in the same coordinate frame to obtain a global point cloud of the scanned area. One of the scans is regarded as the reference scan. The coordinate frame of this reference scan will be the reference coordinated frame where all the other scans will be geometrically aligned to. As a terrestrial laser scanner produces $1:1$ scale measurements, the scans do not need to be rescaled before the overlaying.

A rigid-body transformation preserves the shape of the scans. It only rotates and/or translate the whole scan to overlay on the reference scan. The registration process consists of executing a method that determines the rotation angles $[\varphi,\theta,\psi]$ and the translation parameters $\mathbf{T} = [T_x, T_y, T_z]^T$ that result in the best alignment of two scans. Typically, two scans are considered to be aligned in the best possible way if a suitable objective function is minimized in the least squares sense, *e.g.* minimizing the distance between matching tie points, or between matching surfaces. Redundancy of information enables a better estimation of the rotation and translation parameters, therefore enough tie points overlapping on two consequent scans should be planned.

A translation consists of moving the coordinates of an object in the same defined direction. In Cartesian coordinates, for instance, the translation of a point $\mathbf{P}_i = [x_i, y_i, z_i]^T$ with a translation direction $\mathbf{T} = [T_x, T_y, T_z]^T$ is defined as:

$$\begin{aligned}\mathbf{P}_{i\text{–translated}} &= \mathbf{P}_i + \mathbf{T} \\ &= \begin{bmatrix} x_i \\ y_i \\ z_i \end{bmatrix} + \begin{bmatrix} T_x \\ T_y \\ T_z \end{bmatrix}\end{aligned} \tag{2.13}$$

A rotation rotates the object about the $x-$, $y-$, and $z-$ axis. The three basic rotation matrices about the $x-$, $y-$ and $z-$ are defined in counterclockwise direction when looking towards the origin as follows:

$$\begin{aligned}\mathbf{R}_x(\varphi) &= \begin{bmatrix} 1 & 0 & 0 \\ 0 & \cos\varphi & -\sin\varphi \\ 0 & \sin\varphi & \cos\varphi \end{bmatrix} \\ \mathbf{R}_y(\theta) &= \begin{bmatrix} \cos\theta & 0 & \sin\theta \\ 0 & 1 & 0 \\ -\sin\theta & 0 & \cos\theta \end{bmatrix} \\ \mathbf{R}_z(\psi) &= \begin{bmatrix} \cos\psi & -\sin\psi & 0 \\ \sin\psi & \cos\psi & 0 \\ 0 & 0 & 1 \end{bmatrix}.\end{aligned} \tag{2.14}$$

Let A, B and C be matrices respectively of dimensions $(i \times l)$, $(l \times k)$ and $(k \times j)$. The multiplication of A, B and C is associative, *i.e.* $[ABC]_{ij} = A_{il}B_{lk}C_{kj} = ([AB]_{ik})C_{kj} = A_{il}([BC]_{lj})$. When multiplying two matrices, their dimensions must satisfy the product $(i \times j) = (i \times k)(k \times j)$. If the matrices are not squared, this product is not satisfied when commuting. If the matrices are diagonal and of the same dimension, then the multiplication is commutative. A matrix multiplication is associative but not commutative. As such, many different rotation matrices can be derived depending on the order of the desired rotations. A rotation matrix obtained from the multiplication of the three rotation matrices Eq. (2.14) is given as:

$$\begin{aligned}\mathbf{R}(\varphi, \theta, \psi) &= \mathbf{R}_z(\psi)\mathbf{R}_y(\theta)\mathbf{R}_x(\varphi) \\ &= \begin{bmatrix} r11 & r12 & r13 \\ r21 & r22 & r23 \\ r31 & r32 & r33 \end{bmatrix} \\ &= \begin{bmatrix} \cos\theta\cos\psi & -\cos\varphi\sin\psi + \sin\varphi\sin\theta\cos\psi & \sin\varphi\sin\psi + \cos\varphi\sin\theta\cos\psi \\ \cos\theta\sin\psi & \cos\varphi\cos\psi + \sin\varphi\sin\theta\sin\psi & -\sin\varphi\cos\psi + \cos\varphi\sin\theta\sin\psi \\ -\sin\theta & \sin\varphi\cos\theta & \cos\varphi\cos\theta \end{bmatrix}\end{aligned} \tag{2.15}$$

The rotation of a point $\mathbf{P}_i = [x_i, y_i, z_i]^T$ with rotation angles $[\varphi, \theta, \psi]$ is defined as:

$$\begin{aligned}\mathbf{P}_{i\text{–rotated}} &= \mathbf{R}\mathbf{P}_i \\ &= \begin{bmatrix} r11 & r12 & r13 \\ r21 & r22 & r23 \\ r31 & r32 & r33 \end{bmatrix} \begin{bmatrix} x_i \\ y_i \\ z_i \end{bmatrix}\end{aligned} \tag{2.16}$$

Many different rigid body transformations can be defined depending on the order of the desired rotations and translations [39]. The 3D rigid body transformation is defined as the 4×4 matrix with 6 degrees of freedom, which first rotates the points then translate them as follows:

$$\begin{bmatrix} x_i \\ y_i \\ z_i \\ 1 \end{bmatrix}_{\text{transformed}} = \mathbf{RP}_i + \mathbf{T} = \begin{bmatrix} r11 & r12 & r13 & T_x \\ r21 & r22 & r23 & T_y \\ r31 & r32 & r33 & T_z \\ 0 & 0 & 0 & 1 \end{bmatrix} \begin{bmatrix} x_i \\ y_i \\ z_i \\ 1 \end{bmatrix}_{\text{original}} \tag{2.17}$$

Two main registration methods are distinguished [17, 169]. The first class of methods consists in matching tie points, or reference points [107, 118, 43]. Before scanning a scenery, reference objects are placed in the line of sight of the scanner, and later on used to match and overlay the scans. The second class of methods reconstruct features in the scenery based on measured points such as planes or lines [15, 60, 110, 58]. These features are used for matching between two scans.

The point clouds can also be georeferenced, which means that they are expressed in a chosen external geodetic coordinate system, *e.g.* WGS84. Direct georeferencing implies that the position and orientation of the scanner head are known [93]. A total station or a GPS receiver can be used to measure the exact position of the stand point. Indirect georeferencing makes use of local control points measured in the scene with another method, such as again a GPS receiver or total station. These points, either recognizable features or targets, are then mapped in the point clouds, and the whole point cloud is transformed accordingly.

2.2.3 Segmentation

After acquiring millions of 3D points, one direct post-processing step is to group the points to fit a specific analysis. Segmentation algorithms group points that have similar properties under a given homogeneity criterion, *e.g.* planar features, color features. Many segmentations methods are currently implemented [109], each of them specifically designed to group points in a predefined environment and type of data, *e.g.* forest data or building site data. Most of these methods can eventually be customized to comply to another type of data.

A segmentation divides the data in several regions that are all connected. The regions are viewed either as a group of points with similar homogeneity criterion, or as a group of points surrounded by edges. Two main categories of segmentation are commonly used to extract surface features: region growing and edge connection. Region growing method detects continuous surfaces under a local surface criterion, such as planar, convex or concave surfaces, or a defined color gradient. The region grows around a chosen seed point as long as the local surface criterion is fulfilled [55, 56, 128, 121]. Other approaches to region growing are the so called split-and-merge methods [9]. At first, the data is split in equal regions by means of quadtrees or octrees, until the points in each subregion are meeting the predefined homogeneity criterion. Once the split phase is finished, neighboring regions with similar properties are merged. The merge phase is repeated until no more region need a change. Edge-based methods detect discontinuous surfaces under a predefined criterion [36, 142]. Edges of discontinuous surface are connected to produce object contours.Fig. 2.7 depicts the edge detection and a segmentation of a duck in 7 homogeneous colors areas.

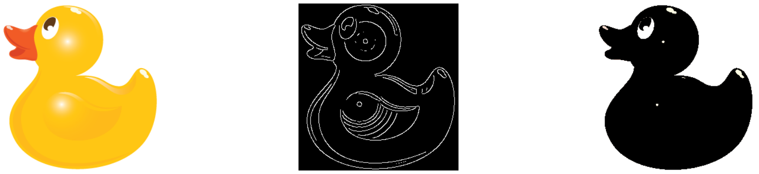

Object Edges Background

Segment 1 Segment 2 Segment 3

Segment 4 Segment 5 Segment 6

Figure 2.7: *Edge detection and segmentation of a 2D duck picture. The edges of the duck are detected by looking for local maxima of the gradient of a grayscale image. The duck is partitioned in 7 different clusters of colors by using a k-means clustering method.*

Both categories of segmentation require well defined threshold values. These methods are often sensitive to noise in the point cloud and varying point density. The data is most of the time filtered from noise and biases before being segmented. The quality description of individual 3D point quality will improve the quality of the segmentation and result in more accurate regions of similar properties.

2.3 Factors influencing the individual point quality

The systematic and random errors induced by the scanning mechanism as well as the surrounding factors accumulate in the final point cloud products. Errors of individual points propagate through standard processing steps like registration or segmentation into final products such as 3D as-built models or structural monitoring results. The quality of individual points is influenced by several factors. Considering the point cloud acquisition process as a link budget [119], four main groups of influencing factors can be distinguished: i- instrumental, ii- environmental, iii- object related, iv- scanning geometry. In this section, the influencing factors that play a role on the quality of a 3D point acquisition are presented, but for which, in many cases, the user has limited influence on, namely the instrumental factor, the environmental factor, the object related factor.

2.3.1 Instrument and hardware limitation

Like any instrument, a terrestrial laser scanner is not perfect. The systematic and random errors due to the mechanical design and the technical limitations of the hardware propagate in both the emission of the laser beam and the reception of the reflected light. A thorough calibration of the instrument often enables to identify the systematic errors and correct the biases in the final point cloud [24, 133]. Different calibration approaches are studied, *e.g.* calibration based on point matching [150, 47, 134], planar features matching [11, 1] or cylinder features matching [22, 23]. Laser scanner self-calibration determine different calibration parameters based on the point-cloud measurements, by for instance focusing on the correction of systematic errors [91, 92]. Different methods of analysis are used to determine the calibration parameters, such as the covariance analysis [10], piecewise linear functions [102] or Fourier transform techniques [132].

Random errors due to the inherent physical properties of the different units are often not easily removable.

At the emission of the laser beam, three main factors are to be taken into account. The first factor is the beam divergence deviation σ_{beam}, which represents the uncertainty in the angular position of the emitted laser beam [3, 141]. The beam divergence γ_0 is the derivative of the beam radius, as defined in Eq. (2.2), with respect to the axial position. The emitted laser beam can have a small deviation from the center axis of the desired direction. This uncertainty is however often negligible for scanners with good collimation.

The second factor is in relation with the beam deflection unit, which depends on the type of laser scanner in use. Some scanners use a single-facet rotating mirror [85, 44], others use a multi-facet rotating mirror [126]. Each system has its own error sources, *e.g.* variation of facet angles, surface roughness [124], mirror deformation [168]. Moreover, the angular position of the mirror is recorded by a shaft encoder [5], which translates the angular position of the mirror into a digital code. By taking all possible instrumental error sources, the beam deflection angular precision $\sigma_{\text{angular deflection}}$ is a common factor to both types of deflection unit. The uncertainty of this angular position propagates in the final point cloud, as this position determines the vertical angle position φ_i of a point.

The third factor is the axes error σ_{axes}, which comprises three different axes. The first axis is the horizontal axis, which is the rotation axis of the mirror. The second axis is the vertical axis, which is the rotation axis of the head of the scanner. The last axis considered is the collimation axis, which is the axis that passes through the center of the mirror, both for the emission of the beam and the reception of the echo. These axes are never perfectly aligned and stable, and therefore result in uncertainties [92].

At the reception of the echo signal, the above mentioned instrumental uncertainties play a role when detecting the echo signal. On the top of those factors, few more random errors are added. First, depending on the type of scanner in use, namely a phase-based or a time-of-flight, the determination of the range differs, see Sec. 2.1.3. For a time-of-flight scanner, the effect of non-linearities and noise in the received pulse rising edge can affect the pulse arrival time determination, defined as $\sigma_{\text{pulse time}}$. For a phase based scanner, the determination of the phase difference between the received and the emitted signals can be altered by uncertainties $\sigma_{\text{phase diff}}$ due to *e.g.* the signal digitization, initial and final phase computation, or phase shift computation. Finally, for both types of scanners, a last major uncertainty to be taken into account is the range determination precision $\sigma_{\text{range instrument}}$. As explained in Sec. 2.1.3, the range is not directly measured, it is derived from the measurement of time or phase difference between the emitted and received laser beam. The precision of the range computation depends on the precision of the measured reflected signals.

2.3.2 Atmospheric conditions

After the emission, the laser beam travels through the air until it reaches an opaque surface [141]. The object's surface scatters the light in many directions, as explained in Sec. 2.1.2. The measured backscattered light also travels back through the air. The laser beam will be affected by atmospheric conditions depending on the wavelength in use. The main atmospheric factors to take into account are the ambient temperature, the humidity, the ambient light, the vibrations due to turbulences and the pureness of the air. The laser beam can be affected in three ways. First, it can be attenuated, meaning that the signal intensity becomes weaker as it travels through the medium. Second, the signal can be distorted, which means that a pulse would be elongated of shortened and that a continuous wave frequency is changed. Third, the laser beam can be deviated from its original propagation direction due to atmospheric disturbances such as droplets or dust particles present in the medium [13, 18, 63].

Extreme atmospheric conditions such as very high or low temperatures, rain and wind can affect the instrument functioning. For instance, some mechanical rotations like the mirror or the scanning head may not be as accurate as specified when scanning under normal weather conditions. Moreover, the mirror surface is affected by changes of temperature and can deform. Water condenses on the surface resulting in a thin layer of water or droplets. Additionally, like every electronic instrument, the functioning of the scanner is affected by humid conditions and can damage the inner electronic part by oxidation and weakening the connections.

As described by Weichel [166], the atmospheric attenuation is a combination of the molecular absorption and scattering, and the aerosol absorption and scattering. Two main atmospheric attenuation factors due to particles in the air are to be taken into account [124, Sec. 3.4.2]. The first attenuation factor is the scattering of the light due to particles in the air. These particles are either in the size of molecules, which is the Rayleigh scattering, or the particles are larger but in the order of the wavelength λ, which is explained by the Lorenz-Mie theory. Diffraction theory describes the scattering of very large particles such as water droplets. The second attenuation factor is due to the absorption of the light by gases and by particles present in the air, *e.g.* water vapor, dust.

During the two ways travel, the laser beam interacts with the atmosphere [124, Chap. 4], mainly consisting of nitrogen (78%) and oxygen (21%). Water is also present, often as water vapor. Among other gases, the atmosphere also contains carbon dioxide (0.035%). All the gaseous constituents of the Earth atmosphere have an influence on the transmission of signals depending on the signal wavelength, as shown in Fig. 2.8. The attenuation of the laser beam in the atmosphere is described by the Beer-Lambert's law [166], which relates the absorption of light to the properties of the material through which the light signal is traveling:

$$\eta_{atm} = \frac{I(\rho)}{I_0} = e^{-\Gamma\rho} \tag{2.18}$$

where η_{atm} is the atmospheric transmittance, I_0 is the intensity of the emitted signal, $I(\rho)$ is the intensity of the received signal, ρ is the distance to the object and Γ is the atmosphere attenuation factor or optical depth.

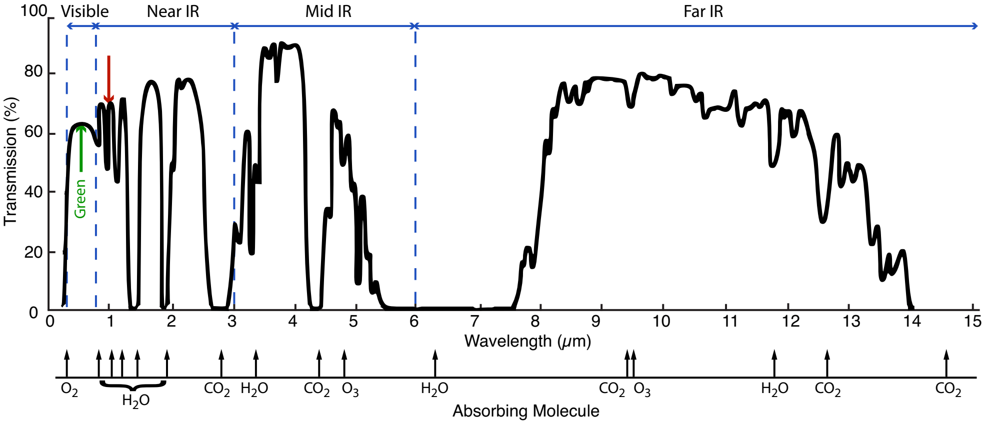

Figure 2.8: *Wavelength dependence on the atmospheric transmittance measured over* 1820 *m path at sea level. [166]*

Moreover, as seen in the Fig. 2.8, the atmospheric attenuation is dependent on the laser light wavelength in use and the range to the object. The manufacturer often provides general measurement accuracies under near-laboratory conditions. When the user is capturing a point cloud, it is often never under those conditions. Indoors, the artificial ambient light and the dust in the air have to be taken into account. Outdoors, possible rain and fog affect the number of returned points, as the laser beam has difficulties to penetrate through water droplets without being distorted and scattered around. Moreover, the sunlight also disturbs the laser beam as the same wavelength as the beam is relevant in the solar emission spectrum.

2.3.3 Object scattering properties

As explained in Sec. 2.1.2, the BRDF characterizes the variations of the reflectance properties of a surface with the illumination and the scattered light directions as the Eq. (2.5). The surface properties can be described using for instance the albedo, the roughness or the directional-hemispherical reflectance. The anisotropy of the reflected light defined by the BRDF depicts the dependency of the reflected intensity with respect to the incidence direction. The reflectivity property of a material defines the amount of light scattered, with respect to the wavelength of the laser light in use. The laser scanner has therefore a view on the surroundings in terms of intensities, it can be seen as a black and white picture, where the brighter the pixel, the more reflective the material.

In general, the albedo is defined as the ratio between the total power scattered by the material and the total incident power. The albedo is dependent on the direction of the incident signal. The absorption and reflection of the received light are inherent properties of the material and dependent on the wavelength of the emitted signal. The color of a surface is a human perception property, which represents the visible spectrum of wavelengths that are not absorbed by the material and reflected back. However, as the laser scanners function under different wavelengths, namely IR and green spectrum, the color property does not impact the perception of a laser scanner in the same way as for the human eye.

The irradiance M defined as Eq. (2.19) represents the total power reflected by the material L_{out} in all possible directions and depends on the material reflectivity properties [124, 103].

$$M = \int_{\theta=0}^{\pi/2} \int_{\varphi=0}^{2\pi} L_{\text{out}} \cos\theta d\varphi \tag{2.19}$$

The surface roughness scatters the light in different directions and affects the reflectance properties of a surface. If a surface is perfectly smooth, it acts like a mirror and reflects the light specularly in one direction, following the law of reflection as depicted in Fig. 2.5. As a TLS measures in backscatter, in the particular case of specular reflections no light signal is returned back to the scanner if the surface is not perpendicular to the emitted beam. A TLS can therefore not measure mirror-like surfaces if they are not exactly placed perpendicularly to the emitted laser beam. If the surface is ideally rough, the light is scattered homogeneously in all directions, following the Lambertian scattering model depicted in Fig. 2.5. The outgoing radiance is then independent of the direction of the incoming light as it is isotropic, following:

$$M = L_{\text{out}} \int_{\theta=0}^{\pi/2} \int_{\varphi=0}^{2\pi} \cos\theta d\varphi \tag{2.20}$$

Most of the surfaces encountered while scanning are not perfect. They have different albedos, different backscatter models and roughnesses. Defining each material scanned during a surveying plan is a very tedious work and costs a lot of time with respect to the actual influence on the point cloud quality. The two major influences the material property has on the individual point quality are: i- the number of returned signals, ii- the signal distortion. It is often not possible to scan surfaces that have a high transmittance or that are highly specular, such as windows, transparent surfaces or mirror-like unless these surface are on beforehand coated with a more reflective and rough material. Other types of materials can distort the backscattered signal, such as high reflectance materials or polarized materials. The estimated range is then biased due to the distortion of the received signal, as the estimation of the range depends on the estimated time or phase of the backscattered signal, see Sec. 2.1.3.

The influence of the material properties on measured intensity and the number of returned points have been sparsely studied. However, a thorough study of this influencing factor has to be performed, where all the consequent uncertainties σ_{material} on the range measurement still has to be defined. Currently some studies have shown the effects of surface properties on the quality of individual points [21, 94], mainly focusing on the returned intensity measurements for instrument calibration [69, 71], analysis and use of the intensity meansurement [2, 117] or the correction of the intensity measurement [65]. As this study would be on itself equivalent to another PhD study, it is not part of this work.

2.3.4 Scanning geometry

Scanning geometry is defined as the incidence angle and the range to a surface. The incidence angle is defined as the angle between the laser beam vector and the normal vector of the surface. The range is defined as the distance between the TLS and the surface. This influencing factor is the only factor where the user have control on.

This influencing factor is well studied on Airborne Laser Scanning data [137]. The effects of this factor on TLS measurements are briefly identified in some studies [115, 76], by for instance investigating the intensity return under different scanning geometry conditions [116, 69, 78]. These effects are modeled in our contributions [148, 147, 149].

This influencing factor is further studied in detail in Chapter 4, where models of incidence angle and range effects are presented. The developed scanning geometry models are currently being widely used [77, 40, 34] and applied in many different studies such as deformation modeling in man-made structures [127, 96] as well as natural sites [80, 48, 100] using scanning geometry constraints.

2.4 Conclusions

In this chapter, the following research question was investigated and answered: What major factors influence the quality of an individual point in a point cloud?

This chapter presented an overview of the principles of laser scanning. By using the laser light as a carrying signal, the distance to objects is estimated from the backscattered signal reflected on objects surfaces. As a 3D position of surfaces is captured with a very short time and with very good accuracy, it has been shown that the technology of laser scanning is more and more used in surveying procedures. After the acquisition, the point clouds are post processed for further applications. As the errors of individual points propagate in the final product, there is a need for a good point quality description. The manufacturer provides basic technical specifications which are often obtained in near-laboratory conditions. In practice, the quality of individual points in a point cloud is influenced by four main factors. Three of the four main factors were presented in this chapter, namely the instrument limitations, the atmospheric conditions and the object properties. In real-life, the end-user often has a limited influence on these three factors. It is difficult to modify parameters such as mirror rotation, foggy weather or wall material to comply with better scanning conditions. The last influencing factor is the scanning geometry, for which the end-user has a strong influence as the position of the laser scanner in the scenery is determined by the user. The influence of the scanning geometry will be further discussed in Chapter 4.

All the presented factors influence the measurement of individual points, by either adding noise or by distorting the intensity and shape of the emitted signal. The range determination precision depends on the quality of the received signal. The precision of individual point comprises all the possible uncertainties due to instrumental errors, environmental conditions, object surface properties and scanning geometry as follows:

$$\sigma_{\text{point}} = \sqrt{\sigma^2_{\text{instrument}} + \eta^2_{atm} + \sigma^2_{\text{material}} + \sigma^2_{\text{geometry}}} \tag{2.21}$$

It is assumed that every error factor is uncorrelated. The propagation of the individual errors in the point precision and eventually to the point cloud is presented in Chapter 3.

Part II

Identification and modeling scanning geometry influence on the quality of a point cloud

Chapter 3

Quality assessment using planar features

> “Quality means doing it right when no one is looking.”
>
> Henry Ford

High spatial resolution and fast capturing possibilities make 3D terrestrial laser scanners widely used in engineering applications and cultural heritage recording. Most surveying applications require high quality end products, which can only be achieved by carefully processing high quality acquisitions. Although the TLS measurements are in general reliable, they are subject to random and systematic errors. A thorough quality description of the individual point is currently needed to improve the end-products that make use of 3D point clouds [67, 28, 32, 35, 112, 25, 20, 101, 7, 82, 48].

In this chapter, the following research question is investigated and answered:

How can the quality of an individual point in a point cloud be assessed?

First, in Sec. 3.1 the basics of quality description are presented, consisting of the accuracy and the precision of a measurement. As the background in probability and statistics is not the same for every reader, elements used in this work are detailed in this chapter. The quality analysis of the point cloud is further described using error propagation techniques. The quality of a point cloud presented in this thesis is based on the estimation of local planar features. There are several methods to fit a plane to a number of points. In this thesis, three methods were investigated that are commonly used in the field of laser scanning [104], which enabled us to process massive amounts of data with reasonable processing time and memory usage. These methods are compared and evaluated in Sec. 3.2. Based on the results it is decided which method is further used in the rest of this work. The quality of each local fit is described using a Least Square Estimation. The main quality describers used in this work are presented for each method.

3.1 Accuracy and Precision

Statistical analysis of the data spatial dispersion enables to characterize the uncertainty of the measurements [152, 154]. Generally, the uncertainty of measurements is defined as the systematic and random errors. Random errors are described by the statistical dispersion of the measurements, from which the precision of the acquisition is derived. Random errors are by definition not reproducible and are determined using the redundancy of information. Systematic errors, conversely, are reproducible errors and are defined by the biases of the measurements, from which the accuracy of the acquisition is derived. A reference value or true value is needed to determine the systematic errors. Fig. 3.1(a) depicts an example of systematic and random errors on targets and Fig. 3.1(b) depicts the uncertainty determination using normally distributed data.

The variability of the random errors distribution is an indicator for the quality of the measurements. A good quality acquisition is obtained when the systematic and random errors are minimal around the required levels.

The accuracy refers to the deviation of measurements from a true value, as depicted in Fig. 3.1. A reference or true value can be acquired with a different more reliable measurement technique such as a total station point measurement, or could refer to a horizontal and a vertical datum such as a WGS 84 coordinate point. The identification of biases is one of the main steps to achieve a good calibration of the instrument [92, 71, 132]. The position of every single point is difficult to be verified using other surveying techniques. In this thesis, the systematic errors or biases are not further analyzed. The instrument is considered to be well calibrated and ready to be used "as is".

The precision of a measurement is defined by two main factors. The first factor is the repeatability of a measurement. It defines the variations of the measurements when using one same instrument repeatedly for the same target under constant surveying conditions in a short period of time. Small variations in these repeated measurements define a good repeatability and a consistency in the measurements. The second factor is the reproducibility of a measurement. It defines the variations of the measurements when using the same instrument under different surveying conditions and long periods of time between the measurements. Both the repeatability and the reproducibility are expressed as standard deviations, as depicted in Fig. 3.1(b). The definition of the precision of a measurement does not require a true value, and therefore it can be estimated using the measurements only. A reliable measurement is a measurement that is precise, *i.e.* repeatable and reproducible. Many studies have been conducted in the field of the calibration of the instrument [11, 90, 89, 92, 97, 139, 134, 132, 162, 71, 70, 29, 24]. However, there is very limited literature that deals with the propagation of errors on individual points in a 3D point cloud. This chapter presents different ways to propagate errors that were used in this thesis.

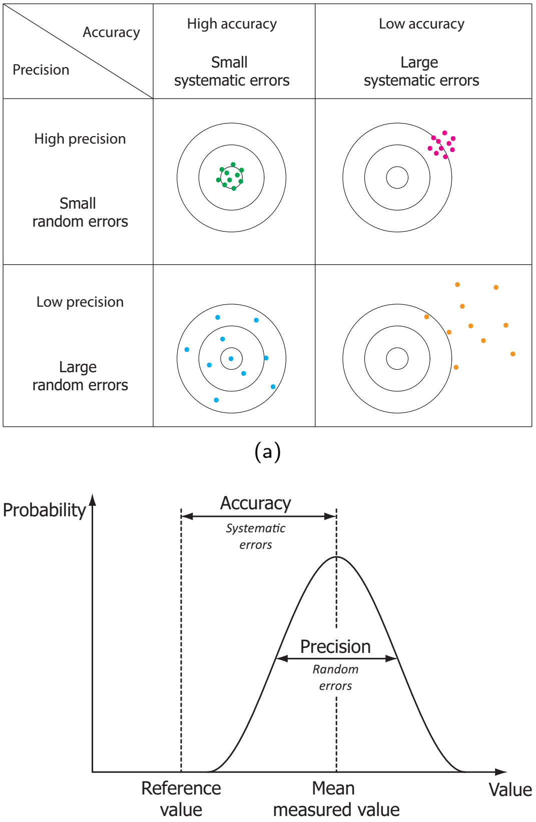

(a)

(b)

Figure 3.1: *Random errors and systematic errors.* ***(a)*** *Random and systematic errors using a target as a reference value. The precision and the accuracy of the measurements are dependent respectively on the random errors and systematic errors.* ***(b)*** *Uncertainty determination using normally distributed data.*

3.2 Planar feature extraction and noise level

TLS technology measures signal reflections on object surfaces as point clouds. Assuming the surface is locally sufficiently planar as further described in Chapter 3, a plane can be estimated on the object surface. In this thesis, the considered dataset is a small area of the point cloud obtained after subdivision of planar segments data extracted from a point cloud as described in Sec. 2.2.3 or a small neighborhood. A larger dataset requires more memory and is therefore computationally heavier. The local area can be an entire planar segment (see Sec. 2.2.3), a smaller area like a patch (*e.g.* a 10×10 cm area as shown in Chapter 5) or a local neighborhood (*e.g.* 10 points in the surrounding of the point of interest). The resulting planar parameters can be applied for different purposes, *e.g.* normal extraction, 3D modeling, segmentation, classification, feature extraction, registration. In this work, we are using the planar parameters to assess the individual point quality in a point cloud.

The following methods are based on the equation of a plane defined as Eq. (3.1).

$$f\left(x, y, z\right) = \mathbf{PN} + d = 0 \tag{3.1}$$

where $\mathbf{P} = \left[x, y, z\right]$ denotes a point on the plane, $\mathbf{N} = [n_1, n_2, n_3]^T$ is a normal vector of the local plane and d denotes the distance to the plane from the origin.

The derivation of the local planar features differs with respect to to the stochastic components taken into account. The following section introduces several plane fitting methods: Least Squares (LS) plane estimations and Principal Component Analysis (PCA). The LS methods presented in this work are formulated following a common notation, see [154]. The uncertainty investigated in this work deals only with the noise levels, biases are not studied.

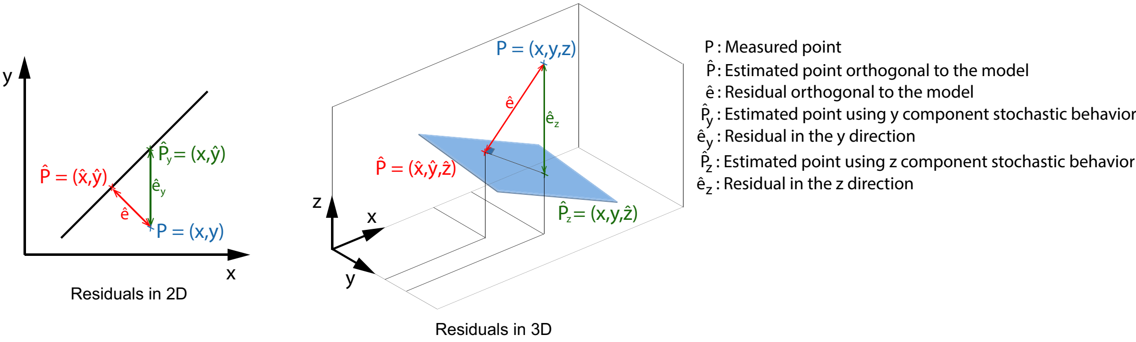

Figure 3.2: *2D and 3D Residuals of Least Squares Estimation methods. In both cases, the residuals can be defined in one specific direction or perpendicular to the fitted model.*

3.2.1 Complexity of algorithms

An algorithm is a list of calculation steps. It inputs data, processes it through the defined calculation steps and outputs a result. Every single calculation step requires a specific processing time, which is a function of the input data size.

For example, let us consider the simple case of the addition and the multiplication of two numbers a and b. In both cases, the algorithm is the most 'complex' when a and b are consisting of the same number of digits n. As an example, the algorithm of the addition process is given in Algorithm 1. This algorithm describes the steps to follow when two numbers have to be added together, by means of 'for loops'. The function 'Mod' computes the remainder of the division and the function 'Floor' rounds the number out.

In the same way, the algorithm for the multiplication of two numbers a and b is given in Algorithm 2.

Multiplying two n-digits numbers requires more processing time than simply adding them up. As seen in the pseudo-code in Algorithm 2, a multiplication requires the machine to first multiply digit by digit and add them up accordingly afterwards. The multiplication

Algorithm 1: Addition (base 10) of two numbers

```
input  : a[$1,\cdots,n$], b[$1,\cdots,n$]
output : result

for $i \leftarrow 0$ to $n-1$ do
    result[$i$] ← Mod((a[$i$]+b[$i$]+c,10));
    c ←Floor((a[$i$]+b[$i$]+c)/10);
end
result[$n$] ← c;
```

Algorithm 2: Multiplication (base 10) of two numbers

```
input  : a[$1,\cdots,n$], b[$1,\cdots,n$]
output : result

for $i \leftarrow 0$ to $n-1$ do
    c ←0;
    for $i$=0 to $n-1$ do
        product ← (a[$i$]*b[$j$]+c);
        temp[$j$][$i+j$] ← Mod(product,10);
        c←Floor(product /10);
    end
    temp[$j$][$n+j$] ←c
end
for $i$← 0 to $2*n-1$ do
    sum ← c;
    for $j \leftarrow 0$ to $n-1$ do
        sum ← sum + temp[$j$][$i$];
    end
    result[$i$] ← Mod(sum,10);
    c ← Floor(sum /10);
end
result[$2*n$] ← c;
```

algorithm is more complex than the addition algorithm as it involves a ‘for loop’ in a ‘for loop’.

In terms of number of operation realized, the addition algorithm would perform n number of operation, realized in the 'for loop'. As the multiplication algorithm contains a nested ‘for loop’, it would perform n^2 operations.

The asymptotic running time is a generally accepted describer for quantifying the efficiency of an algorithm [30, 8]. The asymptotic running time describes the number of operations an algorithm would perform as a function of the size of the data to be processed.

The symbol big O is commonly used for estimating the order of magnitude of a variable and describing the asymptotic upper bound of an algorithm, which expresses the worst case scenario of computation. It means that an algorithm could need the indicated maximum number of operations, but it could also need less, depending on the specific input data. An algorithm provides a solution to a given problem, however the way it solves the problem may be more or less efficient from an asymptotic running time point of view. An algorithm is called optimal if there is no alternative algorithm solving the same problem with a better asymptotic running time. If, for example, the asymptotic running time of an optimal algorithm to solve a certain problem is $O(n \log n)$, we say this problem has a computation complexity of $O(n \log n)$.

As big O characterizes functions according to their growth rates as n approaches infinity, only the components in the algorithm with the highest growth rate are taken into account, leaving out the constants, scaling factors and lower order terms. Therefore, the big O is a describer that provides a fairly good estimate how an algorithm scales for large values of n. However, when considering smaller n the asymptotic running time is less relevant. By looking at the previously shown examples, the main factor to be taken into account is the number of 'for loops'. The asymptotic running time of the addition algorithm is $O(n)$, which is linear, and the one for the multiplication algorithm is $O(n^2)$, which is squared.

3.2.2 Ordinary Least Squares based on normal equations

The Ordinary Least Squares (OLS) method estimates the plane coefficients by minimizing discrepancies in one given Cartesian direction. In this section, a weighted least square approach is presented that uses the statistical behavior of the observations in the estimation model, and provides an unbiased estimator [154]. Using this method of least squares estimation implies the assumption that the variances of the other two Cartesian components are not taken into account. In this section, the example of the least squares estimation in the z-direction is presented, assuming the x and y components to be deterministic.

From this assumption, the equation of a plane Eq. (3.1) is formulated as:

$$z_i = -\frac{(n_1 x_i + n_2 y_i + d)}{n_3} \tag{3.2}$$

Let A be a [m×n] design matrix and $\mathbf{x}$ be the planar parameters of the considered area. The general LS system is expressed as:

$$\mathbf{y} = \mathbf{A}\mathbf{x} \tag{3.3}$$

where $\mathbf{y}$ is the vector of observations.

Using this LS formulation in the case of the OLS estimation in the z-direction, the vector of observations is expressed as follows:

$$\mathbf{y} = [z_i]_{i=1,\ldots,n}$$

and the design matrix $\mathbf{A}$ is:

$$\mathbf{A} = [x_i, y_i, 1]_{i=1,\ldots,n}$$

In this case of OLS, the planar parameters $\mathbf{x}$ are defined as follows:

$$\mathbf{x} = \left[\frac{n_1}{n_3}, \frac{n_2}{n_3}, \frac{d}{n_3}\right]^T$$

In this thesis, the focus is put on finding the Best Linear Unbiased Estimation (BLUE), which is obtained by substituting the weight matrix with the inverse of the observational covariance matrix $\mathbf{W} = \mathbf{Q}_{\mathbf{yy}}^{-1}$ [154]. The LS estimation of the planar parameters $\hat{\mathbf{x}}$ is then given as Eq.2.59 in [154]:

$$\boxed{\hat{\mathbf{x}} = \left(\mathbf{A}^T \mathbf{Q}_{\mathbf{yy}}^{-\mathbf{1}} \mathbf{A}\right)^{-1} \mathbf{A}^T \mathbf{Q}_{\mathbf{yy}}^{-\mathbf{1}} \mathbf{y}} \tag{3.4}$$

where $\mathbf{Q_{yy}}$ denotes the dispersion or the second central moment of $\mathbf{y}$, which is represented as the covariance matrix $\mathbf{Q_{yy}} = D(\mathbf{y})$. D represents the mathematical dispersion operator. When assuming a Gaussian model for the parameter estimation, the complete structure of the PDF is given by $\mathbf{y} \sim \mathcal{N}(\mathbf{Ax}, \mathbf{Q_{yy}})$.

In this case, the estimated planar parameters are given as:

$$\hat{\mathbf{x}} = \begin{bmatrix} \hat{x}_1 & \hat{x}_2 & \hat{x}_3 \end{bmatrix} \tag{3.5}$$

The normalized plane norm is defined then as follows:

$$\mathbf{N} = \begin{bmatrix} \dfrac{-\hat{x}_1}{\sqrt{\hat{x}_1^2 + \hat{x}_2^2}} & \dfrac{-\hat{x}_2}{\sqrt{\hat{x}_1^2 + \hat{x}_2^2}} & 1 \end{bmatrix}^T \tag{3.6}$$

The distance between the plane and the origin is given as:

$$d = \frac{-\hat{x}_3}{\sqrt{\hat{x}_1^2 + \hat{x}_2^2}} \tag{3.7}$$

Following the Eq.2.12 in [154], the least squares residual vector $\hat{\mathbf{e}}$ is defined as follows:

$$\boxed{\hat{\mathbf{e}} = \mathbf{y} - \hat{\mathbf{y}}} \tag{3.8}$$

The residuals minimized in this method are only expressed in the z-direction, as follows:

$$\hat{\mathbf{e}} = [z_i - \hat{z}_i]_{i=1,\dots,n} \tag{3.9}$$

The planar parameters $\mathbf{x}$ are estimated to minimize the sum of squares of the deviations $\hat{e}_i$ as Eq.2.9 in [154]:

$$S = \underset{\mathbf{x}}{\arg\min} \sum_{i=1}^{n} \hat{e}_i^T \hat{e}_i \tag{3.10}$$

The sum of squares of OLS minimizes the residuals in the z-direction as defined in:

$$S = \arg \min_{n_1, n_2, d} \sum_{i=1}^{n} (z_i - \hat{z}_i)^T (z_i - \hat{z}_i) \tag{3.11}$$

The least squares estimation model described in this thesis minimize the l^2-norm of the residuals. One can also compute the perpendicular residuals to the fitted model, defined as the distances from the points to the plane, and they are computed as follows:

$$\hat{\mathbf{e}}_\perp = \begin{bmatrix} x_i & y_i & z_i & 1 \end{bmatrix} \begin{bmatrix} \mathbf{N} & d \end{bmatrix}^T \tag{3.12}$$

These orthogonal residuals are not used for this particular LS minimization. Their values have no influence in the OLS fitting process.

The variance-covariance matrices of the estimated parameters $\mathbf{Q}_{\hat{\mathbf{x}}\hat{\mathbf{x}}}$, the estimated values

$\mathbf{Q}_{\hat{\mathbf{y}}\hat{\mathbf{y}}}$ and the residuals $\mathbf{Q}_{\hat{\mathbf{e}}\hat{\mathbf{e}}}$ are given as follows:

$$\begin{aligned}
\mathbf{Q}_{\hat{\mathbf{x}}\hat{\mathbf{x}}} &= \left(\mathbf{A}^T \mathbf{Q}_{\mathbf{yy}}^{-1} \mathbf{A}\right)^{-1} \\
\mathbf{Q}_{\hat{\mathbf{y}}\hat{\mathbf{y}}} &= \mathbf{A} \mathbf{Q}_{\hat{\mathbf{x}}\hat{\mathbf{x}}} \mathbf{A}^T \\
\mathbf{Q}_{\hat{\mathbf{e}}\hat{\mathbf{e}}} &= \mathbf{Q}_{\mathbf{yy}} - \mathbf{Q}_{\hat{\mathbf{y}}\hat{\mathbf{y}}}
\end{aligned} \tag{3.13}$$

The number of points per area of interest varies with the type of considered subdivision (*e.g.* segment, Cartesian area selection, spherical area selection, neighboring points). To compare the quality of one area with respect to another, the Root Mean Squared Error (RMSE) is used, which takes into account the number of points per area. The RMSE is an indication of the precision of the residuals based on the fitted plane parameters and the sample observations, and is computed as described in Eq. (3.14). As we assume the data to be unbiased, the RMSE is equivalent to the standard deviation of the residuals $\sigma_{\hat{\mathbf{e}}}$.

$$\mathrm{RMSE} = \sigma_{\hat{\mathbf{e}}} = \sqrt{\frac{\hat{\mathbf{e}}^T \hat{\mathbf{e}}}{n-m}} \tag{3.14}$$

where n is the number of observations and m is the number of estimated parameters. The redundancy of information is expressed as $p = n - m$. In this case, the number of parameters to be estimated is $m = 3$.

The OLS is a simple deterministic process that enables to estimate planar parameters from observations by solving an inconsistent system of equations. By incorporating the statistical behavior of the observations by using the weighting matrix $\mathbf{W} = \mathbf{Q}_{\mathbf{yy}}{}^{-1}$, we are able to estimate planar parameters that are optimal and unbiased.

Incorporating the reference standard deviation $\sigma_{\hat{\mathbf{e}}}$ means that the local noise level is used to express confidence in how well the points determine the planar parameters. The matrix of observational variances $\mathbf{Q}_{\mathbf{yy}}$ is derived as shown in Eq.3.15.

$$\mathbf{Q}_{\mathbf{yy}} = \sigma_{\hat{\mathbf{e}}}^2 I_n \tag{3.15}$$

In determining the planar parameters, a higher point density will result in more precise planar parameters estimation. In general, using the redundancy of the observations $(p = n - m)$ allows the derivation of adjusted points on the adjusted planar surface with a precision far below the nominal point precision of an individual laser point.

The propagation of the planar parameters quality on the center of gravity (CoG) $M = [\bar{x}, \bar{y}, \bar{z}]$ of the area enables a good representation of the range quality of the considered area. Based on the linear variance propagation law described as Eq.3.16 [154], for each considered area, the quality of the planar fitting is propagated $\hat{\sigma}_m$ to the center of gravity M.

$$\hat{\sigma}_m^2 = A_m \mathbf{Q}_{\hat{\mathbf{x}}\hat{\mathbf{x}}} A_m^T \tag{3.16}$$

In this OLSE method, the matrix A_m is defined as $A_m = [\bar{x}, \bar{y}, \bar{z}]$. The planar quality describers obtained with this method are not based on approximations.

Advantages of this method This method enables the computation of planar features of a set of points very easily. Moreover, this linear LS estimation offers the possibility to analyze the quality of the planar features in an extensive and complete way.

Disadvantages of this method The residuals are minimized in one direction only. Therefore, if the plane is not tilted in a xy-plane, the residuals to be minimized will not make sense, e.g. a xz-plane to be estimated using the residuals in z-direction will not provide an optimal solution. This method is limited in terms of planar orientation, as the residuals to be minimized become larger for other orientations than xy-planes. One could first rotate the points about a given angle, however to do so, one has to first determine this angle, therefore the normal of the plane passing through these points needs to be known. This method is very sensitive to outliers. One way to deal with outliers is to make use of a weighted LS [154], *i.e.* a weight matrix per point, or to filter the outliers before applying this method, *e.g.* by using a RANSAC method [45] or any other outlier detection methods such as data-snooping methods (*e.g.* W-Test), Tau Test or t- Test [155]. The inversion of the $n \times n$ variance-covariance matrix in Eq. (3.4) requires a large memory capacity and can be seen as the major limiting factor of the complexity computation. The complexity of the OLSE method has an asymptotic bound $O(n^2 log(n))$ [128].

3.2.3 Least Squares Plane fitting based on Homogeneous Equations

This method is based on the solution proposed in [61], and is often called Total Least Squares Estimation. This method is originally presented by [49]. This method estimates the planar features by assuming all the coordinates' stochastic behavior. The minimized residual per point is the perpendicular distance to the fitted model. This type of residuals is independent of the coordinate system in use.

Let the equation of a plane be defined as Eq.3.1. Using matrix notation, this equation is written as follows:

$$\begin{gathered}\begin{bmatrix} x_i & y_i & z_i & 1 \end{bmatrix}_{i=1\dots n} \begin{bmatrix} n_1 & n_2 & n_3 & d \end{bmatrix}^T = \mathbf{0}_{n\times 1} \\ \mathbf{A}\mathbf{x} = b \end{gathered} \tag{3.17}$$

where $\mathbf{0}_{n\times 1}$ is a vector of $[n \times 1]$ zeros. Recall that we have n observations, and in this case $m = 4$ parameters to estimate. It is required that $n \geq m$ to ensure a unique solution exists for the following minimization problem. The LS solution $\hat{\mathbf{x}}$ minimizes the sum of the squares as in Eq. (3.10) defined as follows:

$$S = \arg\min_{x} \|\mathbf{A}\mathbf{x} - \mathbf{b}\|$$

One trivial solution to this problem is $\hat{\mathbf{x}} = 0$. A sufficient condition for the existence of a nontrivial solution is given in Theorem 4.1 by [49], formulated as follows:

> Let $\hat{\sigma}_j$ be the j^{th} largest singular value of $A \in \mathbb{R}^{m\times n}$ and σ_j be the j^{th} largest singular value of the augmented matrix $[b|A]$, with v_j the corresponding right singular vector, $m > n$. If
>
> $$\hat{\sigma}_n > \sigma_{n+1} \tag{3.18}$$
>
> then $\sigma_n > \sigma_{n+1}$ and the Total Least Square problem has an existing solution and is the only solution to the problem.

To minimize the sum of the squared errors, the gradient with respect to each planar parameter should be equal to zero. The solution of this problem is obtained by making use of the singular value decomposition (see Section 7.4 in [83]). The solution of this linear LS problem is given by the matrix of eigenvalues λ and the matrix of eigenvectors $\mathbf{x}$

of the $\mathbf{A}^T\mathbf{A}$ matrix. The solution $\hat{\mathbf{x}}$ that minimizes the Least Squared Error is given by the eigenvector of the $\mathbf{A}^T\mathbf{A}$ matrix corresponding to the smallest eigenvalue $\lambda_{min} = \min_i \lambda_i$. The eigenvectors $\mathbf{x}$ of the matrix $\mathbf{A}^T\mathbf{A}$ and the corresponding eigenvalues λ_i are computed using the singular value decomposition, *e.g.* built in in Matlab®.

In this case, the estimated planar parameters are given as:

$$\boxed{\hat{\mathbf{x}} = \begin{bmatrix} \hat{x}_1 & \hat{x}_2 & \hat{x}_3 & \hat{x}_4 \end{bmatrix}^T} \tag{3.19}$$

The normalized plane norm is then defined as follows:

$$\mathbf{N} = \left[\frac{\hat{x}_1}{\sqrt{\hat{x}_1^2 + \hat{x}_2^2 + \hat{x}_3^2}} \quad \frac{\hat{x}_2}{\sqrt{\hat{x}_1^2 + \hat{x}_2^2 + \hat{x}_3^2}} \quad \frac{\hat{x}_3}{\sqrt{\hat{x}_1^2 + \hat{x}_2^2 + \hat{x}_3^2}} \right] \tag{3.20}$$

The distance to the plane is given as:

$$d = \frac{\hat{x}_4}{\sqrt{\hat{x}_1^2 + \hat{x}_2^2 + \hat{x}_3^2}} \tag{3.21}$$

This method solves the Least Squares estimation based on homogeneous equations, which means that the vector of observations $\mathbf{y}$ is equal to zero. Therefore the residuals $\hat{\mathbf{e}}$ that are minimized are given as the perpendicular distance to the fitted model as follows:

$$\boxed{\hat{\mathbf{e}} = \mathbf{A}\hat{\mathbf{x}}} \tag{3.22}$$

In this method, the number of parameters estimated is $m = 4$. Therefore, a constraint has to be made on the computation of the RMSE which is based on the sample mean and not on the population mean. It is computed as follows:

$$\mathrm{RMSE} = \sqrt{\frac{\hat{\mathbf{e}}^T\hat{\mathbf{e}}}{n - m + 1}} \tag{3.23}$$

where n is the number of observations and m is the number of estimated parameters. The redundancy of information is expressed as $p = n - m$. Similarly to the previous method, we assume that all the observables have the same precision and that the weight matrix gives the same weight to all the observables.

Advantages of this method The Total Least Squares method minimizes the orthogonal distance to the model. As shown in Fig. 3.2, this vector of residuals is independent of the coordinate system direction, and therefore more reliable than the residuals resulting from the previously presented OLSE method.

Disadvantages of this method The computational complexity of this algorithm is very important. The asymptotic upper bound is dominated by the bound of the singular value decomposition, as $O(mn^2))$ [49]. This limits the amount of data that can be processed, as it requires a lot of internal memory. Moreover, as this method is non linear, the complete quality description can not be computed. Only approximations to linear models can be used to provide an approximation of the quality describers.

3.2.4 Principal Component Analysis

Consider a set of n observations $\mathbf{X} = [x_i, y_i, z_i]_{i=1,\dots,n}$ of coordinates of points on a planar surface. As described in Eq. (3.24), the aim of this method is to find the Cartesian basis $\mathbf{B}$ with respect to which the observations are expressed such that no correlations between different Cartesian directions is possible. The corresponding change of basis $\mathbf{B}$ transforms the n observations $\mathbf{X}$ into a dataset $\mathbf{Y}$. The basis $\mathbf{B}$ estimates a Cartesian coordinate system that is the best in a least squares sense: it minimizes the perpendicular distances from the data to the fitted plane model formed by two of the axes.

$$\mathbf{Y} = \mathbf{B}\mathbf{X} \tag{3.24}$$

Note that the size of the matrix of observations $\mathbf{X}$ is $n \times m$, where in this case the data dimension is $m = 3$.

The point cloud is first centered around its center of gravity $\mathbf{M} = E[\mathbf{X}] = \left[\bar{x}, \bar{y}, \bar{z}\right]$ so that the data set has a zero empirical mean.

$$\mathbf{X_c} = \mathbf{X} - \mathbf{M} \tag{3.25}$$

Then, the $m \times m$ covariance matrix[1] $\mathbf{C_x}$ of the mean-deviated data $\mathbf{X_c}$ is computed as defined in Eq.3.26.

$$\mathbf{C_x} = \frac{1}{n-1}\mathbf{X_c}\mathbf{X_c}^T \tag{3.26}$$

The components $c_{i,j}$ of $\mathbf{C_x}$ represent the covariance of the variable components $\mathbf{X_i}$ and $\mathbf{X_j}$. The variance of a component $c_{i,i}$ indicates the spread of the variable component $\mathbf{X_i}$ around its mean value.

The eigenvectors $\mathbf{V}$ of the covariance matrix $\mathbf{C_x}$ and the diagonal matrix $\mathbf{D}$ of the eigenvalues λ of the covariance matrix $\mathbf{C_x}$ are computed as in Eq.3.27 using *e.g.* the eigen decomposition in Matlab®.

$$\mathbf{V}^{-1}\mathbf{C_x}\mathbf{V} = \mathbf{D} \tag{3.27}$$

where $\lambda = diag(\mathbf{D})$. Note that the covariance matrix $\mathbf{C_x}$ is a symmetric positive definite matrix, and that its eigen decomposition results in positive eigenvalues only. An eigenvalue is a scaling factor, *i.e.* a stretch or a shrink. A negative eigenvalue characterizes a reflection, meaning that the scaling occurs in the opposite direction.[83]

An orthogonal basis is created by ordering the eigenvectors V in the order of descending eigenvalue size, *i.e.* the first column of this orthogonal basis consists of the eigenvector having the direction of the largest variance data. We assume the variance of the two first principal components to be larger than the variance of the measurement noise. That is, the two eigenvectors corresponding to the two largest eigenvalues represent the two 2D axes of the best fitted plane to the point cloud. The third eigenvector, which corresponds to the smallest eigenvalue, is orthogonal to the first two and defines the normal vector $\mathbf{N}$ of the fitted plane.

The $m \times n$ vector of residuals $\hat{\mathbf{e}}$ is obtained by computing the distances from the mean-deviated points X_c to the plane, as explained in Eq.3.28

$$\hat{\mathbf{e}} = \mathbf{X_c}\mathbf{N} \tag{3.28}$$

---

[1] Note that the covariance matrix is obtained based on the sample mean of the dataset. As the population mean is assumed to be unknown,the sample covariance matrix takes into account the redundancy of information. If the population mean is known, the population covariance matrix becomes: $\mathbf{C_x} = \frac{1}{n}\mathbf{X_c}\mathbf{X_c}^T$.

The distance to the plane is defined as:

$$d = [\bar{x} \quad \bar{y} \quad \bar{z}]\mathbf{N} \tag{3.29}$$

In this method, the number of parameters estimated is $m = 3$. It is computed as follows:

$$\mathrm{RMSE} = \sqrt{\frac{\hat{\mathbf{e}}^T\hat{\mathbf{e}}}{n-m}} \tag{3.30}$$

where n is the number of observations and m is the number of estimated parameters. The redundancy of information is expressed as $p = n - m$.

Advantages of this method Principal Component Analysis (PCA) is one of the key tools in multivariate statistical analysis. The linear regression determined by a PCA minimizes the perpendicular distances from the point cloud to the fitted model regardless the coordinate frame. PCA is in some sense comparable to the Total Least-Squares method (see the previous method), but it is known to be computationally more efficient. Moreover, PCA can incorporate a covariance matrix to take the relative quality of the observables into account. PCA determines the optimum basis, in terms of Least-Mean-Squares-Error, in which the data set can be re-expressed, using orthogonal linear transformations.

The complexity of the PCA has an asymptotic upper bound $O(nm^2)$, where $m = 3$ is the data dimension [38]. By comparing it to the previously presented methods, the best scenario for computation of the OLSE is worse than the worst scenario for the computation of the PCA, see the practical assessment presented further.

Robust PCA can be used instead of the classic PCA, where a non-trivial robust covariance matrix is incorporated that results in the determination of more robust Principal Components [157]. The main reason why this method is not used in this work is that the determination of this robust matrix is recursive and computationally heavy. The use of the classic PCA is chosen for its fastness and linear behavior. Moreover, the classic PCA can handle large amounts of data very accurately with very fast processing time, given that there are no outliers. Additionally, one can also investigate the Independant Component Analysis, which separates statistical independent components from each other and finds a basis that is not necessarily orthogonal.

Disadvantages of this method The quality analysis of the planar features is not achieved as straightforward as for the OLSE method.

PCA is very sensitive to outliers. If large outliers are present, the first component of the orthogonal basis is often attracted toward outlying points instead of the main direction of the observations [130]. To cope with this major drawback, prior to using PCA, an outliers filtering procedure should be applied on the dataset. Many different filtering algorithms are present, which are often computationally heavy as well [131]. In this work, the robust plane fitting is performed using the RANSAC algorithm, which is very fast and requires low amounts of memory. Considering that each random sample should contain at least three points, which is the minimum to define a plane, and assuming that at most 50% of the points are outliers, 35 random samples are needed to ensure, with a probability of 99%, that at least one sample is outliers-free [61]. The relatively small number of the required random samples compared to the large amounts of data indicates that the computational cost of this type of robust plane fitting is easily affordable. Finally, the

PCA method is not robust for exceptional cases such as points aligned as a line. The efficiency of the algorithm depends on the structure of the data.

3.3 Practical assessment

To illustrate the different planar fitting methods, in this section a short practical assessment is presented. First, the performances of the algorithms based on two simulated datasets are shown. Afterwards, the three above described planar fitting methods are demonstrated on two real datasets. The first dataset is extracted from a real life point cloud of a planar surface without outliers. The other dataset is containing some large outliers. The comparison of the methods on these cases provides practical information on the performance and the applicability of each method.

The proposed methods have been tested on a workstation Dell Precision 390, with 3 Gb of RAM memory, a Dual-Core Intel CPU at 2.13 GHz, and a graphical card NVIDIA Quadro FX3500 256-bit GDDR3. The computations are run under the OS Microsoft Windows 7. The programs are implemented using the software Matlab. The plots are also generated using Matlab.

3.3.1 Simulated data

The first simulated data is a point cloud of 100 000 points. This point cloud is generated such that it simulates the pattern of a real point cloud. The points are regularly distributed in the xy-plane and normally distributed in the z-direction, following the distribution $\mathcal{N} \sim (0, 0.003\ m)$. The three above described algorithms are used to fit a plane through this dataset. The performances of each algorithm is listed in Table 3.1.

Method	OLSE	Total LS	PCA
Number of Points	100 000		
Time (s)	0.28	1.03	0.16
RMSE (m)	0.0030	0.0030	0.0030

Table 3.1: *Performance of plane fitting algorithms on first simulated dataset*

As stated previously, the orientation of this point cloud is ideal for the OLSE method presented in Sec. 3.2.2. The resulting point quality is the same using all three algorithms and is also the same as the individual point cloud quality. They all deliver the same planar parameters. However, the OLSE and the PCA methods are computing the planar parameters much faster than the Total Least Square method. Therefore, it is concluded that if the orientation of the considered point cloud is known beforehand, the choice of the planar fitting method influences the processing time to extract the planar parameters.

The second simulated data is generated in the same way as the previous one, except that in this case the point cloud is oriented in the xz-plane. The points still follow a normal distribution $\mathcal{N} \sim (0, 0.003\ m)$ in the y-direction. The performance of each algorithm is listed in Table 3.2.

Method	OLSE	Total LS	PCA
Number of Points	100 000		
Time (s)	0.28	1.03	0.16
RMSE (m)	1.45	0.0030	0.0030

Table 3.2: *Performance of plane fitting algorithms on the second simulated dataset*

In this case, the "worst case scenario" for the OLSE method is presented, where the points are oriented vertically while the residuals in the z-direction are minimized. It is seen that by using the OLSE method on such a case, the estimated planar parameters are not fitting the points. However, the other two methods perform well in this case too, showing that the orientation of the plane is not influencing the end results.

Note that for the two presented experiments, the computational effort of the planar fitting methods is the same for the same number of points. It is however seen that the orientation of the plane plays an important role in the decision of which method to use. If the orientation of the plane is on forehand known, the OLSE method is an attractive method, as it computes the planar parameters very fast and provides a full quality description of the resulting parameters. If the latter is not needed, the PCA method is then the preferred method for its fastness. The Total Least Squares method costs the most computational efforts but provides the best planar parameters regardless the orientation of the plane, and enables a quality description.

3.3.2 Real data

In this paragraph, sets of points are extracted from real datasets. The point clouds are captured using the TLS Faro LS880, which is reported by the manufacturer to provide a global individual point quality of 3 mm.

The first real dataset is extracted from a point of cloud of an indoor area. It contains 13851 points. This point cloud is extracted from a horizontal floor area. Again, the three above described algorithms are used to fit a plane through this dataset. The performance of each algorithm is listed in Table 3.3.

Method	OLSE	Total LS	PCA
Number of Points	13 851		
Time (s)	0.02	0.82	0.03
RMSE (m)	0.0035	0.0035	0.0035

Table 3.3: *Performance of plane fitting algorithms on first real dataset*

A visualization of this point cloud is given in Fig. 3.3, where a smaller random sample of the used points is plotted for better visibility. The respective distributions of the residuals per methods are plotted in Fig. 3.4.

The three methods deliver the same quality in terms of the resulting RMSE. Again, as seen previously, the Total Least Squares method is much slower than the OLSE or the PCA. In this case, the obtained results are comparable to the simulated horizontal dataset.

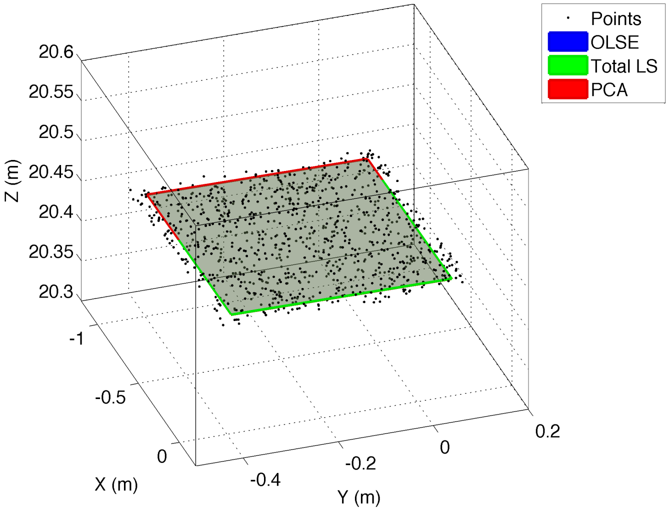

Figure 3.3: *3D Plot of real dataset of a floor without outliers*

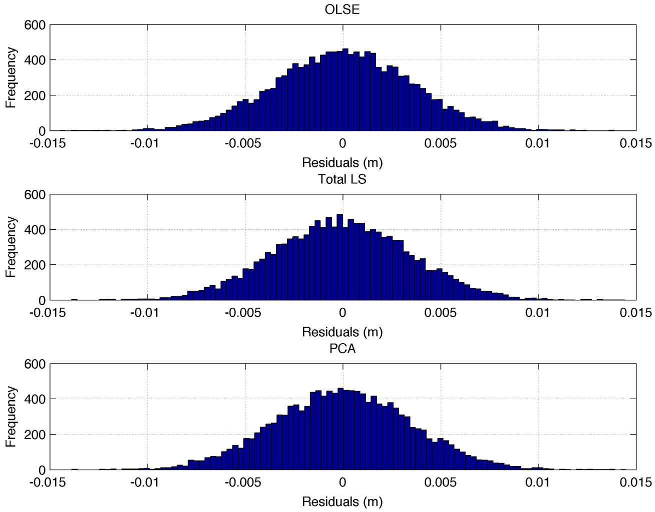

Figure 3.4: *Residual histogram per method*

The RMSE obtained for the three plane fitting methods is comparable to the individual point quality and fits the manufacturer's specifications.

The second real dataset is extracted from the same indoor area point cloud as the previous one. It contains 73 575 points. This point cloud also samples a horizontal floor. It however contains some large outliers. The three above described algorithms are used to fit a plane through this dataset. The performance of each algorithm is listed in Table 3.4.

Method	OLSE	Total LS	PCA
Number of Points	73 575		
Time (s)	0.07	0.84	0.04
RMSE (m)	0.0035	0.0036	0.0035

Table 3.4: *Performance of plane fitting algorithms on first real dataset*

A visualization of this point cloud is given in Fig. 3.5, where only a subset is plotted for better visibility. In addition, a zoomed view on the fitted planes is provided in Fig. 3.6. The respective distributions of the residuals per methods are plotted in Fig. 3.7.

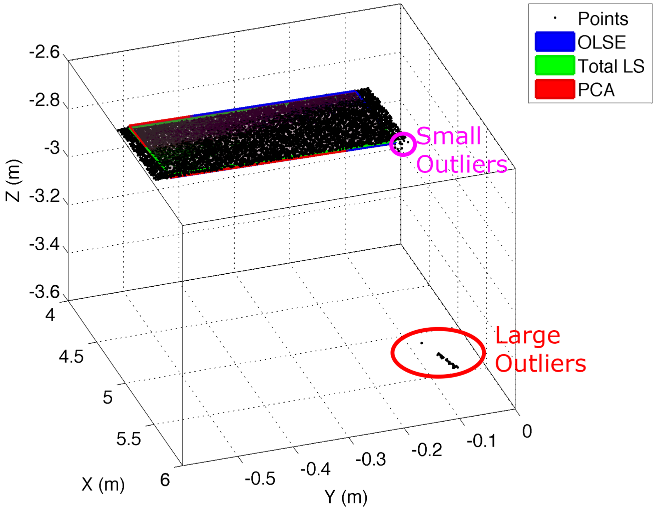

Figure 3.5: 3*D Plot of real dataset of a floor with outliers*

The first result to be observed is that the presence of outliers influences the planar parameter determination in the case of the OLSE and PCA methods. As seen on the histograms, the spread of the residuals is very small for the Total Least Squares method compared to the OLSE and the PCA methods. The second result to be observed is that the RMSE remains in the range of the individual point quality. Of course, in this example a very few number of points are outliers, therefore they did not have much influence on the overall number of points. But such a small number of points already affected the planar parameters determination.

This practical study enabled to have a better insight in the different cases of planar fitting. First, if the orientation of the plane to be fitted is known on forehand, the OLSE method is attractive as it is fast and complete. Second, if outliers are present, it is often better to make use of the Total Least Squares method, which is independant of the orientation of the plane and less sensitive to outliers. Finally, the PCA method is fast and independent of the orientation of the plane as well. However, the PCA method is more sensitive to

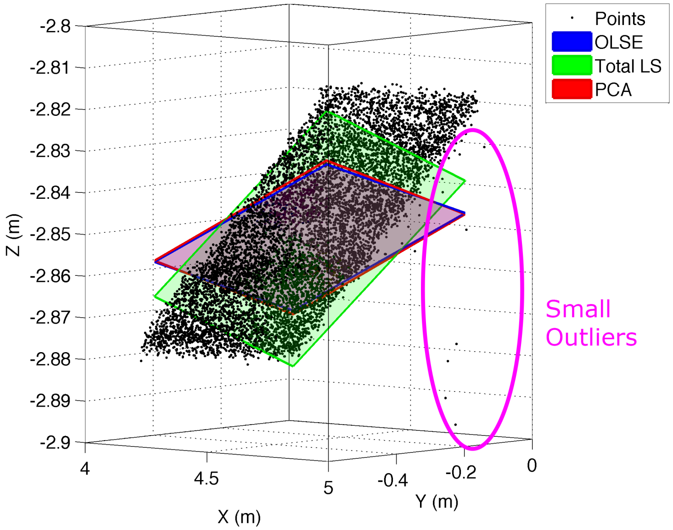

Figure 3.6: *Zoom on the 3D plot of real dataset of a floor with outliers*

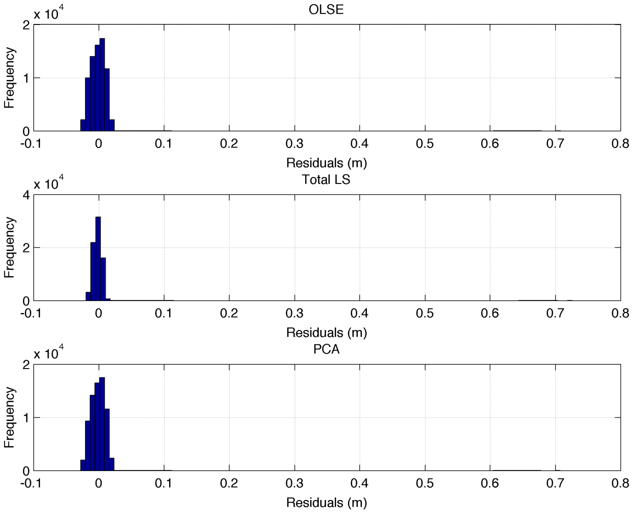

Figure 3.7: *Residual histograms per method*

outliers. This last example stresses the fact that the OLSE and the PCA methods would require a proper outliers detection before fitting a plane.

3.4 Conclusions

This chapter provides an answer to the previously stated research question: How can the quality of an individual point in a point cloud be assessed?

This chapter presented an overview of methods of planar fitting considered in this thesis. As stated previously, there are many other methods present that estimate planar features with different subtleties. These particular three methods were chosen, investigated and used because, among other reasons, they enabled us to process huge amounts of data (few million points) with a reasonable time / memory consumption.

To evaluate the global influence of the scanning geometry on the point cloud quality, standard quality describers are computed for each local planar surface estimated with n scan points. By using these quality describers, the influence of the scanning geometry is developed in the next chapters. It has been shown that the Ordinary Least Squares method is fast and provides a good quality analysis of the planar features. However, this method is dependent on the orientation of the plane. The second method described is the Total Least Squares method, which computes the planar features in a very accurate way regardless of the orientation of the plane. It is however a slow method and requires a lot of memory. A good trade-off method presented in this chapter is the Principal Component Analysis, which is fast and independent on the plane orientation. The quality description achieved by the latter is not as straightforward as the two previous methods.

Chapter 4

Scanning geometry

> *"La musique est l'arithmétique du son, comme l'optique est la géométrie de la lumière."*
> "Music is the arithmetic of sounds as optics is the geometry of light"
>
> Claude Debussy

In Chapter 2 the principles of laser scanning were presented. It is shown that there are four major influencing factors on the quality of an individual point in a point cloud. On three main factors, the user only has a limited influence. In this chapter, the last influencing factor, where the user does have control on is presented: the scanning geometry.

After defining the scanning geometry components and their effects on the point quality, the free space propagation of the laser light is presented, from which the laser range equation is derived. The quality assessment of individual points in a point cloud has been presented in Chapter 3, where details on the error modeling using planar features is provided. Based on these error models, correction coefficients are derived in this chapter.

In this chapter, the following research questions are investigated and answered:

What is scanning geometry and how does
it affect the individual point quality?

4.1 Introduction

The position of the Terrestrial Laser Scanner (TLS) and the local orientation of the surface determines the local scanning geometry, defined as the incidence angle and the range to the surface. The scanning geometry influence has been previously investigated on Airborne Laser Scanning data [137]. Although already identified in previous TLS studies [115, 116, 76, 69], these effects were not yet modeled for TLS. Characterization of the contribution of the influencing factors to the quality of scan points results in a better quality description of the point cloud. Subsequently, the propagation of well-described errors in further processing steps leads to better end-products, by means of proper weight factors per measurement for instance. As an example, the Least Squares 3D surface and curve matching method presented by Gruen and Akca [60] proposes an algorithm that enables the propagation of the errors by means of variance-covariance matrix weighting to achieve a better estimation of the registration parameters. The knowledge of the scanning geometry contribution to the measurement noise also enables the optimization of the measurement set-up to achieve a minimization of the measurement of noise for example.

In standard error analysis of TLS, the impact of the scanning geometry on the the total error budget is not well investigated. This chapter explores the effects of the scanning geometry on the point cloud quality, focusing on the incidence angle and the range of the laser beam with respect to a surface. The incidence angle is defined as the angle between the laser beam vector and the normal vector of the surface. The range is defined as the distance between the TLS and the surface. The incidence angle and the range affect the individual point Signal to Noise Ratio. The received signal level of the measurements decreases with increasing incidence angle and range. The received signal level influences the precision of the distance determination.

The theoretical models of the scanning geometry, as the incidence angle and range influence, have already been developed and presented in [148, 147, 149]. This chapter summarizes the findings and contributions published in these works.

The individual point quality is computed using Least Squares estimation techniques presented in Chapter 3. The quality of the point cloud as a whole, as specified in this chapter, is derived based on the propagation of the individual point range precision. This chapter presents an original approach to model the scanning geometry contribution to the total error budget of a TLS. The foreknowledge of the local surface geometry enables the assessment of the influence of the scanning geometry on the quality of the individual point measurements in a point cloud. The application of the developed models is presented through two practical experiments presented in Chapter 5.

4.2 Incidence Angle

Let the vector $\mathbf{P}_i = [x_i, y_i, z_i]_{i=1\cdots n}$ be defined as the laser beam vector from the laser scanner to the surface in the direction of the transmitted laser beam. The incidence angle α_i, as depicted in Fig. 4.1, is defined as the angle between one laser beam vector $\mathbf{P}_i$ and the normal vector $\mathbf{N}$ of the surface, see Eq. (4.1):

$$\alpha_i = \cos^{-1}\left(\frac{\mathbf{P}_i \cdot \mathbf{N}}{|\mathbf{P}_i|\,|\mathbf{N}|}\right). \tag{4.1}$$

The normal vector $\mathbf{N}$ is defined as the outer-pointing unit vector perpendicular to the tangent plane of the surface at the point $\mathbf{P}_i$. The angle of incidence is therefore always in the interval $\left[0 < \alpha_i < \frac{\pi}{2}\right]$. As explained in Sec. 2.1.2, the scanner measures the reflected beams at backscatter, *i.e.* the measured reflected laser light path, as depicted in Fig. 4.1, and retraces the path of the transmitted laser beam $\mathbf{P}_i$. The reflection of the light on a surface depends on the object properties, *i.e.* the material and the shape dependent anisotropy, and the scanning geometry. The reflectivity property describes the reflection of the light at a surface.

The emitted laser beam expands with a beam divergence characterized and provided by the manufacturer, as explained in Sec. 2.1.1. A laser beam hitting a surface perpendicularly results in a circular footprint on the object's surface. In this work, we assume the TLS emits Gaussian beams, which means that the distribution of the energy in the footprint is normally distributed, as depicted in Fig. 4.1. This assumption implies that for continuous surfaces the reflected signal is also Gaussian. In the perpendicular case, the energy distribution is the same along all radial sections in the footprint. Larger distances results in wider circular footprints and therefore weaker returned signals. If the laser beam is hitting the surface with a non-zero incidence angle, the resulting footprint on the surface is elongated, and therefore the energy distribution is also spread and forms an ellipse on the surface as defined in Eq. (2.4).

A lower intensity of the received signal implies a deteriorated Signal to Noise Ratio (SNR). The detection unit often applies a threshold value to detect a reflected signal. If a signal is too weak, it will not be detected as a reflected signal. A signal is weak when its magnitude is smaller than the noise level of the detection unit. For longer distances or higher incident angles, the detection of the signal becomes harder.

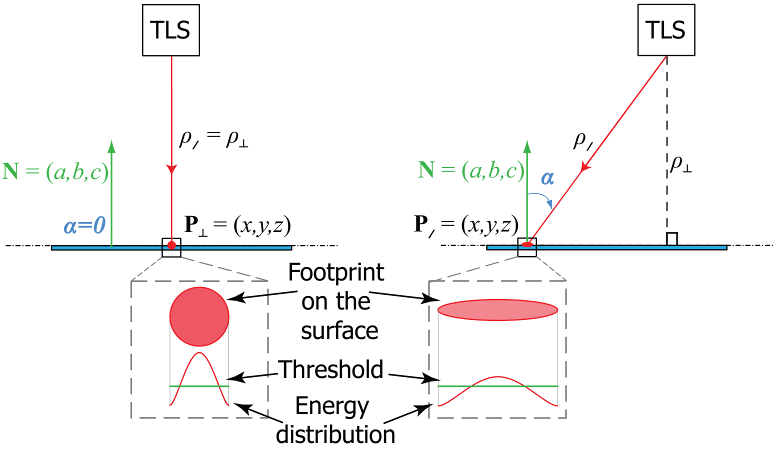

Figure 4.1: *Schematic illustration of the reflection geometry, with (left) a perpendicular laser beam ($\alpha = 0°$), (right) a laser beam with an incidence angle α to the normal $\mathbf{N}$ of a planar surface. $\mathbf{P}$ represents the point measured on the surface. The perpendicular laser beam results in a point of range $\rho_{\perp}$. The incident beam results in a point of range $\rho_{/}$. The resulting footprint shape and the energy distribution within the footprint are sketched for both situations.*

4.3 Free Space Path Propagation: towards laser range equation

The TLS technology enables accurate distance measurements to objects' surfaces by emitting laser beams at known angular directions and measuring the reflected signals in the emitted direction. The detection of the reflected signal requires a SNR of good quality, since a threshold on the level of energy of the signal determines the validity of the received signal.

To quantify the amount of the received signal with respect to the emitted signal, we describe the energy budget between the laser light transmitter and the detection unit. The energy budget takes into account the attenuation of the signal due to propagation as well as other possible signal deterioration, and enables the characterization of the SNR. As depicted in Fig. 4.2, in the case of the Laser Scanner, a two-way energy budget is conceived. In the first way, a laser beam is emitted from the transmitter towards a surface, which receives an amount of energy contained within a footprint. Depending on the surface reflectance properties, a certain amount of energy is reflected. On the way back, the energy is reflected and scattered in directions defined by the surface reflectivity properties, which are mostly different from the line of illumination. Therefore, a very small fraction of the emitted number of photon is reflected back towards the detector. Located at the same position as the laser transmitter $\mathrm{T_x}$ and placed at a distance ρ away from the surface S, the detection unit $\mathrm{R_x}$ measures the reflected signals in backscatter within a given field of view, as depicted in Fig. 4.2.

The received power $P_\mathrm{R}(\rho)$ at the receiver $\mathrm{R_x}$ is given by the Free Space Path (FSP) transmission equation, also known as the Friis equation [46]

$$P_\mathrm{R}(\rho) = P_\mathrm{T} G_\mathrm{T} G_\mathrm{R} \eta_{sys} \eta_{atm} L_\mathrm{FSP} \tag{4.2}$$

where: P_T is the transmitter power, $G_\mathrm{T}, G_\mathrm{R}$ are the transmitter and the receiver gains, η_{sys} is the transmission factor of the system, η_{atm} is the transmission factor of the atmosphere and L_FSP is the FSP loss.

The FSP loss is a function of the wavelength λ and the distance ρ of the surface:

$$L_\mathrm{FSP} = \left(\frac{\lambda}{4\pi\rho}\right)^2 \tag{4.3}$$

In the case of the Laser Scanner, a two ways link budget is considered. The first link budget is between the laser $(\mathrm{T_x})$ and the receiving surface $(\mathrm{S_{R_x}})$. The second link budget is between the radiating surface $(\mathrm{S_{T_x}})$ and the detector $(\mathrm{R_x})$.

The gain G represents the directivity of the unit, or how well the unit is capable of sending/receiving the light in one given direction. The gain G is the ratio between the power received from an ideal lossless isotropic unit (which receives power equally likely from all directions) and the power received from the actual unit. This key performance parameter is related to the effective area A_e of the considered sensor as follow:

$$G = \frac{4\pi A_\mathrm{e}}{\lambda^2} \tag{4.4}$$

The effective area $A_{\mathrm{eT_x}}$ of the transmitting sensor $\mathrm{T_x}$ is related to the distance ρ and the transmitter beam width β_T. It represents the footprint area at the surface placed at a distance ρ. Following Eq. (2.3), the footprint is at first approximated to a circle of diameter $d_{\mathrm{eT_x}} = 2\rho\tan(\beta_\mathrm{T}/2)$. As the transmitter beam width β_T is small compared to

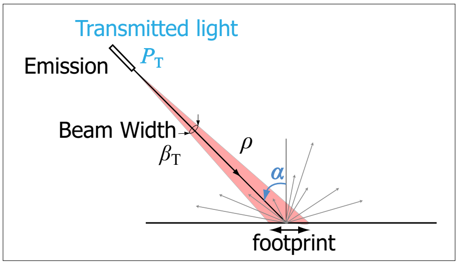

Way 1: Emission

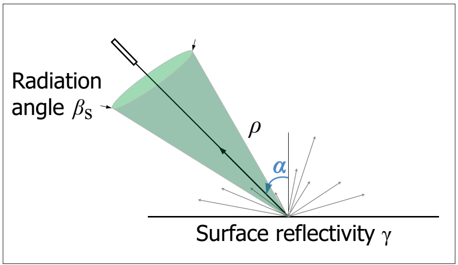

Reflection

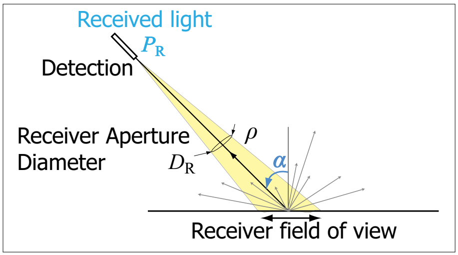

Way 2: Detection

Figure 4.2: *Two ways link budget between the receiver* (R_x) *and the transmitter* (T_x) *in a FSP propagation model.*

the distance ρ, the diameter of the footprint can be approximated to $d_{eT_x} = \rho\beta_T$. The effective area A_{eT_x} of the transmitting sensor is then defined as follow:

$$A_{eT_x} = \frac{\pi d_{eT_x}^2}{4} = \frac{\pi\rho^2\beta_T^2}{4} \tag{4.5}$$

It shows that for lower frequencies (or longer wavelengths), a bigger unit is needed to achieve a specific gain G.

The irradiance, or power per unit area U_{SR_x} at the surface at a distance ρ is related to the effective area of the transmitter A_{eT_x} and the transmitted power P_T as:

$$U_{SR_x} = \frac{P_T}{A_{eT_x}} = \frac{4P_T}{\pi\rho^2\beta_T^2} \tag{4.6}$$

U_{SR_x} is expressed in $(\mathrm{W \cdot m^{-2}})$, and it represents the power density with respect to the laser beam spreading that is captured at the surface.

The reflection of the light on a surface depends on the reflectance of the surface S. The

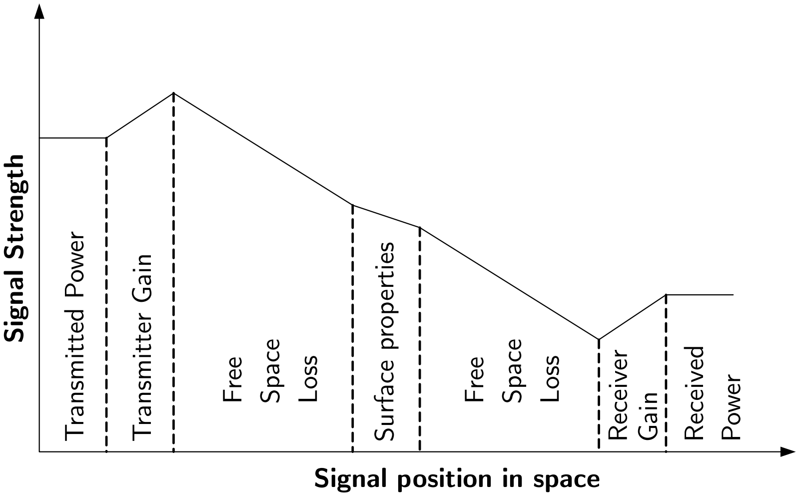

Figure 4.3: *Schematic representation of the signal propagation from the transmitter to the receiver.*

reflection of the light at a surface is described by the Bidirectional Reflectance Distribution Function (BRDF), which depends on the properties of the surface, as described in Eq. (2.5). The reflectivity property χ of the surface is defined as the ratio between the total incident power U_{SRx} and the total power scattered U_{STx}, such as:

$$\chi = \frac{U_{\mathrm{STx}}}{U_{\mathrm{SRx}}} \tag{4.7}$$

The scattered power P_{STx} at the surface is therefore a function of the surface directional properties χ, the received power at the surface U_{SRx} and the effective area A_{eSRx} of the receiving surface:

$$\begin{aligned} P_{\mathrm{STx}} &= U_{\mathrm{STx}} A_{\mathrm{eSRx}} \\ &= U_{\mathrm{SRx}} \chi A_{\mathrm{eSRx}} \\ &= \frac{4P_{\mathrm{T}}}{\pi \rho^2 \beta_{\mathrm{T}}^2} \chi A_{\mathrm{eSRx}} \end{aligned} \tag{4.8}$$

The incoming signal on the surface is partially absorbed, and partially radiated. The outgoing radiation is simplified and modeled as a cone of solid angle β_{S}, as shown on Fig. 4.2. The effective area A_{eSTx} of the transmitting surface is defined as the function of the solid angle β_{S} and the distance ρ:

$$A_{\mathrm{eSTx}} = \beta_{\mathrm{S}} \rho^2 \tag{4.9}$$

The power per unit area U_{Rx} at the receiver at a distance ρ from the surface S is related to the effective area of the transmitting surface A_{eSTx} and the radiated power P_{STx} at the surface as:

$$\begin{aligned} U_{\mathrm{R_x}} &= \frac{P_{\mathrm{ST_x}}}{A_{\mathrm{eST_x}}} \\ &= \frac{4P_{\mathrm{T}}}{\pi\rho^2\beta_{\mathrm{T}}^2}\chi A_{\mathrm{eSR_x}}\frac{1}{\beta_{\mathrm{S}}\rho^2} \end{aligned} \tag{4.10}$$

The effective area of the receiver $A_{\mathrm{eR_x}}$ is defined as surface of the disk with the receiver area diameter D_{R}:

$$A_{\mathrm{eR_x}} = \frac{\pi D_{\mathrm{R}}^2}{4} \tag{4.11}$$

The power entering the receiver is then defined as:

$$\begin{aligned} P_{\mathrm{R}} &= U_{\mathrm{R_x}} A_{\mathrm{eR_x}} \\ &= \frac{4P_{\mathrm{T}}}{\pi\rho^2\beta_{\mathrm{T}}^2}\chi A_{\mathrm{eSR_x}}\frac{1}{\beta_{\mathrm{S}}\rho^2}\frac{\pi D_{\mathrm{R}}^2}{4} \end{aligned} \tag{4.12}$$

The target cross-section represents how well an object can be detectable. It is based on its surface directional properties χ, the effective area of the receiving surface $A_{\mathrm{eSR_x}}$ and the direction of the outgoing radiations β_{S}. Let the target cross-section σ be:

$$\sigma = 4\pi\chi\frac{A_{\mathrm{eSR_x}}}{\beta_{\mathrm{S}}} \tag{4.13}$$

The power entering the receiver ($\mathrm{R_x}$) is then:

$$P_{\mathrm{R}} = \frac{P_{\mathrm{T}} D_{\mathrm{R}}^2}{4\pi\rho^4\beta_{\mathrm{T}}^2}\sigma \tag{4.14}$$

In the case of the Laser Scanner, the target area is a disk (footprint) and assumed to have Lambertian scattering behavior. The outgoing photons are then scattered in the conic area within the solid angle $\beta_{\mathrm{s}} = \pi$. Assuming that the the effective area of the receiving surface $A_{\mathrm{eSR_x}}$ is a function of the effective area of the transmitter $A_{\mathrm{eT_x}}$ and the incidence angle α, the target cross-section becomes:

$$\sigma = \pi\rho^2\beta_{\mathrm{T}}^2\chi\cos\alpha \tag{4.15}$$

where $A_{\mathrm{eSR_x}} = A_{\mathrm{eT_x}}\cos\alpha$.

Taking into account the system and the atmospheric transmission factors, the power entering the receiver is finally defined as:

$$\boxed{P_{\mathrm{R}} = \frac{P_{\mathrm{T}} D_{\mathrm{R}}^2}{4\rho^2}\eta_{sys}\eta_{atm}\chi\cos\alpha} \tag{4.16}$$

Eq. (4.16) is the laser range equation being used in this work. It is defined as a function of the scanning geometry, represented as the incidence angle α and the range ρ, the system settings, represented as the transmitted power P_{T} and the receiver area diameter D_{R}, the surface reflectivity property χ and the transmission factors $\eta_{sys}\eta_{atm}$.

4.4 Signal deterioration

In the previous section, by considering the two ways link budget between the receiver and the transmitter, the total power entering the receiver P_{R} has been defined as in Eq. (4.16), which among other parameters, depends on the geometry of the surface to be measured.

It is seen that the emitted signal P_T undergoes degradation, which results in a weaker signal. First, Eq. (4.16) shows that the SNR of a laser return deteriorates with the cosine of the incidence angle α. Additionally, the SNR deterioration is inversely proportional to the range ρ squared.

In this section, these two types of deteriorations are presented in detail, for which a coefficient of contribution is derived per type of deterioration.

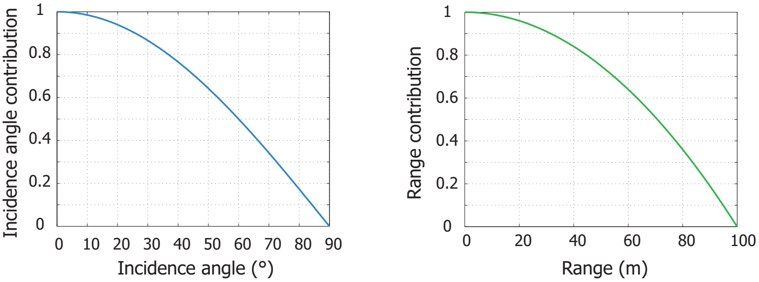

Figure 4.4: *Effect of increasing incidence angle and range to the signal deterioration. (left) Plot of the the signal deterioration due to increasing incidence angle α according to Eq.* (4.23)*, (right) plot of the signal deterioration due to increasing ranges ρ according to Eq.* (4.24)*, with* $\rho_{min} = 0$ *m and* $\rho_{max} = 100$ *m.*

4.4.1 Signal deterioration due to incidence angle

Assume the equation of a plane is expressed in Cartesian coordinates to be defined as in Eq. (4.17).

$$d = ax + by + cz, \tag{4.17}$$

where the normal vector of the planar surface is defined as $\mathbf{N} = [a, b, c]$ and d is the distance of the plane to the origin. By substituting the Cartesian coordinates of a point $\mathbf{P}$ with its spherical coordinates $\mathbf{P}_s = [\theta, \varphi, \rho]$ following Eq. (2.12), the equation of a plane Eq. (4.17) is expressed as in Eq. (4.18).

$$d = \rho\left(\cos\phi\,(a\cos\theta + b\sin\theta) + c\sin\phi\right). \tag{4.18}$$

The distance d of the plane to the origin, depicted as $\rho_\perp$ in Fig. 4.1, can also be expressed as a function of the incidence angle α and the range measurement ρ to the surface, following Eq. (4.19):

$$d = \rho\cos\alpha. \tag{4.19}$$

As seen in Chapter 3, by fitting planes to the points, the distance between the points and a planar fit is minimized, resulting in residuals $\hat{\mathbf{e}}_\rho$ per point, which are in the direction of the laser beam if the Least Squares plane fitting method based on homogeneous equations is used.

Following the same principle as in Eq. (4.19), the orthogonal residuals per point $\hat{\mathbf{e}}_d$ are a function of the residuals per point $\hat{\mathbf{e}}_\rho$ in the direction of the laser beam and the incidence angle α, following Eq. (4.20):

$$\hat{\mathbf{e}}_d = \hat{\mathbf{e}}_\rho \cos\alpha. \tag{4.20}$$

The standard deviation $\sigma_{\hat{\mathbf{e}}_\rho}$ of the noise level $\hat{\mathbf{e}}_\rho$ in the direction of the laser beam is defined as Eq. (4.21):

$$\sigma_{\hat{\mathbf{e}}_\rho} = \sqrt{\frac{\hat{\mathbf{e}}_\rho^T \hat{\mathbf{e}}_\rho}{n-m}}, \tag{4.21}$$

where m represents the number of estimated parameters of the plane fitting and n is the number of points.

Using the law of propagation of uncertainty, the orthogonal distance standard deviation $\sigma_{\hat{\mathbf{e}}_d}$ is expressed as a function of the range standard deviation $\sigma_{\hat{\mathbf{e}}_\rho}$ following Eq. (4.22):

$$\sigma_{\hat{\mathbf{e}}_d} = \sigma_{\hat{\mathbf{e}}_\rho} \cos\alpha \tag{4.22}$$

The effect of the incidence angle on a measurement can be quantified by means of a "contribution coefficient". In Fig. 4.4, the theoretical contribution of the incidence angle to the signal deterioration is plotted, that follows, according to Eq. (4.22), the function $\cos\alpha$. The effect of the incidence angle on the range measurement is expressed as a coefficient $c_I(\alpha)$ of values ranging from 1 to 0 for incidence angles α ranging from 0° to 90°, as defined in Eq. (4.23):

$$\boxed{\begin{aligned} c_I(\alpha) &= \cos\alpha \\ &= \cos\phi\,(a\cos\theta + b\sin\theta) + c\sin\phi \end{aligned}} \tag{4.23}$$

The model of the incidence angle contribution $c_I(\alpha)$ expresses the effect of incidence angle on the range measurement noise based only on the point cloud angular information (θ,ϕ) and a local surface normal vector $\mathbf{N}$. This incidence angle factor approach enables an easier incorporation of uncertainties using error propagation techniques. Furthermore, the foreknowledge of the normal vector per point allows the computation of an incidence angle per scan point. This model is applicable to planar surfaces, for *e.g.* a CAD model, on the condition that the normal vector per scan point is known.

4.4.2 Signal deterioration due to range

The received amount of power decreases with increasing scan range, as described by the laser range equation Eq. (4.16), *i.e.* the effect of the range to the total noise level is proportional to the square of the range. Assuming that ρ_{min} is the minimum range for which the backscattered signal can be detected, and ρ_{max} is the maximum range measurable without ambiguity, the contribution of the range on the measurement deterioration is modeled by a coefficient $c_R(\rho)$ of values ranging from 1 to 0 for ranges ρ ranging from ρ_{min} to ρ_{max}, as defined in Eq. (4.24).

$$\boxed{c_R(\rho) = \frac{\rho_{max}^2 - \rho^2}{\rho_{max}^2 - \rho_{min}^2}} \tag{4.24}$$

where ρ_{min} and ρ_{max} are set depending on the laser scanner in use.

The model of the range contribution $c_R(\rho)$ expresses the effect of the range on the precision of the range measurement noise based on the type of laser scanner in use and its measurement limitations. This coefficient is mainly derived from a first calibration of the tool in use. This coefficient show how reliable the measurement is depending on the measured range. This coefficient has been developed and tested with phase based scanners. It is however expected to be applicable in the same way for the pulse based scanners.

It will be shown in Chapter 5 how Eq. (4.23) and Eq. (4.24) allow us in a practical setting to decompose the noise into components by measurement range and by incidence angle.

4.5 Conclusions

In this chapter, the following research question was investigated and answered: What is scanning geometry and how does it affect the individual point quality?

First, in this chapter, the scanning geometry has been defined, by using two parameters: the incidence angle and the range. It is seen that the shape of the footprint of the laser light on a surface depends on those two parameters.

To quantify the amount of received light with respect to the emitted light and the elements contributing to a signal deterioration, a two ways energy link budget was described, which led to the definition of the total power entering the receiver. It is shown that this power depends greatly on the scanning geometry. The influence of the scanning geometry is shown to be a major influencing factor, which is often taken into account in the current point quality studies [127, 160, 113].

It is shown in Chapter 5 that by considering the influence of scanning geometry on the signal to noise ratio, the increase in measurement noise with increasing incidence angle and increasing ranges is successfully modeled. By reconstructing the original spherical point cloud measurements, the models quantify the scanning geometry contribution as a function of the point cloud angular information and locally estimated planar parameters.

The presented approach allows the isolation of the contribution of noise induced by the scanning geometry, based only on point cloud data. No additional or external measurements are needed. The contribution of the two scanning geometry parameters on the point quality has been quantified using contribution coefficients. Both models of contribution express the reliability of the incidence angle and range on the measurement noise as a coefficient ranging from 1 to 0, as 1 means the measurement is reliable and 0 translates a not reliable measurement. These models are currently being widely used [77, 40, 34] and applied in many different studies such as deformation modeling in man-made structures as well as natural sites using scanning geometry constraints [127, 96, 80, 48, 100, 151].

In Chapter 5, the scanning geometry is further investigated in practical situations.

CHAPTER

5

Total error assessment in practice

> "For the things we have to learn before we can do them, we learn by doing them."
>
> Aristotle, The Nicomachean Ethics

A terrestrial laser scanner measures the distance to an object surface with a precision in the order of millimeters. The quality of the individual points in a point cloud, although directly affecting standard processing steps like point cloud registration and segmentation, is still not well understood. In this chapter the influence of the scanning geometry on the individual point precision or local measurement noise is evaluated. The local scan geometry depends on the distance and the orientation of the scanned surface, relative to the position of the scanner. The local scanning geometry as shown in Chapter 4 is parameterized by two main parameters, the range, i.e. the distance from the object to the scanner and the incidence angle, i.e. the angle between incoming laser beam and the local surface normal.

In this chapter, the following research question is investigated and answered:

How does the scanning geometry affect
the total point cloud quality in practice?

In this chapter it is shown that by studying the influence of the local scan geometry on the signal to noise ratio in a real point cloud, the dependence of the measurement noise on range and incidence angle can be successfully characterized if planar surfaces are observed. This work is presented in [146, 147] and [148]. Two practical measurement set-ups are presented. First, a controlled set-up using a plate mounted on a goniometer is used to examine the effects of the scanning geometry. The plate is first rotated to enable the study of the effect of the incidence angle. Then, the same experiment is reproduced at different distances to the scanner, resulting in a complete study of the influence of both incidence angles and range. As a second measurement set-up, the implications of the models presented in Chapter 4 are demonstrated further by comparing two point clouds of a small room, obtained from two different scanner positions: a center position and a corner position. From these practical assessments, it is shown in Chapter 6 that it is possible to optimize measurement set-ups in such way that the measurement noise due to bad scanning geometry is minimized, which therefore contributes to a more efficient acquisition of point clouds of better quality.

5.1 3D point cloud analysis in practice

After the acquisition of a 3D point cloud (see Sec. 2.1), some post processing steps are needed to estimate the scanning geometry per point. In this section, we present the steps we followed in this work. There are of course many other ways to extract the scanning geometry from a point cloud. The presented work flow is one way of doing it, which enabled us to process large amount of points in a reasonable amount of time and memory.

5.1.1 Segmentation of a point cloud

In Sec. 2.2.3, the concept of segmentation was introduced. The point cloud $\mathbf{P} = [x, y, z]$ is first segmented based on a planar feature extraction algorithm. Several segmentation methods are presented in Sec. 2.2.3.

In this thesis, the planar surfaces are extracted using a gradient based range image [55]. A range image enables a 2.5D representation of the dataset, where each pixel value corresponds to the distance ρ of an observed point from the scanner. This method estimates, for each measurement considered as an image pixel[1], the parameters of a normal vector in a spherical coordinate system, namely the two angles (α, β) and the perpendicular distance (γ) between the plane the measurement belongs to and the origin, as shown in Fig. 5.1. This estimation is based on the scan parameters and horizontal and vertical gradient images[2].

Points with similar planar parameters (α, β, γ) are considered to be part of the same plane, *i.e.* segment. For the experiments presented in this work, small segments are filtered out from the analysis. We consider a segment to be small when it contains less than 10 points. This segmentation algorithm is based on the range image and therefore does not take into account the intensity measurements.

---

[1] The point cloud is represented as a range image, where every image pixel represents the angular position following the scanning resolution, and is colored following the measured range.

[2] A gradient image provides the directional changes in pixels of an image. It enables the extraction of edges of objects and local contrasts.

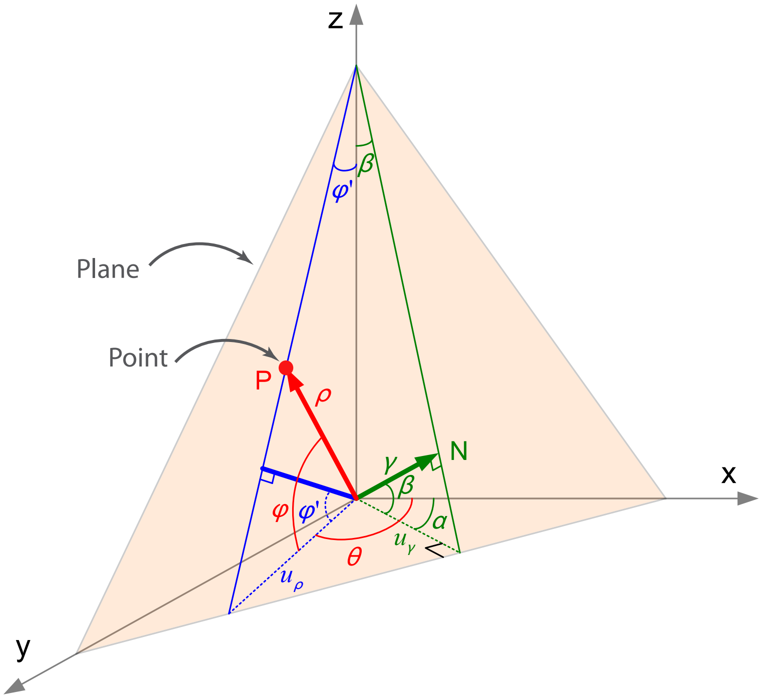

Figure 5.1: *Relationship between scan angle and normal vector orientation used for the segmentation of point cloud with respect to planar features. A point* $P = [\theta, \varphi, \rho]$ *is measured on the plane with the normal parameters* $N = [\alpha, \beta, \gamma]$*. Different angles used for the range image gradients are plotted.*

5.1.2 Data representation: Net-view

3D laser scans can be seen as panoramic images. To have a better and easier visualization of the experimental results, the 3D point cloud is represented as a 2D net-view, such that it allows a real 2.5D visualization of the scene when colored. The relative scale of the objects in the scene is then maintained. Fig. 5.2 depicts the common example of the net-view of a dice consisting of six planar surfaces.

In this work, the XY plane is usually taken as the reference plane of the net-view representation. The segmentation of the captured point cloud results in groups of points having similar planar features. The knowledge of surface normals enables rotations of the points belonging to the planar surface to the XY plane.

5.1.3 Patch subdivision

To have a better insight into the local error behavior and the local quality of points of similar scanning geometry, each segment is divided into small patches. This subdivision results in patches containing only a small number of points, but enough points to apply a plane fitting algorithm. The least squares estimation of the local planar features presented

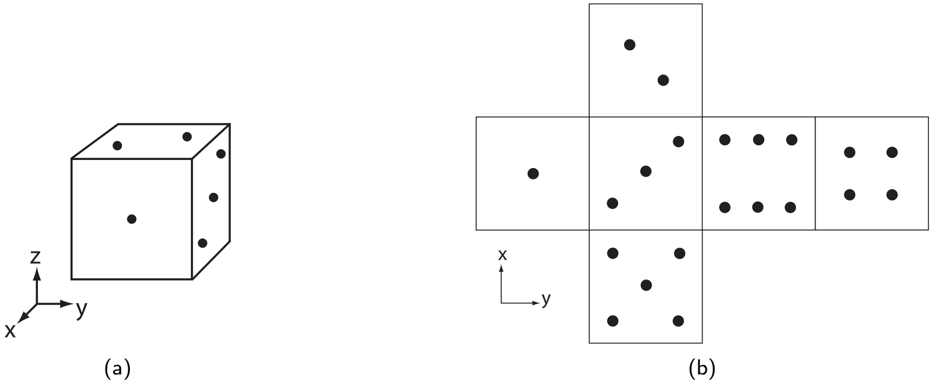

Figure 5.2: *Schematic representation of patch subdivision **(a)** Schematic* $3D$ *representation of a cube, **(b)*** $2D$ *Net-view of the cube.*

in Chapter 3 is less consuming in memory and computation time for smaller datasets. Two different patch subdivisions are applied to point clouds in this work. The first method described in Sec. 5.1.3.1 separates the point cloud into areas based on Cartesian coordinates. The second subdivision described in Sec. 5.1.3.2 is based on the spherical representation of the point cloud. These two different ways of patching the data provide a very different insight in the quality of the local data.

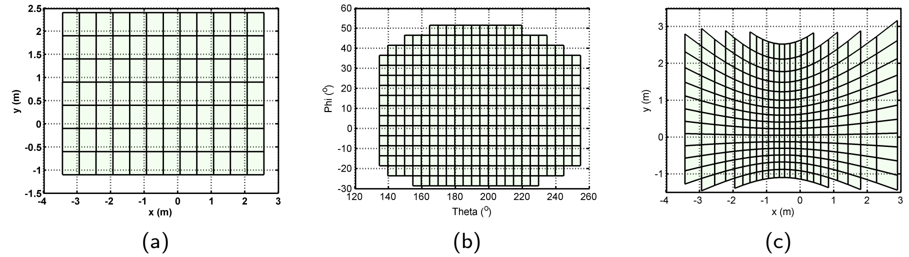

Figure 5.3: *Schematic representation of patch subdivision **(a)** Cartesian patches,* 50×50 *cm grid. **(b)** Spherical patches,* $5^\circ\times5^\circ$ *grid. **(c)** Spherical patches represented in the Cartesian domain.*

5.1.3.1 Cartesian patch subdivision

Based on the net-view presented previously, it is very easy to create a 2D grid of the point cloud, with a specified patch size, as depicted in Fig. 5.3(a). The point cloud lies on the XY reference plane. The advantage of this type of subdivision is that the patch area remains the same for the entire point cloud. As the point density varies with the orientation and the distance of the patch with respect to the laser scanner, the number of points per patch is varying as well.

5.1.3.2 Spherical patch subdivision

As seen previously in Sec. 2.1.4, the TLS captures 3D measurements in a spherical way. Laser beams are sent with regular horizontal and vertical angle increments. The measurements consist of the two angular positions (θ,ϕ) and a distance (ρ) for each laser beam received. The point cloud is divided into smaller rectangular patches in the spherical domain, as depicted in Fig. 5.3(b). This spherical subdivision results in patches containing the same number of points per patch as the coordinate system is the one used by the scanner in acquiring its points. Therefore, the patch size varies with respect to the orientation and the distance of the considered surface, as illustrated in Fig. 5.3(c). In Fig. 5.3(b) the spherical patches are shown in the spherical domain and in Fig. 5.3(c) the same patches are shown in Cartesian domain. Depending on the orientation of the surface, the representation of such spherical grid into the Cartesian coordinate system differs. In the case plotted in Fig. 5.3(c), the surface is placed at a almost perpendicular orientation with respect to the scanner.

5.1.4 Planar features per patch and incidence angle per point

Once the point cloud has been segmented and patched, the planar features of each patch are extracted by applying a planar fitting algorithm. In this thesis, we presented three methods of planar feature extraction methods in Chapter 3. In the rest of this chapter, we choose to make use of the Total Least Squares method presented in Sec. 3.2.3. After extracting the planar parameters, the computation of the incidence angles at individual points is derived from Eq. (4.1).

5.1.5 Theoretical number of points per Cartesian patch

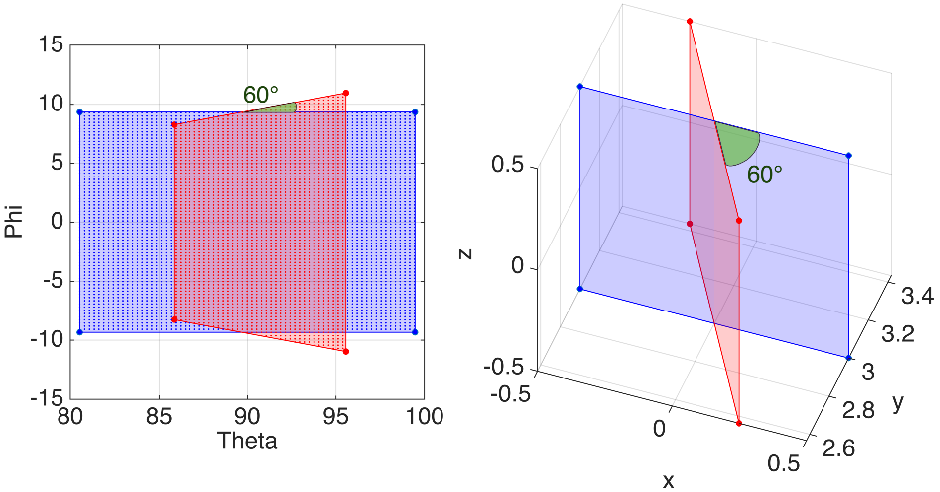

Figure 5.4: *Theoretical number of points. Practical example of a plate of* 1×1 *m placed at* 3 *m, oriented at* 0° *and being rotated at* 60°*.*

As shown in Fig. 5.4, the scanner captures points on the considered surface in a spherical way *i.e.* range measurements obtained at fixed angular increments, see Chapter 2. The scanner emits a regular grid of laser rays that is independent of the surface that is scanned. The number of pulses locally hitting the surface depends on the scanning geometry, namely the orientation and distance of the surface with respect to the scanner. In this theoretical example, the plate being rotated at 60° (red plate in Fig. 5.4) covers less surface in the spherical domain than the perpendicular one (blue plate in Fig. 5.4). Therefore, the number of points recorded on the red plate is smaller.

In Fig. 5.5, the theoretical number of points per patch of 20×20 cm is shown. [98] presents a method for computing the theoretical number of points on a surface, which is based on the scanning specifications of the laser scanner in use, in this case the FARO LS880 [44]. The main parameters to consider when determining the number of points on a surface are the vertical and horizontal scanning angle increments and the spherical coordinates of the borders of the considered surface. In Fig. 5.5 on the left, the number of points with respect to the orientation of the patch of 20×20 cm and its distance to the scanner is plotted. On the right, the theoretical number of points per patch of 20×20 cm is plotted, assuming that the patch is at a near perpendicular orientation with respect to the Laser Scanner. In this theoretical plot, the scanning specifications applied in the case study are used, namely a scanning resolution of $1/5$ of the total resolution of the scanner (see Table 2.1).

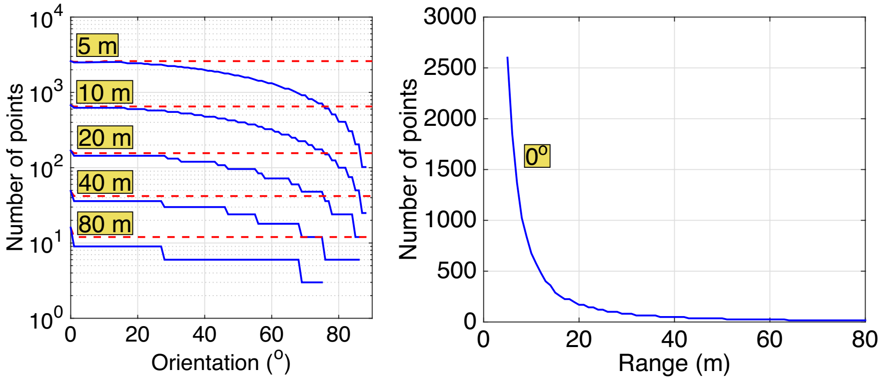

Figure 5.5: *Theoretical number of points. (left) Number of points with respect to the orientation of the patch and the distance.*

In Fig. 5.5, it is shown that the theoretical number of points decreases dramatically for orientations of the patch greater than 70°. It is also shown that when considering smaller ranges, *e.g.* smaller than 20 m, the number of points per patch is very high. As shown in Fig. 5.5, small variations in small ranges result in a great variation in number of points. For example, at 5 m, the number of points of a near perpendicular patch of 20×20 cm is 2601. When this patch is placed at 10 m, the number of points decreases to 676. When placing it further away to 20 m, the number of points on the patch is only 169. When considering bigger ranges, *e.g.* greater than 40 m, the variation in number of points is smaller. When this patch is placed at 40 m, the number of points decreases to 49. When placing it further away at 60 m, the number of points is 25. The number of points per considered area is an important aspect when fitting plane and assessing the quality of the area. The redundancy of information is important to obtain a reliable plane model. As shown in Chapter 6, the minimum number of points per unit area is a constraint a user can specify and require when scanning a scene.

5.2 Plate experiment measurements

Two different sets of experiments were conducted to validate the models developed in Chapter 4. A first set of experiments is performed to examine the effect of varying incidence angle on the noise level at a fixed distance to the scanner. In the second set of experiments, the distance to an object is varied as well. The influence of the scanning geometry on the scan quality is analyzed through experiments conducted under near laboratory conditions[3] using the TLS HDS6000 from Leica [85]. Both experiments are performed on a 1×1 m white coated plywood board. The board used in this experiment is not reflecting in a perfect isotropic way, but it is considered to be almost Lambertian. This board is mounted on a tripod via a screw clamp mechanism provided with a goniometer that enables the mechanism to rotate horizontally with an angular resolution of $2°$, as depicted in Fig. 5.6. The first experiment focuses on the influence of the incidence angles on the quality of the point cloud. The second experiment combines the influence of the incidence angles and the range.

The incidence angles per point are computed locally by first fitting a plane through the points as shown in Chapter 3, then using the methods described in Chapter 4. The angle given by the goniometer only provides a rough indication on the orientation of the plate.

Figure 5.6: *Reference plate measurement set-up. A white coated plywood board is mounted on a tripod via a screw clamp mechanism provided with a $2°$ precision goniometer.*

---

[3] The experiments were conducted in the basement of a building, where the tempetrature and humidity were controlled and monitored, and where there was no daylight.

5.2.1 Experiment 1: Influence of changing incidence angle on the noise level

The first experiment investigates the incidence angle contribution on the range measurement. The experimental board is placed at a fixed distance of 20 m from the TLS. The board is rotated from 0° to 80° in steps of 10°. At each orientation step, the board is scanned, as depicted in Fig. 5.7. The following analysis is based on 9 scans, containing between 4900 and 38500 points per scan depending on the orientation of the plate with respect to the laser beam.

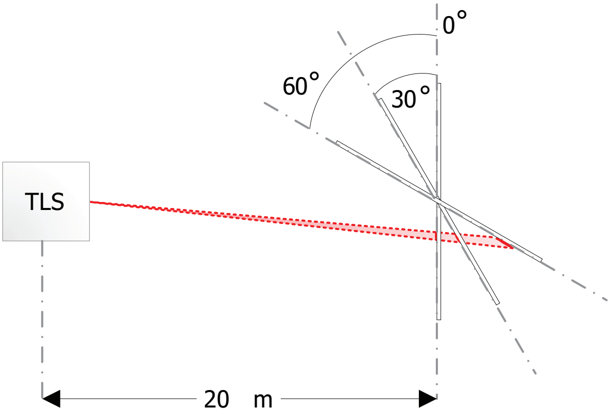

Figure 5.7: *Measurement setup of experiment 1. A board placed at a fixed distance of 20 m is scanned at varying incidence angles. A representative laser beam is depicted in red.*

First the planar parameters $\mathbf{N}$ are estimated for each scan using Total Least Squares as described in Sec. 3.2.3. The estimation uses all points of the considered scan of the board. A noise level $\hat{\mathbf{e}}_\rho$ in the direction of the laser beam is then computed for each point in the scan following Eq. (3.22). The orthogonal noise level $\hat{\mathbf{e}}_\mathbf{d}$ is derived for each point in the scan following Eq. (4.20). The incidence angle α per point is computed based on the estimated planar parameters $\mathbf{N}$ and the laser beam vector $\mathbf{P}$, as described in Eq. (4.1). Fig. 5.8 shows the standard deviation $\sigma_{\hat{e}_\rho}$ with respect to the incidence angle for each scan, derived from the noise level in the direction of the laser beam per point $\hat{\mathbf{e}}_\rho$ following Eq. (4.21). It also shows the standard deviation $\sigma_{\hat{e}_d}$ with respect to the incidence angle for each scan, derived from the orthogonal noise level per point $\hat{\mathbf{e}}_\mathbf{d}$ following Eq. (4.20). Note that for each plate orientation, the number of points considered decreases with increasing incidence angles as seen in Sec. 5.1.5.

The influence of the incidence angle is clearly visible and follows the theoretical incidence angle effect described in Section 4.4.1. A larger standard deviation of errors in the direction of the laser beam is observed for larger incidence angle. Subsequently, the noise level induced by the incidence angle α is removed from the noise level $\hat{\mathbf{e}}_\rho$, providing the remaining standard deviation $\sigma_{\hat{e}_d}$ in Fig. 5.8. The orthogonal noise level is almost independent of the incidence angle. The orthogonal noise level $\hat{\mathbf{e}}_\mathbf{d}$ shows a slight increase at 10°, followed by a small continuous decrease of errors until 70° and a consecutive increase towards maximal incidence angles. This characteristic trend could be partially explained by the scattering behavior of the surface with respect to incoming light, de-

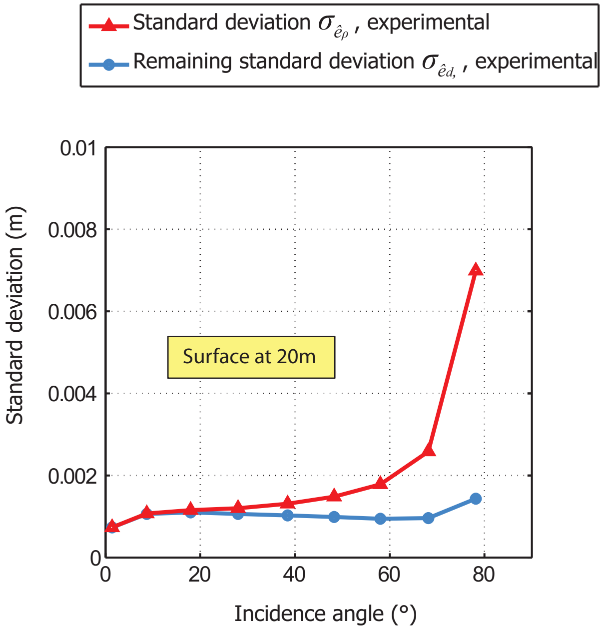

Figure 5.8: *Standard deviation with respect to the incidence angle of the surface, given a fixed scanner position. The standard deviation of the noise in the direction of the laser beam* $\sigma_{\hat{e}_\rho}$ *is plotted in red. The orthogonal standard deviation* $\sigma_{\hat{e}_d}$*, after removal of the incidence angle effect is plotted in blue. At every plate orientation, the standard deviations are computed using all the points scanned on the plate.*

scribed by the Bidirectional Reflectance Distribution Function of the surface, which is not perfectly Lambertian. Lichti [90] also observes such a characteristic trend and suggests to use an a-priori threshold of a maximum incidence angle of 65° for removing not reliable measurements.

5.2.2 Experiment 2: Simultaneous influence of incidence angle and distance.

This experiment investigates the simultaneous influence of distance and incidence angle on the point cloud quality. The experimental board is placed at distances ranging from 10 m to 50 m in steps of 10 m and one additional low distance placement at 5 m from the TLS. At each distance placement, the experiment described before in Sec. 5.2.1 is conducted. As depicted in Fig. 5.9, the board is scanned at each distance placement and for each rotation. This experiment consists of 54 scans captured successively at around the same time.

However, only 45 scans are captured in a good enough quality. For higher distances and larger rotation angles, the standard deviation obtained was significantly higher than 5 mm. The number of points measured at these extreme situations decreased to less than 100 points per scan, as depicted in Fig. 5.10. At 60° and 50 m distance, only the points

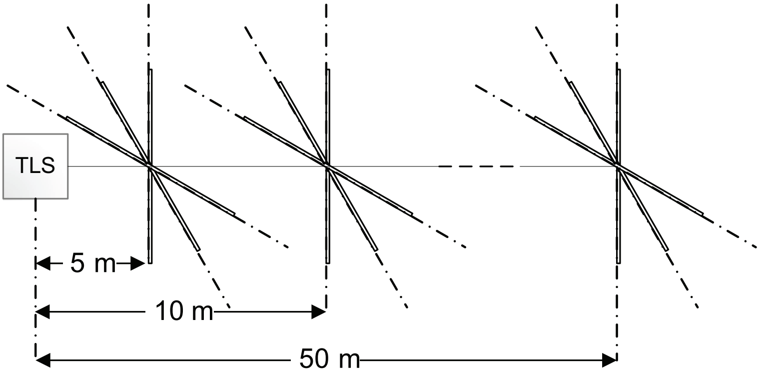

Figure 5.9: *Measurement setup of experiment 2. A board is scanned at varying distances and at varying orientations.*

on the border of the board are measured, no points on the board are measured because of the high incidence angle and range of the measurements. The return signal strength is too low for the detection unit to be detected. These extreme cases appeared to be irrelevant for the analysis and are therefore not presented in the following study. For the remaining 45 scans, the point cloud contains between 3 100 and 150 500 points depending on distance and orientation of the surface.

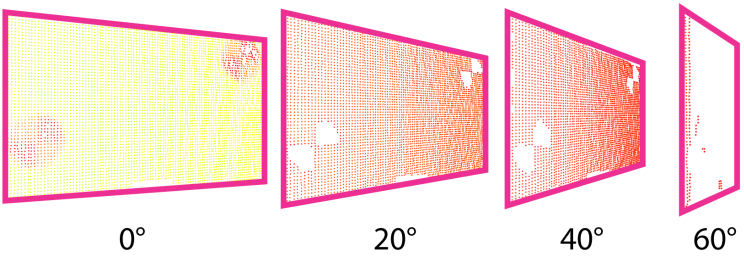

Figure 5.10: *Point clouds of the board colored with intensity. The board is placed at* 50 *m from the TLS. The presented inclinations are from left to right* 0°*,* 20°*,* 40° *and* 60°*. The board is outlined in bold lines. At* 60° *and* 50 *m distance, only the points on the border of the board are measured, no points on the board are measured because of the high incidence angle and range of the measurements.*

The standard deviation of the residuals $\sigma_{\hat{e}_\rho}$ is derived for each scan in the manner described in Sec. 5.2.1. The planar parameters are estimated using all the points in a scan. Two different effects of the scanning geometry are isolated by this experiment.

5.2.2.1 Isolation of incidence angle effect

Fig. 5.11 shows the standard deviation of the residuals $\sigma_{\hat{e}_\rho}$ with respect to the distance from the surface. As in Sec. 5.2.1, it is clearly visible that for larger incidence angles, larger noise levels are obtained.

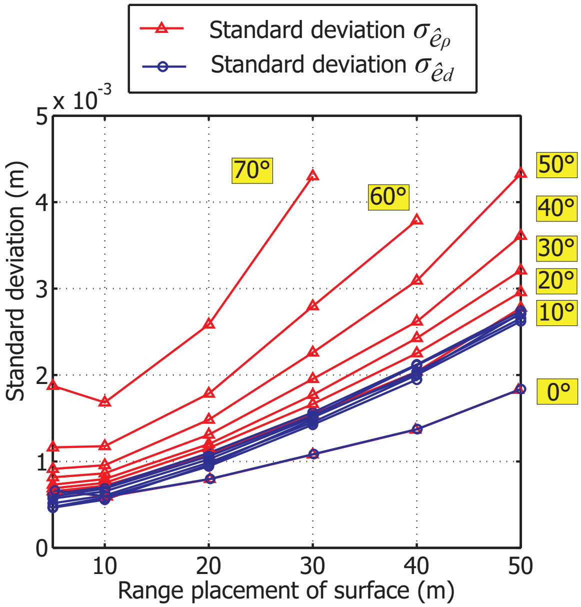

Figure 5.11: *Standard deviation with respect to the incidence angle of the surface, given 6 different scanner positions. The standard deviation of the noise in the direction of the laser beam* $\sigma_{\hat{e}_\rho}$ *is plotted in red. The orthogonal standard deviation* $\sigma_{\hat{e}_d}$*, after removal of the incidence angle effect following Eq.* (4.20)*, is plotted in blue.*

The incidence angle effects are removed from the standard deviation of the residuals $\sigma_{\hat{e}_\rho}$ using the method described in Sec. 4.4.1. The standard deviation of the orthogonal noise $\sigma_{\hat{e}_d}$ is almost independent of incidence angle and follows the same increasing trend for increasing distance from the board to the scanner. The errors obtained for an orientation of the plate at 0° seem to be shifted in comparison with the global trend observed for other incidence angles. Low incidence angles result in almost circular footprints on the surface as shown in Chapter 4. In this case, a near optimum signal is returned, with a large magnitude. A possible explanation for the phenomenon observed for low incidence angles could be as follows: the detection system might adapt the recording system to this optimal measurements by rescaling the measurements because it is more likely to saturate the detection system when the laser beam hits a surface in a nearly perpendicular way [71].

5.2.2.2 Isolation of distance effect

It is shown that with increasing range, the measured noise level increases. Fig. 5.12 shows the remaining standard deviation after removal of incidence angle effects. The range effects are removed from the remaining noise levels using the approach described in Section 4.4.2.

A larger standard deviation is observed for larger ranges. The noise level induced by the range effect is removed from the noise level $\hat{\mathbf{e}}_\rho$, shown as the remaining standard deviation

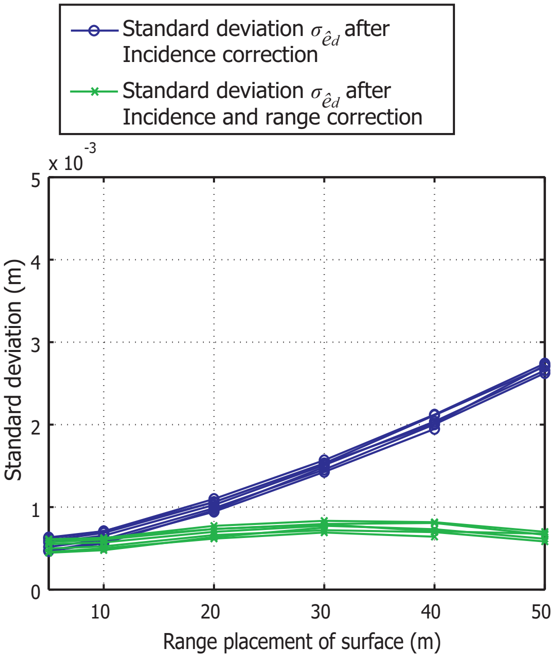

Figure 5.12: *Standard deviation of noise level given 6 different scanner positions. The standard deviation of the orthogonal noise* $\sigma_{\hat{e}_d}$ *after correction of the incidence angle effect is plotted in blue. The orthogonal standard deviation* $\sigma_{\hat{e}_d}$*, after removal of the incidence angle effect and the range effect following Eq.4.23, is plotted in green. The standard deviation of the* $0°$ *case is not plotted due to its particular properties.*

$\sigma_{\hat{e}_d}$ in Fig. 5.12. The additional parameters of the range contribution model in Eq. (4.24) are set with respect to the TLS in use in this experiment, namely the Leica HDS6000, resulting in $d_{min} = 0$ m and $d_{max} = 80$ m. The remaining error is almost independent of the range. A slight increase of the global trend is observed from 10 m to 30 m, which can be avoided by fine tuning the additional parameters in Eq. (4.24).

5.3 Room experiment measurements

5.3.1 Measurement set-up and processing steps

In this section, the influence of scanning geometry is isolated and quantified for a typical point cloud representing a closed and empty room, as depicted in Fig. 5.13. As the captured point cloud contains more than 20 million points, the determination of planar parameters and the isolation of the scanning geometry contribution comprises additional steps described further in this section.

Two walls and the floor of the room are analyzed in this study. The floor of this room is covered with light colored linoleum and the walls are painted in white and have very smooth surfaces. This experiment is conducted using the LS880 HE TLS from FARO.

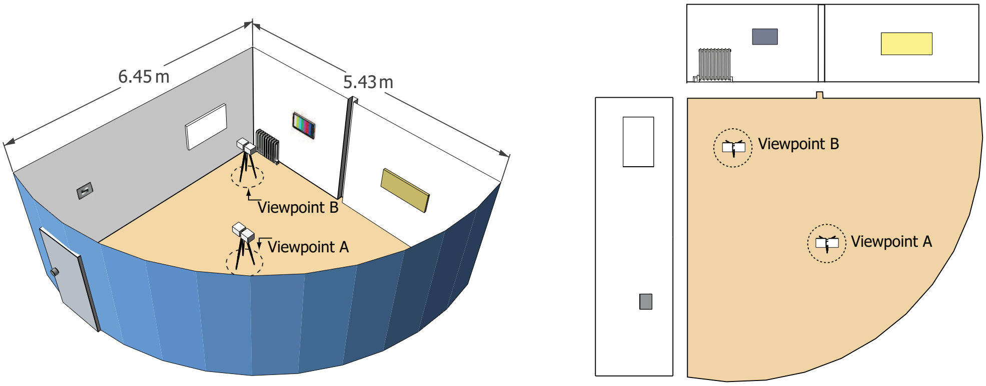

Figure 5.13: *Measurement Set-up of the standard room measurement using the location of the two view points: viewpoint A in the center and viewpoint B in a corner. (left) 3D representation of the room, with the two viewpoints locations, (right) 2D net-view representation of the room with the two walls and the floor, and the two viewpoints locations.*

The resolution was set at $1/4$ of the full resolution [44]. The laser scanner scans the room from two different viewpoints. The first viewpoint (viewpoint A) is approximately situated in the middle of the room. From the viewpojnt A, the resulting point cloud contains 1225307 points. The second viewpoint (viewpoint B) is located near the corner formed by the two planar walls. From the viewpojnt A, the resulting point cloud contains 1591288 points.Both scans were acquired on the same day, with similar environmental conditions. The position of the TLS is recognizable in scans of the floor because the TLS cannot scan underneath its position. Four test plates that were used in previous studies are added on the two planar walls. Two reference test charts (ESSER TE106 and TE109) for color and grey scale were previously used in a remission experiment [19]. A white coated plywood and a medium-density fibre board were used before in a scan angle experiment [149].

In this work, to determine the incidence angle of a surface, the point cloud is first segmented according to coarse planar features [55]. The segmentation process divides the scanned scenery into areas having similar planar parameters. Resulting segments are spatially different in size and point density. The segmentation results in four main segments: the floor and three wall pieces, as depicted in Fig. 5.14. One of the walls is divided into two different segments. For an easier visualization of the experimental results, the point cloud is represented as a net view, allowing a real 2.5D visualization of the scene in such a way that the relative scale is maintained, as depicted in Fig. 5.14. In this work, the XY plane is chosen as reference plane of the net-view representation.

To have a better insight into the local error behavior and the local quality of points of similar scanning geometry, each segment is subdivided into small patches as described in Sec. 5.1.3. First, each segment is divided into small Cartesian patches of 20×20 cm, as shown in Sec. 5.1.3.1. As discussed previously, this type of patch provides a regular grid area over the whole segment. However the number of points per patch varies with respect to the orientation and the distance to the scanner.

Then each segment is divided into small spherical patches of $5^\circ \times 5^\circ$, as explained in

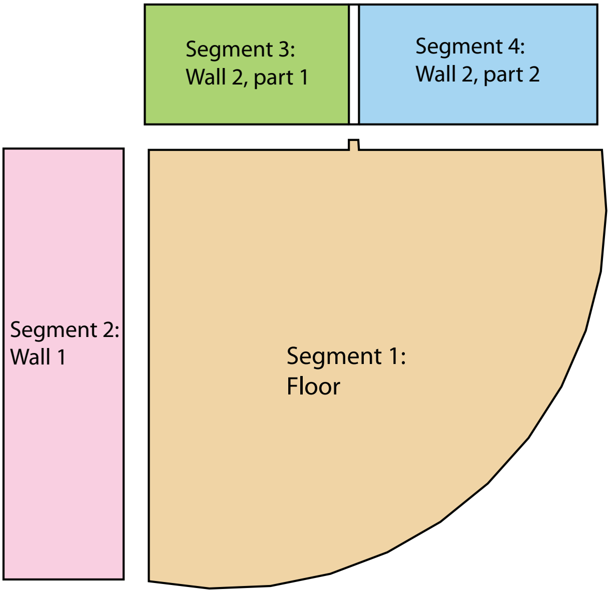

Figure 5.14: *Net-view representation of the standard room segmentation. The room is segmented into four main segments.*

Sec. 5.1.3.2. This subdivision results in patches containing only a small number of points, but enough points to apply a Least Squares estimation of the planar parameters as described in Sec. 3.2.3. In this work, a spherical patch contains approximatively 12 000 points. The spherical patches applied on the segments in the room are depicted in Fig. 5.15. The patch size, varies with respect to the orientation and the distance of the considered surface. Hence, the use of spherical patches enables the local estimation of the deviation to smaller surfaces, which reduces the magnitude of the outliers due to imperfections in the planarity of the floor and the walls.

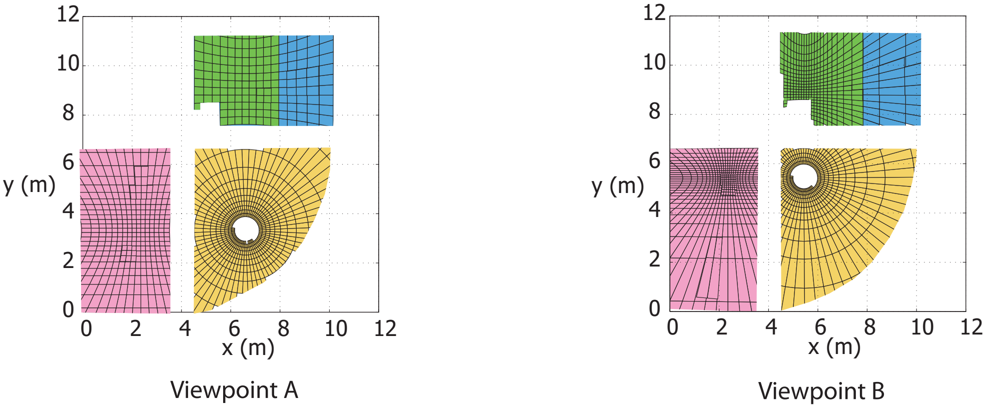

Viewpoint A

Viewpoint B

Figure 5.15: *Net-view of the standard room with spherical patches, using a grid size of* $5^\circ \times 5^\circ$

5.3.2 Isolating the incidence angle effect

In this section, the influence of the incidence angle on the point cloud quality is analyzed for the different positions of the TLS. In this case study, the influence of the range is not incorporated as the variety of ranges in the room is very limited, ranging from 0 m to 6.5 m.

5.3.2.1 Theoretical incidence angle effect

Fig. 5.16 depicts the theoretical incidence angle effect per point on the measurement precision, derived from the estimated planar parameters per segment, as described in Eq. (4.23). Clearly, the position of the laser scanner has an influence on the local incidence angle. Angles plotted in red indicate larger theoretical contribution to the deterioration of the measurement precision. The corner viewpoint results in higher incidence angles towards the far sides of the segments.

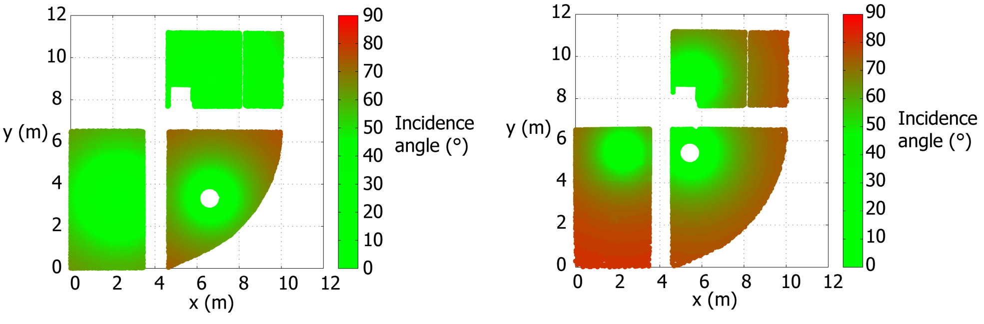

Viewpoint A

Viewpoint B

Figure 5.16: *Net-view of the standard room colored with the theoretical incidence angle effects.*

5.3.2.2 Noise level per segment in practice

For each segment, a regression plane is fitted according to the method described in Sec. 3.2.3. Fig. 5.17 shows the residual $\hat{\mathbf{e}}_\rho$ in the direction of the laser beam, per point in each segment. The points colored in red represent residuals higher than 1 cm. The points on the floor segment (segment 1) that are situated in high incidence angle areas produce high residuals. By moving the scanner from the viewpoint in the corner to the viewpoint in the center, high incidence angles at the bottom right corner of the segment 1 are avoided. In white, the RMSE per segment as computed following Eq. (3.23) is printed in Fig. 5.17. The differences in RMSE between the two viewpoints can partially be explained by comparing the different incidence angle pattern for each segment. In the corner viewpoint (viewpoint B) results, a circular pattern of higher noise levels can be observed in segment 2, corresponding to a surface that is oriented nearly perpendicular to the laser beam. A possible explanation for this effect can be found in the saturation of the detection unit, due to an overload of the intensity sensor of the laser beam. The points measured shortly after the saturation are all affected by a higher residual.

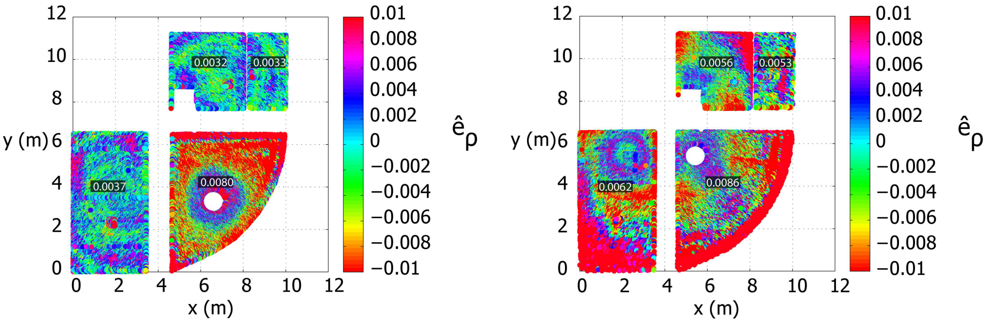

Viewpoint A

Viewpoint B

Figure 5.17: *Net-view of the standard room colored with the the noise level* $\hat{\mathbf{e}}_\rho$ *in the direction of the laser beam. Residuals higher than* 1 *cm are colored in red. (left) Scan captured from viewpoint* A*, in the center of the room, (right) Scan captured from viewpoint* B*, in the corner of the room.*

Fig. 5.18 shows the residual per point $\hat{\mathbf{e}}_\mathbf{d}$ computed according to Eq. (4.20), for each segment. In both viewpoints, the effects of incidence angle on the signal deterioration are removed, leaving a noise level $\hat{\mathbf{e}}_\mathbf{d}$ theoretically independent of the scanning geometry influencing factor, and only dependent on the other influencing factors described in Sec. 2.3.

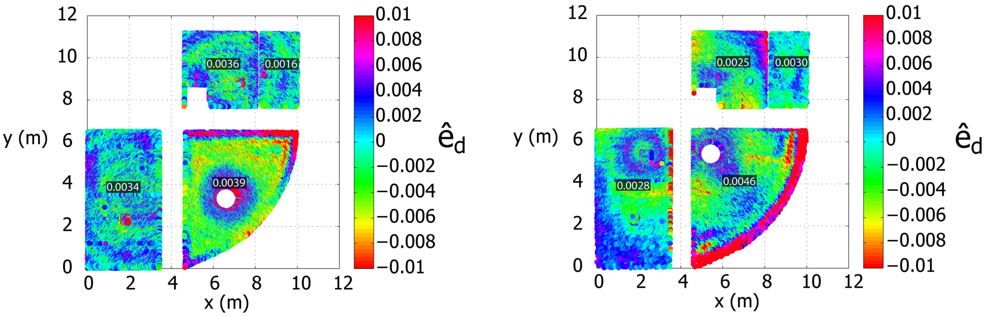

Viewpoint A

Viewpoint B

Figure 5.18: *Net-view of the standard room colored with the the noise level* $\hat{\mathbf{e}}_\mathbf{d}$ *computed according to Eq.* (4.20)*. Residuals higher than* 1 *cm are colored in red. (left) Scan captured from viewpoint* A*, in the center of the room, (right) Scan captured from viewpoint* B*, in the corner of the room.*

In the center viewpoint (viewpoint A), it can be seen that the walls and the floor are not perfectly planar. Segment 2 for instance, shows residuals in the laser beam direction higher than 6 mm despite the local low incidence angle, see Fig. 4.23. After removal of incidence angle effects, these residuals remain higher than 6 mm, see Fig. 5.18. A local planar estimation on a smaller neighborhood enables the analysis of the scanning geometry influence on the signal deterioration, and avoids fitting model errors. In the corner position (viewpoint B), residuals $\hat{\mathbf{e}}_\rho$ obtained for incidence angles higher than 70°

are higher than 1 cm, see Fig. 5.17. Globally, by moving the scanner roughly 2 m to a viewpoint containing higher incidence angles, $\sim 20\%$ of the signal deterioration is due to incidence angles effects.

5.3.2.3 Number of points per Cartesian patch in practice

In Fig. 5.19, the number of points per patch of 20×20 cm is shown for the room used in the experiment. In general, the theoretical number of points is matching the one obtained in the real point cloud. The scanner position at viewpoint B results in a higher total number of points per patch than viewpoint A. For both positions, the point density decreases rapidly with increasing range and incidence angle. As an example, when considering the viewpoint B in Fig. 5.19, the number of points in the patch located at $(6,6)_{(X,Y)}$ is greater than 1500 points, whereas at $(6,6)_{(X,Y)}$ it is less than 10.

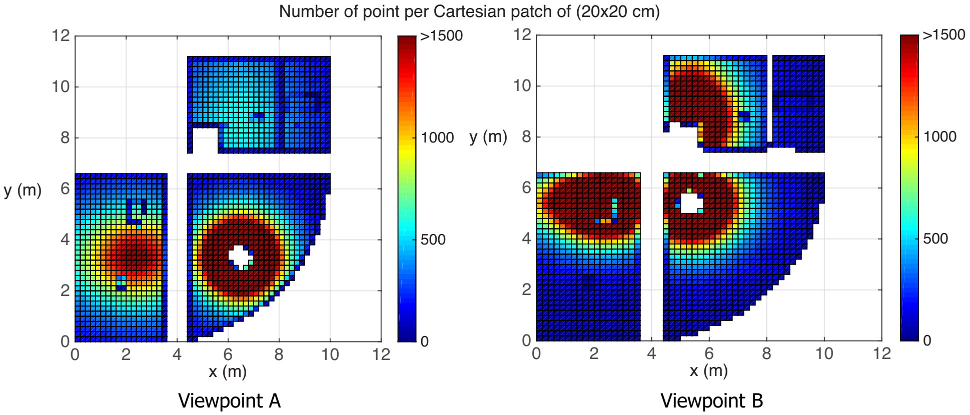

Figure 5.19: *Net-view of the standard room subdivided into Cartesian patches of 20×20 cm colored with the number of points per patch. (left) Scan captured from viewpoint A, in the center of the room, (right) Scan captured from viewpoint B, in the corner of the room.*

5.3.2.4 Noise level per Cartesian patch in practice

From the points in the Cartesian patch, local planar parameters are determined as described in Sec. 3.2.3. For each point in the Cartesian patches in Fig. 5.19 the noise level in the direction of the laser beam is $\hat{\mathbf{e}}_\rho$. The standard deviation $\sigma_{\hat{\mathbf{e}}_\rho}$ of the residuals $\hat{\mathbf{e}}_\rho$ in the direction of the laser beam is computed for each Cartesian patch according to Eq. (4.21). Fig. 5.20 shows the standard deviation $\sigma_{\hat{\mathbf{e}}_\rho}$ for each Cartesian patch, for both viewpoints.

On average, scanning from viewpoint B results in Cartesian patches of better quality. The average patch variance for all patches together equals 0.0023 m for viewpoint A against 0.0017 m for viewpoint B. This shows that by simply moving the scanner by two meters, the quality of the point cloud is in this sense improved by $\sim 25\%$. This is mainly due to the larger amount of small incidence angles patches and smaller amount of patches on the floor with higher noise at viewpoint B.

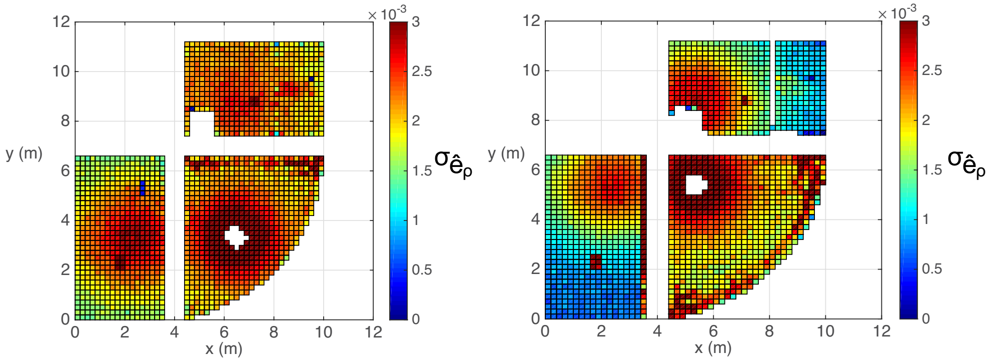

Figure 5.20: *Net-view of the standard room subdivided into Cartesian patches of* 20×20 *cm, colored with the standard deviation* $\sigma_{\hat{\mathbf{e}}_\rho}$ *computed according to Eq.* (4.21)*. (left) Scan captured from viewpoint* A*, in the center of the room, (right) Scan captured from viewpoint* B*, in the corner of the room.*

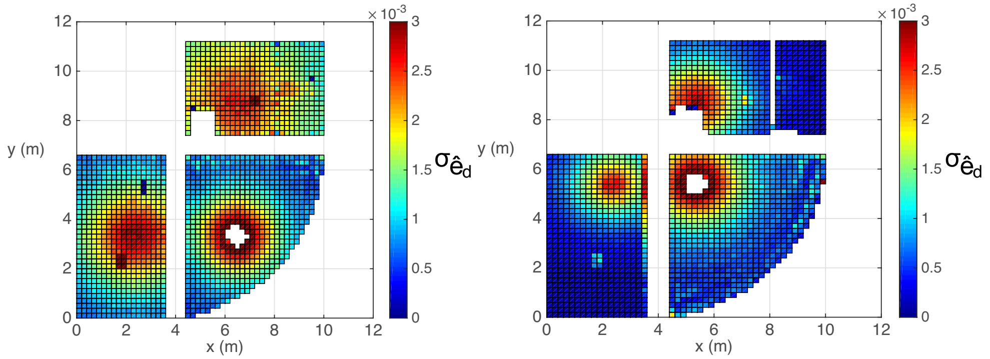

Figure 5.21: *Net-view of the standard room subdivided into Cartesian patches of* 20×20 *cm, colored with the standard deviation* $\sigma_{\hat{\mathbf{e}}_d}$ *computed according to Eq.* (3.14)*. (left) Scan captured from the viewpoint* A*, in the center of the room, (right) Scan captured from the viewpoint* B*, in the corner of the room.*

Fig. 5.21 represents the net view of the room colored with the remaining noise level per scan point $\hat{\mathbf{e}}_d$, after removal of the incidence angle effects according to Eq. (3.14). Clearly this standard deviation depicted in Fig. 5.21 reflects both the individual point quality, compare Fig. 5.17, and the local point density, compare Fig. 5.19. The quality of the Cartesian patches is dominated by the number of points, which biases the comparison of the patches. The Cartesian patches are therefore not really suitable when assessing the quality of local patches of a planar segment with big variations in point density. To avoid the correlation with the number of points per Cartesian patch, we make use of the spherical patches presented in the next paragraph.

5.3.2.5 Noise level per spherical patch in practice

Each segment is subdivided into spherical patches, with a $5^\circ \times 5^\circ$ grid size as depicted in Fig. 5.15. As a consequence, each patch contains 1200 points, unless a patch covers an area with less measurement return or the edge of a segment. For each point in the spherical patches in Fig. 5.15 the noise level in the direction of the laser beam is $\hat{\mathbf{e}}_\rho$. The standard deviation $\sigma_{\hat{\mathbf{e}}_\rho}$ of the residuals $\hat{\mathbf{e}}_\rho$ in the direction of the laser beam is computed for each spherical patch according to Eq. (4.21). Fig. 5.22 shows the standard deviation $\sigma_{\hat{\mathbf{e}}_\rho}$ for each spherical patch, for both viewpoints.

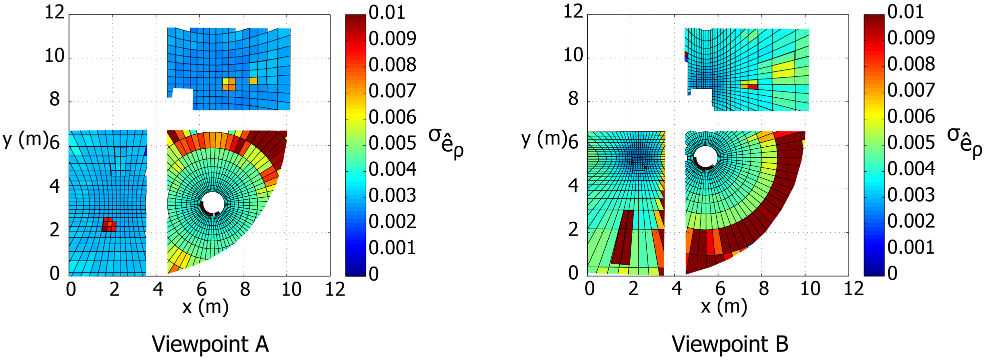

Figure 5.22: *Net-view of the standard room subdivided into spherical patches of* $5^\circ \times 5^\circ$*, colored with the standard deviation* $\sigma_{\hat{\mathbf{e}}_\rho}$ *computed according to Eq.* (4.21)*. (left) Scan captured from viewpoint* A*, in the center of the room, (right) Scan captured from viewpoint* B*, in the corner of the room.*

At lower incidence angles and lower ranges, the point density is higher, which results in a smaller area per patch. The noise contribution due to the incidence angle is clearly visible. Indeed, the patches located at higher incidence angles as seen in Fig. 5.16 are globally less precise than the ones with lower incidence angles. As an example, segment 1, *i.e.* the bottom right segment, is analyzed. By moving the scanner to the corner viewpoint, the far end patches of this segment are less precisely measured due to higher incidence angles. The point density at the far end patches decreases and the area is increasing. By having bigger areas, with less points density, the planar features estimated on these points are less precise. On segment 1, the contribution to the noise level of incidence angles is on average $\sim 22\%$. Moreover, because the surfaces are not perfectly planar, the local imperfections of the surfaces are more apparent on patches with a bigger area. The planarity imperfections of the floor appear very clearly on each viewpoint scan. For example, at the location $(8,6)_{(X,Y)}$, in both viewpoints the patch quality is lower despite a relatively good incidence angle ($\sim 60^\circ$).

By using local patches, the error behaviors of the scan points on the test charts placed in the scene, see Fig. 5.13 are more visible. As studied previously [19], the residuals are dependent on the incidence angle and the surface properties of these test chart.

The average standard deviation of the room is $\sigma_{\hat{\mathbf{e}}_\rho} = 3.23$ mm. Fig. 5.23 represents the net view of the room colored with the remaining noise level per scan point $\hat{\mathbf{e}}_d$, after removal

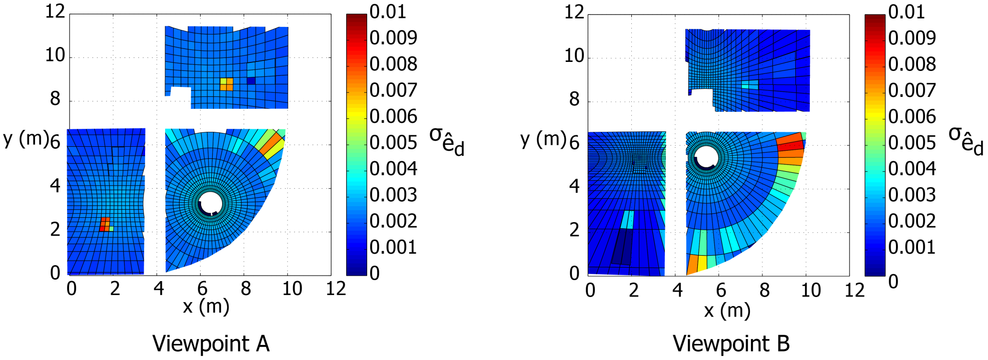

Figure 5.23: *Net-view of the standard room subdivided into spherical patches of* $5^\circ \times 5^\circ$*, colored with the standard deviation* $\sigma_{\hat{\mathbf{e}}_d}$ *computed according to Eq.* (3.14)*. (left) Scan captured from the viewpoint* A*, in the center of the room, (right) Scan captured from the viewpoint* B*, in the corner of the room.*

of the incidence angle effects. The average remaining standard deviation of the room is $\sigma_{\hat{\mathbf{e}}_d} = 2.55$ mm. By averaging the incidence angle contribution per point, it is determined that for this standard room, in both cases approximately $\sim 20\%$ of the measurement noise is caused by non-zero incidence angles. The average of the incidence angle contribution per patch takes into account the point density information.

The proposed approach has been tested on a workstation Dell Precision 390, with 3 Gb of RAM memory, a Dual-Core Intel CPU at 2.13 GHz, and a graphical card NVIDIA Quadro FX3500 256-bit GDDR3. The computations are run under the OS Microsoft Windows 7. The programs are implemented using the software Matlab. The plots are also generated using Matlab.

5.4 Conclusions

This chapter provides an answer to the previously stated research question: How does the scanning geometry affects the total point cloud quality in practice?

The original approach presented in Chapter 4 to express the influence of scanning geometry on the point cloud quality is put in practice and evaluated in this chapter. It is shown how the scanning geometry is extracted from a 3D point cloud in practice. This approach is based on the estimation of local planar features as presented in Chapter 3 applied on both Cartesian and spherical patches. The effects of scanning geometry are quantified and tested on a reference test board and two point cloud sampling of a standard closed room. The practical assessment presented in this chapter shows that the scanning geometry affects the point cloud quality for higher incidence angles and higher ranges from the scanner.

The study of the reference test board shows consistency between the theoretical models derived in Chapter 4 and the noise levels measured at different plate orientations and range placements. The study on the effect of the incidence angles allowed us to show that for a real point cloud of a small room, the contribution of incidence angles to the noise budget decreased by approximately ~ 20% per point when the scanner is moved from one viewpoint located in the middle of the room to another viewpoint with on average more favorable incidence angles. This result is achieved in a small indoor room, where the range effect is not playing an important role. Accordingly, it is shown that it is possible to reduce the total error of the measurements by placing the scanner at another position, which is maybe not the most trivial position one can think of. In this particular case, it is shown that a position at the corner of the small room provides a global better quality point cloud than the one acquired from the middle of the room.

Moreover, the focus of the thesis is set on the scanning geometry effects on the point cloud quality, therefore the surface property effects were not investigated. However, tests performed for this research should ideally be repeated using reference surfaces with known reflectance behavior such as the Spectralon diffuse reflectance targets [79]. From the preliminary studies performed [149] but not shown in this thesis, the surface property effects to also play a role in the quality of the acquisition. As stated previously in Chapter 2, this thesis solely focuses on the effects of scanning geometry on the point quality. All other effects such as surface properties are not presented in this thesis. By being able to isolate the noise component due to scanner geometry, it will also be easier to investigate other noise components. Adequate corrections of these other influencing factors, such as the surface properties, the atmospheric conditions and instrument calibration, will provide future users with measurements of better quality.

Using our approach, an optimization of the measurement set-up can be achieved. An example of such optimization process is presented in Chapter 6. Based on a 2D map of the scene to be scanned, an algorithm is developed that computes possible viewpoints combinations that fulfill a complete coverage of the scene under specific constraints, *e.g.* maximum range, maximum incidence angle, minimum point density. Another application could be a CAD drawing on a first low resolution scan, which enables the characterization of the scanning geometry contribution from the position of the terrestrial laser scanner. Based on the computed incidence angles and ranges, a better positioning of the terrestrial laser scanner according to the scene can be determined where the scanning geometry effects can be minimized. Another application could also be to define a quality standard (say 5 mm), from which the measurement set-up will be derived. This threshold specifies the desired maximum standard deviation achieved from a viewpoint.

Part III

Mitigating scanning geometry negative effects on the quality of a point cloud

CHAPTER

6

Scanner position planning for full scene coverage

> "Give me a place to stand, a lever long enough and a fulcrum. and I can move the Earth"
>
> Archimedes

One of the main applications of the Terrestrial Laser Scanner (TLS) is the visualization, modeling and monitoring of man-made structures like buildings. Especially surveying applications require on one hand a quickly obtainable, high resolution point cloud but also need observations with a guaranteed quality. As shown in Chapter 4 and Chapter 5, the scanning geometry plays an important role in the quality of the resulting point cloud. The ideal set-up for scanning a surface of an object is to position the laser scanner in such a way that the laser beam is near perpendicular to the surface. Due to on-site conditions, such an ideal set-up is in practice often not possible.

In this chapter, the following research question is investigated and answered:

How should a scanning survey be effectively planned?

Several scans taken from different view-points are needed to obtain full coverage of the object surface and to avoid major occlusions. Most scenes contain a large variety of materials and different parts of the scene are scanned with a different scanning geometry from several view-points. The different incidence angles and ranges throughout a scan result in 3D points of varying quality, see Chapter 4. The view-points of the scanner that give the best point-cloud quality are generally not known. This chapter presents a new approach to determine good view-points, but not guaranteed the best view-points.

Despite the large variety of applications, to the best of our knowledge, the topic of TLS placements enabling good quality acquisitions has not been investigated at the time of this research. In this chapter, the different view-points of the laser scanner in a scan project are designed such that the negative impact of scanning geometry on the point quality is mitigated in a particular sense. The design of the measurement setup ensures the complete spatial coverage, while each part of the scene is scanned according to predefined quality requirements. The main quality requirements we use in this thesis are that surfaces are scanned within a maximum incidence angle and range from a given view-point. The complete spatial coverage of the area to be scanned is obtained with a small of number of view-points. The quality of the end point cloud is not investigated in this chapter, as we assume that scanning constraints are sufficient to obtain a good quality point cloud. In the method introduced in this chapter and presented in [145], the impact of the scanning geometry on individual point error is not directly incorporated, only the strict thresholds derived from the scanning geometry studies performed in Chapter 4 and Chapter 5 are used.

6.1 Planning view-points in a scene: available approaches

The determination of the minimum number of view-points needed to cover all edges of a room is known as the set-coverage problem and is a NP-complete problem, a class of notoriously difficult problems [72, 14, 158] (see Sec. 3.2.1). In general, there are no efficient or fast solutions for this class of problems. Therefore, in practice, heuristic methods are used that give an approximation solution.

In this work, we define a view-point as the location of the center of the scanner in the scene. The determination of the positions of view-points that give full coverage of a given scene is investigated in computer science in the Art Gallery problem [26, 108, 50] and the Next Best View problem [73, 123, 14].

In the Art Gallery problem, the complete floor map is assumed to be known on forehand. The positions of the sensors are computed in such a way that all surfaces on the map are covered with a minimum number of sensors. [26] proved that Art Gallery problems have an upper bound on the minimum number of required view-points: there always exists a solution consisting of $[n/3]$ number of view-points that cover all edges of a simple polygon of n vertices. [66] proved that any polygon with n vertices, and h possible holes, can be completely covered by a minimal solution consisting of at most $[(n+h)/3]$ view-points.

In the Next Best View problem, the sensor is first acquiring data from an arbitrary position. Based on this first measurement, the algorithm will incrementally add surfaces to a partial model of the scene and plan the next view-point to acquire such that the visibility is maximal. The process is iterated until the algorithm determines that all possible surfaces have been mapped.

In this chapter, our starting point is a map of a room. In practice, most scenes can be quickly represented as a 2D floor map. One can for instance roughly estimate surroundings and provide a simple "hand drawn" representation of the outer bounds and the possible holes in the scene. Another method could be to quickly scan the scene from arbitrary positions at low resolution and extract the geometry of the scene. From these rough estimations, the optimal scanner view-points are determined using the methodology presented in the following sections. Note that the presented method can be extended from a 2D approach to a 3D approach by considering 3D visibility polyhedra. In this chapter, we only present the 2D approach as it provides a good first insight in the TLS view-point planning.

6.2 A simplified 2D Art Gallery approach

To obtain a problem that is easily solvable by a normal computer, we present in this section some assumptions and simplifications. In a few processing steps, a practical solution is achieved in a small amount of computations.

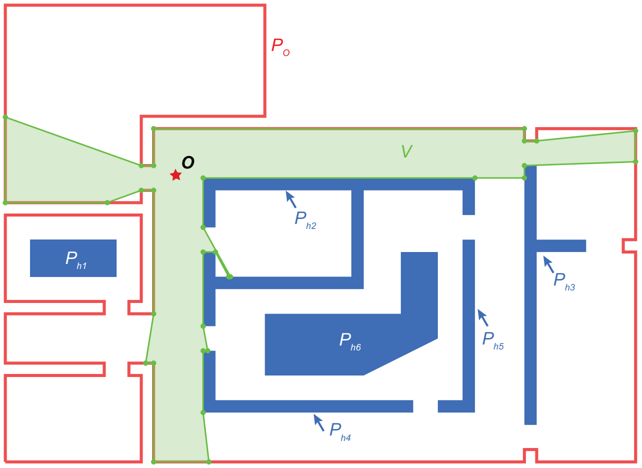

Figure 6.1: *Example of the visibility polygon of a complex room. The outer bound polygon* $\mathbf{P_o}$ *is outlined in red. Interior obstruction polygons* $\mathbf{P_h}_j, j = 1 \cdots 6$ *are represented as blue areas. The interior of these polygons is not visible as they represent wall structure or closed areas. The view-point* O *is depicted as the red star. The visibility polygon* V *from this location* O *is represented as the green area.*

By using notations from [14], the entire scene is defined as the "work space". In this chapter, the work space is defined by using simple polygons, with an "outer bound polygon" that delimits the interior area where the scanner can be placed, and possible "hole polygons" that consists of closed areas within the outer bound polygon where the scanner cannot be placed.

Let the scene be defined as a map $\mathbf{P} = \{\mathbf{P_o}, \mathbf{P_h}\}$ consisting of a simple outer bound polygon $\mathbf{P_o}$ and K possible simple holes polygons $\mathbf{P_h}_j, j = 1 \cdots K$. The scene does not necessarily need to contain hole polygons.

The polygons can be defined as a list of vertices. As defined by [14], a simple polygon is a closed polygonal chain of line segments, also called edges in this chapter, that does not intersect itself. Holes are consisting of non-transparent objects in the scene that can cause interior obstructions, *e.g.* walls, furniture in the room, columns.

To define potential view-point locations, the interior of the room is sampled such that a view-point O is defined inside $\mathbf{P_o}$ and outside all $\mathbf{P_h}$. That is, the outer bound polygon $\mathbf{P_o}$, the K simple holes polygons $\mathbf{P_h}_j, j = 1 \cdots K$ and one arbitrary view-point O fulfill the following relations:

- $\mathbf{P_h}_j \subset \mathbf{P_o} \qquad \forall j$
- $\mathbf{P_h}_i \cap \mathbf{P_h}_j = \varnothing, \qquad i \neq j, \forall i \forall j$
- $O \in \mathbf{P_o} \wedge O \notin \mathbf{P_h}_j \qquad \forall j$

where $\subset$ is the subset operator, $\cap$ is the set intersection operator and $\wedge$ is the logical conjunction operator.

6.2.1 From 3D to 2D view-point positions

Almost all 3D indoors scene can be reduced to a 2D map by taking an horizontal cross section of the scene at for instance the height of the sensor. This approximation of the 3D surroundings by a 2D map results in less intensive computations. As depicted in Fig. 6.1, in this example the horizontal cross-section enables to visualize a floor map of a scene at the height of the scanner, with the outer bound depicted in red and holes depicted in blue. This simplification reduces the complexity of the problem, by considering a 3D scene as a 2D scene at the height of the scanner.

6.2.2 2D Visibility Polygon

The 2D visibility polygon V from a view-point O is a well-known notion [41, 106, 156, 81]. In simple words, the visibility polygon from a view-point is defined as the polygon containing all visible edges, *i.e.* in the direct line of sight of the view-point.

More formally, V is the 2D visibility polygon defined as the set of points p in $\mathbb{R}^2$ that cover all edges of the scene $\mathbf{P}$, such that every point in V is in the direct line-of-sight of the view-point O, is contained inside $\mathbf{P_o}$ and outside $\mathbf{P_h}_j, j = 1 \cdots K$. The view-lines from the view-point O to the points p denoted as $\overline{Op}$ do not intersect any obstacle within the scene $\mathbf{P}$, ergo each $\overline{Op}$ is in the direct line-of-sight of the view-point O. The visibility polygon is therefore defined as follows [41]:

$$V \overset{\text{def}}{=} \max\{p : p \in \mathbf{P_o} \ \wedge \ p \notin \mathbf{P_h}_j \forall j \ \wedge \ \overline{Op} \subset \{\mathbf{P_o} - \mathbf{P_h}_j, j = 1 \cdots K\} \tag{6.1}$$

In Fig. 6.1, the visibility polygon V from view-point O is represented in green.

6.2.3 Discretized possible view-points in a scene

The interior of the room is discretized and gridded with predefined steps of possible scanner locations, as depicted in Fig. 6.7(a). This discretization has the advantage of less computations than when considering continuous locations. However, the grid step size needs to be well defined. A too coarse grid will result in fast computation, but in general in more positions. A too fine grid increases the processing time with no guarantee of having a less locations.

This room is gridded with n possible view-point locations, denoted as $O_i, i = 1 \cdots n$. The grid step is defined such that each edge part is visible from at least one view-point.

6.2.4 Discretized scene

To further simplify the view-point planning, we make use of a discretized scene, where the edges of the polygons $\mathbf{P}$ are reduced to a set of points. In this way, the number of constraints is smaller than when considering continuous surfaces and the computational performance is increased.

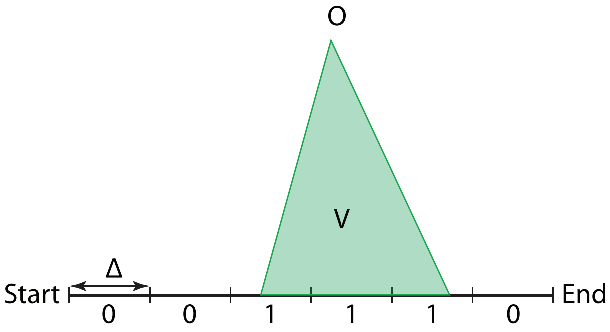

Figure 6.2: *Example of an edge segmentation. The boolean coverage information is given as 1 for visible and 0 as not visible from the view-point O and based on its 2D visibility polygon V. The resolution of the boolean information depends on the edge segmentation interval step Δ.*

Each edge of the scene is discretized into smaller intervals. For instance, an edge m of the outer polygon P_o is discretized into k points, linking smaller segments with interval step Δ following Eq. (6.2):

$$P_o\{m\} = \begin{bmatrix} P_o\{m\}\{1\} \\ \vdots \\ P_o\{m\}\{k\} \end{bmatrix} = \begin{bmatrix} \{x_1, y_1\}, & \{x_2, y_2\} \\ \vdots & \vdots \\ \{x_{k-1}, y_{k-1}\}, & \{x_k, y_k\} \end{bmatrix} \tag{6.2}$$

In Fig. 6.2, the visibility polygon V from the view-point O is depicted as the green area. The edge is divided into smaller segments, which makes it easy keep track of the edge visibility coverage.

The width of the interval step Δ will determine the number of segments k and therefore the resolution of the visibility coverage. Too large segments will result in too simplified approximations of edge coverage, but with faster processing due to a low number of segments. On the contrary, a fine segmentation enables to finely define the boundaries of the visibility coverage at the expense of longer processing time.

6.2.5 Discretized visibility polygons

With the edges of the scene $\mathbf{P}$ subdivided into points connected by small segments, it becomes easy to define the discretized visibility polygon from a view-point O_i using Boolean notation, as depicted in Fig. 6.2. In practice the visibility edges do not perfectly coincide with the small segments boundaries, which results in partially covered segments. In this work, we consider these partially covered segments as visible. As shown in Fig. 6.2, segments that are considered as visible are counted as 1 and the not visible segments as 0. One could also set some thresholds on the amount of visibility coverage per segment, say segments with $> 50\%$ coverage are considered visible, others not visible. We did not set such constraints as we tried to keep the algorithm as simple as possible, and considered any segment as visible as soon as there was some coverage.

In this work, the method described by [41] and implemented by [105] is used to determine the 2D visibility polygon V_i from each possible view-point O_i, as depicted in Fig. 6.1. Only the coverage of the wall surfaces is considered, therefore the polygon edges should all be covered by at least one view-point, while the complete coverage of the interior of the polygon (representing ceiling and floor) is not necessary.

6.3 Optimization problem

6.3.1 Incidence angle and range constraint

The view-points planning algorithms generally assume the sensing instrument to be perfect and with infinite field of view, with valid measurements under any incidence angle and any range constraints. These solutions are very general and unsuitable for the actual TLS capabilities in a real world situation.

It has been shown in Chapter 4 and Chapter 5 that the measurement quality deteriorates with bad scanning geometry, *i.e.* with increasing ranges and increasing incidence angles to the object surface. The incidence angle α is defined as the angle between the laser beam and the normal of the surface. As shown in Chapter 2, a TLS measures distances to surfaces by emitting laser beams, either by continuous modulated signals or single pulses. In both cases, this technology has limitations in the range of measurements, both as a minimum distance d_{min} and a maximum distance d_{max} that can be measured to an object surface. The manufacturer provides the range limitations specific to each laser scanner type, see Sec. 2.2. Moreover, it is shown in Chapter 4 that longer ranges and higher incidence angles result in wider and elongated footprints, which leads to return pulses with decreased signal strength. Therefore, incorporating the scanning geometry limitations in the determination of the visibility polygon provides a realistic representation of the actual measurement capacity of the scanner.

As example of one edge visibility from a view-point O is depicted in Fig. 6.3. This edge is fully visible from the view-point. When adding a maximum incidence angle α_{max} constraint, the edge is only partially visible however, up to the maximum incidence angle α_{max}. The parts of the edges that are observed with incidence angles greater than the maximum threshold α_{max} are considered not visible anymore. The maximum view distance d_{max} from the view-point O is depicted by a red circle. Any edge part that falls outside this circle is considered not visible either.

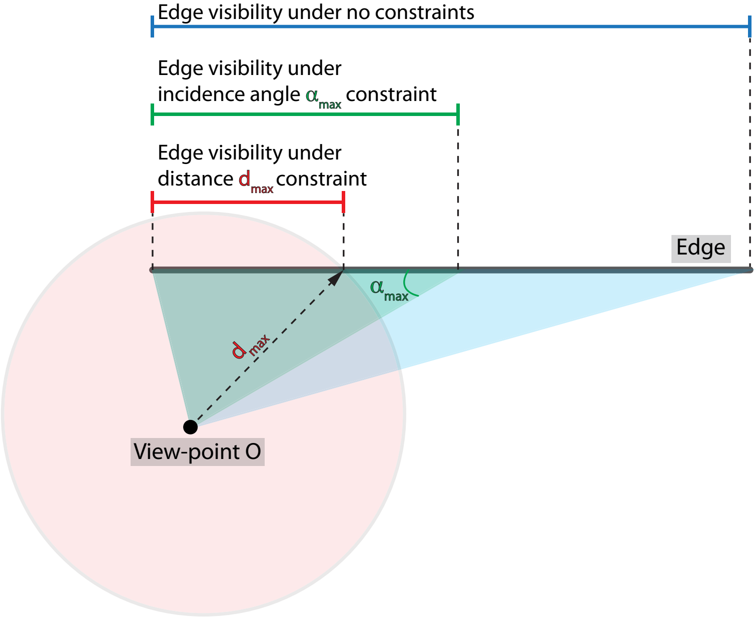

Figure 6.3: *Schematic illustration of the visibility of an edge from a view point O. The visibility of the edge is shown under no constraints, under a maximum incidence angle α_{max} constraint and a maximum distance d_{max} constraint.*

An example of a simple rectangular room is shown in Fig. 6.4. From the view-point O, all edges of this room are visible. The maximum incidence angle constraint α_{max} reduces the visibility of an edge from the view-point O until the maximum incidence angle α_{max}, as shown by the green visible areas in Fig. 6.4. Any edge part with higher incidence angle than α_{max} is considered not visible. The maximum view distance d_{max} from the view-point O is depicted by the red circle. In the same way as for the previous example, any edge part that falls outside this view circle is considered not visible.

By adding the scanning geometry constraints, namely a maximum incidence angle α_{max} and a maximum view distance d_{max}, this simple room example shows that only a few edge parts remain visible from view-point O. These edges fulfill the requirements in terms of low enough incidence angles and distances.

6.3.2 Final view-point localization problem formulation

To significantly reduce the number of scans needed to cover a scene and ensure good quality scans, we propose a view-point localization method based on a 2D map of the area and scanner constraints. This method comprises the following constraints:

- The floor map is a horizontal cross-section obtained at the height of the scanner. This 2D floor map may include holes [Sec. 6.2.1],
- The 2D floor map is discrete [Sec. 6.2.4],
- The possible view-points locations are discrete [Sec. 6.2.3],
- The scanner has range limitations as defined by the manufacturer [Sec. 6.3.1],

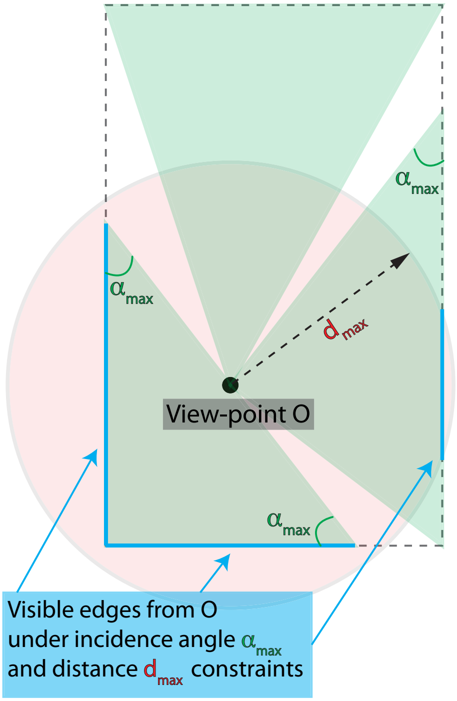

Figure 6.4: *Example of the visibility constraints in a simple rectangular room. The edges of the room are depicted as dashed lines. From the view-point* O*, all edges of this room are visible under no constraints. The visibility polygons from the view-point* O *under a maximum incidence angle constraint* α_{max} *are depicted in green. The maximum distance constraint* d_{max} *is depicted as the red circle. When considering both incidence angle and distance constraints, the visible edges from the view-point* O *are depicted as blue lines.*

- The incidence angles measured on surfaces should not exceed a defined threshold [Sec. 6.3.1].

We present a view-point localization method under the above mentioned constraints. The following cases are studied:
1− All edges of the 2D floor map are covered by at least one view-point.
2− All edges are scanned from at least one view-point with incidence angles below a maximum incidence angle α_{max}.
3− All edges are covered from at least one view-point with at least a minimum distance d_{min} and with a maximum distance d_{max} to the scanner.
4− All edges are scanned from at least one view-point with at least a minimum distance d_{min} and with a maximum distance d_{max} to the scanner and incidence angles below a maximum incidence angle α_{max}.

6.3.3 Optimization problem statement

By modeling this optimization as a discrete combinatorial problem, an approximate solution is obtained. An optimal solution to this optimization problem would be the smallest set of view-point locations $\{o_j \in O_i\}_{(j \leq i)}$ needed to cover all edges of the scene $\mathbf{P}$, given different visibility constraints as defined in Sec. 6.3.2.

The simplified model of the objective function and constraint described by [41] uses the following Integer Linear Programming[1] formulation:

$$\begin{aligned} & z = \min \sum_{j \in \mathbf{P}} o_j \\ \text{subject to:} \quad & \sum_{\substack{j \in \mathbf{P} \\ p_i \in V_j}} a_{ji} o_j \geqslant 1, \forall p_i \in \mathbf{P} \\ & o_j \in \{0,1\}, \forall j \in \mathbf{P} \end{aligned} \tag{6.3}$$

where

$$a_{ji} = \begin{cases} 1, & \text{if } p_i \in V_j \\ 0, & \text{otherwise} \end{cases}$$

$$o_j = \begin{cases} 1, & \text{if } j \text{ belongs to the solution} \\ 0, & \text{otherwise} \end{cases}$$

A view-point o_j is considered to belong to the solution if it fulfills the constraints stated in Sec. 6.2. If the view-point o_j is belonging to the solution, it is given the value 1, else it is given the value 0. From that view-point o_j, the points a_{ji} of the discretized scene $\mathbf{P}$ are given the value 1 for all points p_i that belong to the visibility polygon $V_j = V\left(o_j\right)$. All other points a_{ji} that do not belong to the visibility polygon V_j are considered not visible from o_j and therefore are given the value 0. The visibility polygon is defined based on one of the four visibility constraints defined in Sec. 6.3.2.

The solution set to this optimization problem is given as $Z = \{j \in \mathbf{P} | x_j = 1\}$. The objective function minimizes the cardinality z of the solution set Z [31, 138].

6.4 TLS placement algorithm: Greedy approach

The Boolean coverage information per view-point is used in a Greedy algorithm to determine a minimum number of view-points necessary to cover all the edges of the room, as implemented by [54].

By using a Greedy approach [27], a set-coverage algorithm is obtained in a simple manner that involves few computation steps. The complexity of the Greedy approach has an asymptotic bound of $O(n)$). The Greedy algorithm as shown in Algorithm 3 produces a fast and good non-unique solution, often near the optimal solution [144]. At each iteration, the algorithm choses for the local best view-point, in the sense that the chosen view-point covers the most local uncovered surfaces from the available discrete view-points. In this chapter, we consider a solution to be good if the chosen set of points covers the entire scene, with a small number of view-points. The Greedy approach provides a set of

---

[1] The mathematical optimization program is expressed with variables that are restricted to be integers. The objective function and the constraints are linear. [138]

view-points close to the minimum number of view-points of $\left\lfloor \frac{n+h}{3} \right\rfloor$ [66] required for a complete coverage of the scene [144].

With this approach, the set of view-points cannot be guaranteed to be the minimal number of points achievable. A better solution could be found that could consist of less points by using a different optimization technique, most likely at a cost of more computations and a more complex implementation, without any guarantee that the solution set is greatly improved. However, different optimization techniques are not presented in this work, and are not compared to the presented Greedy approach. This chapter presents one simple method that enables a quick survey plan. In addition, with the approach presented in this chapter, solutions can be found that have the same coverage properties.

For the n possible view-points $O_i, i = 1 \cdots n$, let $V_i, i = 1 \cdots n$ be the n visibility polygons computed following the explanation in Sec. 6.2.2. Each visibility polygon is discretized and snapped to the smaller edge segments of the room $\mathbf{P}$ [105].

Algorithm 3: Greedy Algorithm

```
input  : $O_i, i = 1 \cdots n$, $\mathbf{P}$
output : set of view-points $o_j,, i = 1 \cdots m, m \le n$
initialisation;
$O_{\text{temp}} \leftarrow O$;
$\mathbf{P}_{\text{temp}} \leftarrow \mathbf{P}$;
while $\mathbf{P}_{\text{temp}}$ is not empty do
    index ← Max(Visibility($O_{\text{temp}}$)) ;
    Add($O_{\text{temp}}$[index] to set $o_j$) ;
    Remove($O_{\text{temp}}$[index] from set $O_{\text{temp}}$);
    Remove(edges covered by Visibility($O_{\text{temp}}$[index]) from $\mathbf{P}_{\text{temp}}$)
end
```

The algorithm starts by initializing temporary variables. The temporary variable $\mathbf{P}_{\text{temp}}$ is initialized with all edges of the scene $\mathbf{P}$. The temporary variable O_{temp} is initialized with all n possible view-points $O_i, i = 1 \cdots n$. At each iteration step, the view-point in O_{temp} that covers the most number of uncovered edges in $\mathbf{P}_{\text{temp}}$ is added to the set of view-points o_j. This view-point is obtained by assessing the visibility from all available possible view-points. This selected view-point is then removed from the list of view-points O_{temp}. The respective edges covered by that view-point are also removed from the edge list $\mathbf{P}_{\text{temp}}$. This process is iterated until the temporary variable $\mathbf{P}_{\text{temp}}$ is empty. At the end of the process, the selected set of m view-points $o_j, j = 1 \cdots m$ ensures a complete coverage of all edges in the scene $\mathbf{P}$.

To illustrate the mechanism of the Greedy algorithm, we present a simple example as shown in Fig. 6.5. This simple room consists of 12 edges, without any obstacles inside. As described in Sec. 6.2.4, long edges are divided into smaller segments, so that the entire room is in this case represented by 22 segments. Inside this room, 14 different possible view-points are considered.

First, a table of segment coverage per view-point O is derived, following the method in Sec. 6.2.2, as shown in Table 6.1. Segments that are visible from that view-point are marked 1, and the ones not visible are marked 0.

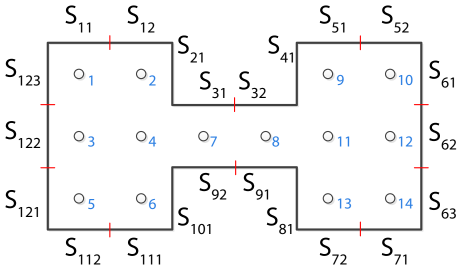

Figure 6.5: *Simple Greedy algorithm example. Room consisting of* 12 *edges, divided into* 22 *segments.* 14 *different view-points are considered.*

O S	1	2	3	4	5	6	7	8	9	10	11	12	13	14
S_{11}	1	1	1	1	1	1	1	0	0	0	0	0	0	0
S_{12}	1	1	1	1	1	1	0	0	0	0	0	0	0	0
S_{21}	1	1	1	1	1	1	0	0	0	0	0	0	0	0
S_{31}	0	0	1	1	1	1	1	1	0	0	1	1	0	1
S_{32}	0	0	1	1	1	0	1	1	0	0	1	1	1	1
S_{41}	0	0	0	0	0	0	0	0	1	1	1	1	1	1
S_{51}	0	0	0	0	0	0	0	0	1	1	1	1	1	1
S_{52}	0	0	0	0	0	0	0	1	1	1	1	1	1	1
S_{61}	0	0	0	1	1	0	1	1	1	1	1	1	1	1
S_{62}	0	0	1	1	0	0	1	1	1	1	1	1	1	1
S_{63}	1	0	0	1	0	0	1	1	1	1	1	1	1	1
S_{71}	0	0	0	0	0	0	0	1	1	1	1	1	1	1
S_{72}	0	0	0	0	0	0	0	0	1	1	1	1	1	1
S_{81}	0	0	0	0	0	0	0	0	1	1	1	1	1	1
S_{91}	1	0	1	1	0	0	1	1	1	1	1	1	0	0
S_{92}	1	1	1	1	0	0	1	1	0	1	1	1	0	0
S_{101}	1	1	1	1	1	1	0	0	0	0	0	0	0	0
S_{111}	1	1	1	1	1	1	0	0	0	0	0	0	0	0
S_{112}	1	1	1	1	1	1	1	0	0	0	0	0	0	0
S_{121}	1	1	1	1	1	1	1	1	0	1	1	0	0	0
S_{122}	1	1	1	1	1	1	1	1	0	0	1	1	0	0
S_{123}	1	1	1	1	1	1	1	1	0	0	1	0	0	1
Score	**12**	**10**	**14**	**16**	**12**	**10**	**12**	**12**	**10**	**12**	**16**	**14**	**10**	**12**

Table 6.1: *Score table of segment (S) visibility per view-point (O) following the example shown in Fig. 6.5*

Table 6.1 provides an overview of the segments visible from each view-point $O_i, i = 1 \cdots 14$. The Greedy algorithm used in this work first selects the view-points that have the highest score in terms of coverage. In this case, two candidates have highest score: O_4 and O_{11}. The algorithm simply takes the first option with a highest score, in this case O_4. At the next iteration, the algorithm considers the scores of coverage per view-point for the remaining segments to be covered. That is, from the updated score table the segments

O S	1	2	3	4	5	6	7	8	9	10	11	12	13	14
S_{11}	1	1	1	1	1	1	1	0	0	0	0	0	0	0
S_{12}	1	1	1	1	1	1	0	0	0	0	0	0	0	0
S_{21}	1	1	1	1	1	1	0	0	0	0	0	0	0	0
S_{31}	0	0	1	1	1	1	1	1	0	0	1	1	0	1
S_{32}	0	0	1	1	1	0	1	1	0	0	1	1	1	1
S_{41}	0	0	0	0	0	0	0	0	1	1	1	1	1	1
S_{51}	0	0	0	0	0	0	0	0	1	1	1	1	1	1
S_{52}	0	0	0	0	0	0	0	1	1	1	1	1	1	1
S_{61}	0	0	0	1	1	0	1	1	1	1	1	1	1	1
S_{62}	0	0	1	1	0	0	1	1	1	1	1	1	1	1
S_{63}	1	0	0	1	0	0	1	1	1	1	1	1	1	1
S_{71}	0	0	0	0	0	0	0	1	1	1	1	1	1	1
S_{72}	0	0	0	0	0	0	0	0	1	1	1	1	1	1
S_{81}	0	0	0	0	0	0	0	0	1	1	1	1	1	1
S_{91}	1	0	1	1	0	0	1	1	1	1	1	1	0	0
S_{92}	1	1	1	1	0	0	1	1	0	1	1	1	0	0
S_{101}	1	1	1	1	1	1	0	0	0	0	0	0	0	0
S_{111}	1	1	1	1	1	1	0	0	0	0	0	0	0	0
S_{112}	1	1	1	1	1	1	1	0	0	0	0	0	0	0
S_{121}	1	1	1	1	1	1	1	1	0	1	1	0	0	0
S_{122}	1	1	1	1	1	1	1	1	0	0	1	1	0	0
S_{123}	1	1	1	1	1	1	1	1	0	0	1	0	0	1
Score	**0**	**0**	**0**	**0**	**0**	**0**	**0**	**2**	**6**	**6**	**6**	**6**	**6**	**6**

Table 6.2: *Score table of segment (S) visibility per view-point (O) following the example shown in Fig. 6.5 after discarding the first view-point candidate O_4.*

already covered by O_4 are not counting anymore in the score table, as shown in Table 6.2.

Again, the Greedy algorithm selects the view-point candidates that have the highest coverage score for the remaining segments that are not yet covered. In this case view-points O_9, O_{10}, O_{11}, O_{12}, O_{13} and O_{14} all have the highest coverage score. The Greedy algorithm selects the first option out of these candidates, which in this case is O_9. The visibility score table is updated as previously. In this simple scenario, only one iteration was necessary to solve the coverage of the example room in Fig. 6.5. The set of view-points that ensure full coverage as selected by the Greedy algorithm in this example are O_4 and O_9.

Note that by adding constraints on the visibility from a view-point, the coverage of edges per view-point may change. Some edges that are considered visible without constraints, or 1 in the score table, might not be visible under different constraints and become 0 in the score table. The Greedy algorithm selects optimal view-points based on the amount of edges that are covered from that view-point.

6.5 View-point localization in practice

The method proposed in this chapter is to be used in the planning phase of a survey project, as shown in Fig. 6.6. It enables the theoretical determination of view-point positions to cover fully a scene. The planning phase of TLS survey projects is often neglected, and can lead to a lack of or too many measurements performed to properly cover the area of interest. It is crucial to plan beforehand the view-points position before going on site. A lack of measurements would imply another survey planning on the same site to complete the set of scans with the not covered areas. Too many scans would imply that the survey could have taken less time in acquisition, but also the post-processing could be less intense, *e.g.* less registration of scans, smaller data to handle.

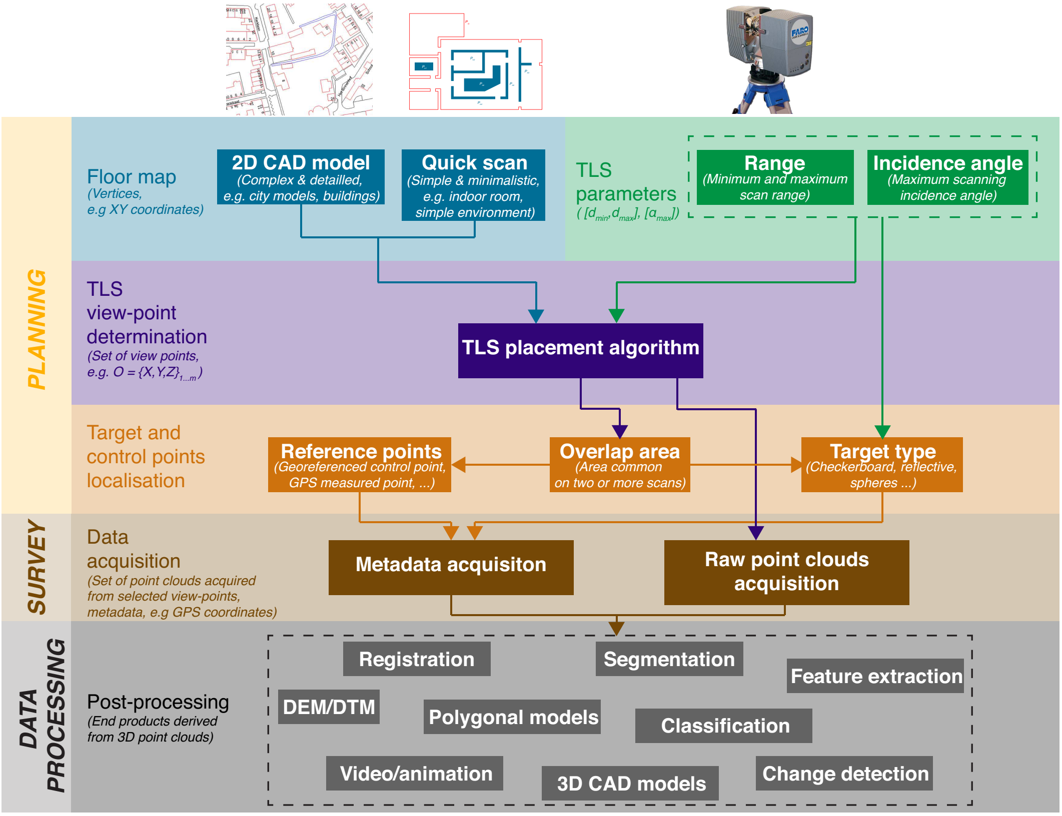

Figure 6.6: *TLS good practice of survey planning*

This method should be used to first get an indication on the number of view-points needed to cover the full scene based on the instrument constraints. Usually, the user needs to rent a TLS to perform measurements. Depending on the TLS in use, the number of scans needed to cover a scene varies, as it depends on the maximum measurable distance. Thanks to this method, the user can vary the different geometrical constraints and assess which TLS suits best his needs. By knowing in advance the expected number of view-points needed, the user can plan ahead the survey in time and space, which is cost effective.

Algorithm 4: TLS Placement Algorithm

```
input  : Outer bound polygon $\mathbf{P_o}$ and possible holes $\mathbf{P_h}$
output : set of view-points $o_j,, i = 1 \cdots m, m \leq n$ with their visibility polygons

initialisation;
Definition of scene edge discretization width;
Definition of scene view-point step discretization width;
Definition of minimum and maximum scanning ranges $d_{min}$ and $d_{max}$;
Definition of incidence angle $\alpha_{max}$;
computation;
$\mathbf{P} \leftarrow$ Scene edge discretization;
$O_i, i = 1 \cdots n \leftarrow$ Scene possible view-point gridding;
$o_j,, i = 1 \cdots m, m \leq n$ Greedy($O_i$, $P$, $d_{min}$, $d_{max}$, $\alpha_{max}$);
```

The presented method is put in practice following Algorithm 4. The floor map is either derived from the actual CAD drawing of the scene, or from a quick scan of the scene that provides the main features to be scanned. In the described method, the floor map is defined as a list of vertices as 2D xy coordinate points. The user needs to define the scene edge discretization width and the view-point step discretization width. These two parameters define the resolution of the solution set, as discussed in Sec. 6.2.4 and Sec. 6.2.3. From our practical assessments, it is advised to sample the possible view-points up to a grid size of approximately half a meter. A too fine discretization of the possible view-points in the scene leads to more difficulties for the user to determine the view-points in the actual scene. When using a roughly estimated map, it is obviously not useful to try to position exactly the TLS to the view-point obtained from our method. A rough estimate around the view-point is sufficient.

Based on the TLS in use and specific requirements of a project, the user defines the desired minimum and maximum scanning ranges d_{min} and d_{max} as well as the maximum incidence angle α_{max}. For each possible view-point in the scene $O_i, i = 1 \cdots n$, a visibility polygon is computed based on these scanning geometry constraints.

The Greedy algorithm as presented in Algorithm 3 selects a set of view-points $o_j,, i = 1 \cdots m, m \leq n$ from the n possible view points $O_i, i = 1 \cdots n$ that ensures a complete coverage of all discretized edges in the scene $\mathbf{P}$. As the floor map is assumed to be on forehand known, the user can easily determine these view-point positions in the real scene by means of *e.g.* a laser distance meter (*e.g.* [86]) or a simple measuring tape. For each of these view-points, the user can also visualize and check the visibility of the scene from the view-point.

6.6 View-point determination results

6.6.1 Measurement set-up

To illustrate the method, two simulated case studies are presented. In both cases, a buffer of $d_{min} = 1$ m is applied around all edges of the room to prevent positions too close to the surfaces. The interval step used for the segmentation of the edges is $\Delta = 0.05$ m. These test cases are assuming that the scans will be acquired by a mid-range phase based terrestrial scanner, which often has a maximum range limitation of $d_{max} = 80$ m. Following Chapter 4 and Chapter 5, the maximum incidence angle on surfaces is set to $\alpha_{max} = 70°$. Both case studies presented in this chapter represent indoor areas that are in real life not often encountered as the presented scales are not realistic. These dimensions were however chosen to depict extreme cases where both incidence angles and ranges were playing an important role in the determination of the number of view-points and their locations.

The first scene is a simple squared room of 400×400 m, as depicted in Fig. 6.7. The room is sampled with 361 possible view-points spaced every 20 m on a regular XY Cartesian grid. This simple test case is chosen to illustrate the impact of the scanning geometry constraints on the definition of the view-points locations.

The second scene is a more complex room of 520×380 m, with multiple rooms and occlusions on walls, as depicted in Fig. 6.8. 356 possible view-points are chosen on a regular Cartesian grid. The effects of occlusions is demonstrated in this test case.

6.6.2 Results and discussions

6.6.2.1 View-points without constraints

By considering only the line of sight of the scanner, the simple room can be completely covered by one view-point, as depicted in Fig. 6.7(a). This simple room is a convex polygon, therefore no occlusions from the edges can occur. Any of the possible 361 view-points will enable the complete coverage of the simple room.

The complex room is concave, meaning that some edges of its bounding polygon can occlude areas in the polygon depending on the view-point. As depicted in Fig. 6.8(a), multiple view-points are required to obtain a complete coverage of the scene. In this particular case, five view-points placed in the different opened rooms cover all the edges of the scene.

6.6.2.2 View-points under incidence angle constraints

Applying the incidence angle constraint on the visibility polygons of a view-point reduces the field of view of the scanner with respect to the surface orientations. As shown in Fig. 6.7(b), the simple room can still be fully seen from one view-point, under the incidence angle constraint of $\alpha_{max} = 70°$. This constraint does not change the number of view-points, it however provides a better position of the scanner from which incidence angles on surfaces are tolerable. As the complex room contains more edges with different orientations, the number of view-points required to cover all the edges with an incidence angle smaller than α_{max} doubles to ten view-points, as seen in Fig. 6.8(b).

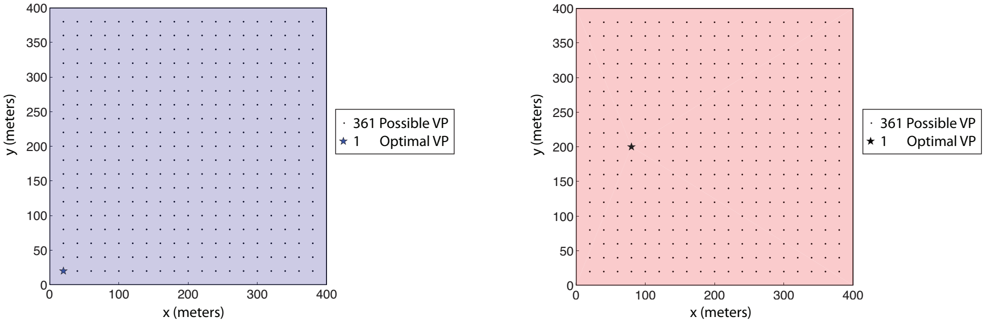

(a) In this case, only one view-point is needed. Any of the possible 361 view-points fulfill the visibility constraint. The visibility polygon is represented as the blue area.

(b) One view-point is required to cover all the edges under incidence angles constraints. Multiple view-points can fulfill the visibility under incidence angle constraints. The visibility polygon is represented as the red area.

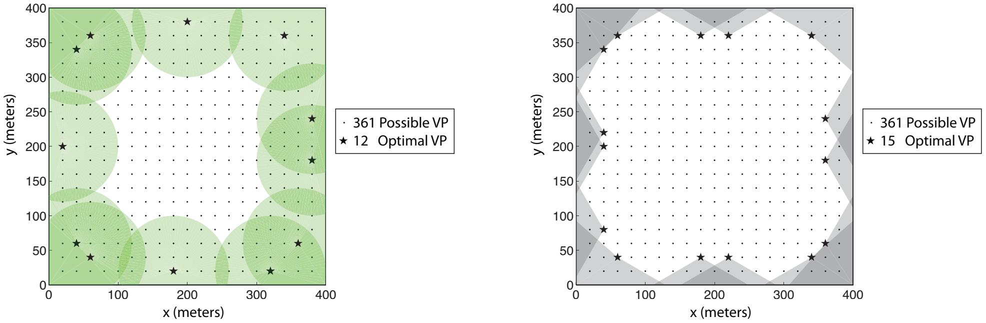

(c) At least twelve view-points are required to cover all the edges under range constraints. The visibility polygons are represented as the green areas.

(d) At least fifteen view-points are required to cover all the edges under range and incidence angles constraints. The visibility polygons are represented as the gray areas.

Figure 6.7: *Visibility coverage of simple room.* 361 *view-points are used in the scene, depicted as black dots. Possible view-points that fulfill the visibility constraints are depicted as stars, with their visibility coverage area. The darker the visibility area, the more view-points coverage.*

6.6.2.3 View-points under range constraints

The range constraints of $d_{min} = 1$ m and $d_{max} = 80$ m enforce a realistic representation of the measurement capabilities of a terrestrial laser scanner. The coverage of all edges of large rooms under range constraints results in the increase of the number of view-points necessary to cover the scene. In the simple room case, twelve view-points are needed, as shown in Fig. 6.7(c). As opposed to the visibility coverage without any constraints, many view-points are required to cover a complete single edge of a scene. Fig. 6.8(c) shows that the complex room is covered by seventeen view-points under range constraints.

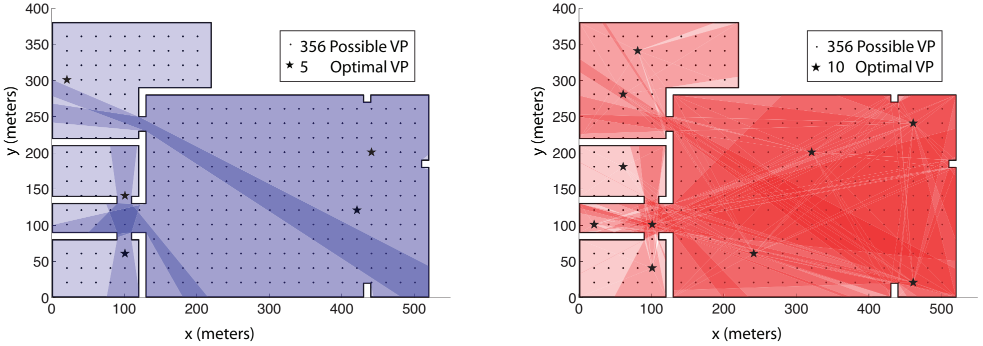

(a) At least five view-points are required to cover all the edges. The visibility polygons are represented as the blue areas.

(b) At least ten view-points are required to cover all the edges under incidence angles constraints. The visibility polygons are represented as the red areas.

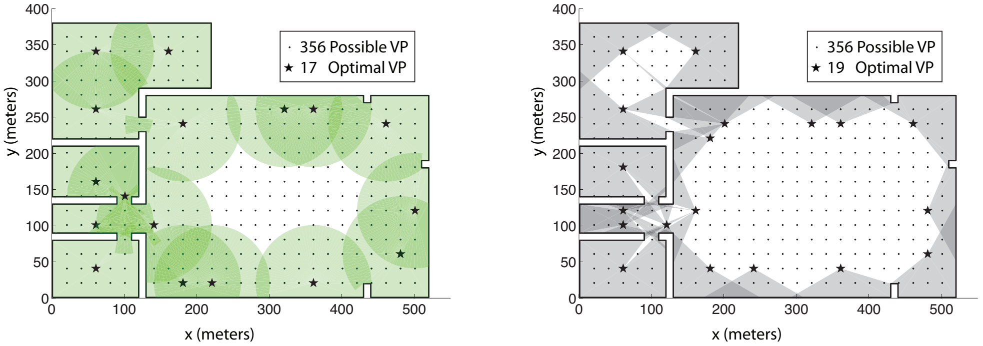

(c) At least seventeen view-points are required to cover all the edges under range constraints. The visibility polygons are represented as the green areas.

(d) At least nineteen view-points are required to cover all the edges under range and incidence angles constraints. The visibility polygons are represented as the gray areas.

Figure 6.8: *Visibility coverage of a complex room.* 356 *view-points are used in the scene, depicted as black dots. Possible locations of the scanner that fulfil the visibility constraints are depicted as stars, with their visibility coverage area. The darker the visibility area, the more view-points coverage.*

6.6.2.4 View-points under incidence angle and range constraints

By incorporating both the maximum incidence angle α_{max} and the range constraints d_{min} and d_{max}, the view-points necessary to cover a large room can be defined. These view-points ensure low incidence angles and ranges to the surfaces that are within the specifications of the instrument. The effects of bad scanning geometry are avoided, resulting in more reliable point clouds. As depicted in Fig. 6.7(d), fifteen view-points are necessary to cover the simple squared room. Nineteen view-points are required to cover the complex room under the range and incidence angle constraints, as seen in Fig. 6.8(d).

6.7 Conclusions and future work

In this chapter, the following research question was investigated and answered: How should a scanning survey be effectively planned?

An original method is presented in this chapter to determine a set of few but sufficient view-points in a scene based on terrestrial laser scanner capabilities. It is shown that the positions of the view-points can be on forehand determined to capture scans of the surroundings with good quality. As a first demonstration to show how to incorporate measurement geometry, it is shown how to incorporate both a maximum range and a maximum incidence angle constraints. This method is fast and only requires a rough 2D floor map of the scene as input.

The influence of this incidence angle constraint and of a range limitation is shown on two simulated rooms. The presented work uses a simple 2D Cartesian gridding of the room to determine possible view-point locations. An adaptive grid to the level of detail required per surface would improve the determination of the best view-points. Moreover, a finer grid would avoid view-points positions too close to each other, however it will be at the expense of longer processing times.

The presented method handles the incidence constraint and the range constraints as two thresholds. These constraints can also be used as a weighting factor. Indeed, as shown in Chapter 5, from two different view-points all edges of a scene can be equally visible, however the influence of the scanning geometry on individual points can be different. By incorporating the impact on error of the scanning geometry per considered view-point in the decision process, the Greedy algorithm will result in view-points providing good quality point clouds with an optimal scanning geometry.

Currently, the presented method uses a 2D discretized map of the scene at the height of the laser scanner. A possible extension of this method would be to consider the 3D room and define the 3D visibility from a view-point. The integration of several realistic scanner heights would improve the determination of the optimal view-points.

Finally, in this work, we used a Greedy approach to select the near optimal view-points necessary to cover the scene. It currently provides a good solution, but not necessarily the optimal one. An exact optimization algorithm would in some cases provide better view-points, often at the cost of a more complex and time/memory consuming program.

Part IV

Critical assessment and future work

Chapter 7

Conclusions and recommendations

> *"There is no real ending. It's just the place where you stop the story."*
>
> Frank Herbert

This concluding chapter summarizes the results presented in this thesis to address the research question stated in Chapter 1. An answer to each subquestion derived in Chapter 1 is provided. Recommendations and possible future works following the methodology presented this work are provided at the end of this chapter.

7.1 Summary of results

As stated in Chapter 1, the main research question investigated in this thesis is:

> How to incorporate measurement geometry in scanning protocols to achieve final products of a well-described good quality?

To answer this question, five subquestions were presented in Chapter 1, which helped answering in detail this main question. In short, this main research question is answered as follows: this dissertation presented an original method that quantifies the effects of scanning geometry on the individual point quality. Here, scanning geometry is defined as the combination of measurement range and incidence angle. The quality of individual points in a point cloud is described based on their noise level, which is extracted in practice using local planar features. The developed models are put in practice in survey planning, where scanning view-points can be localized beforehand to capture scans of the surroundings with good quality. in the following sections, the five subquestions introduced in Chapter 1 are answered in more detail.

7.1.1 What major factors influence the quality of an individual point in a point cloud?

Chapter 2 presented an overview of the principles of laser scanning and the state of the art. Chapter 2 answers this subquestion by presenting a detailed overview of factors that affect the quality of a point cloud. In this thesis, it is shown that the quality of individual points in a point cloud is influenced by four main factors: the instrument limitations, the atmospheric conditions, the object properties and the scanning geometry. The three first factors of these four main factors were discussed in detail this chapter. In real-life, the end-user often has a limited control and influence on these three factors. It is difficult to modify parameters such as mirror rotation, foggy weather or wall material to comply with better scanning conditions. The last influencing factor is the scanning geometry, on which the end-user has a strong influence as the position of the laser scanner in the scene is determined by the user. It is presented in detail in Chapter 4.

7.1.2 How can the quality of an individual point in a point cloud be assessed?

Chapter 3 answers this question by presenting a point cloud quality assessment based on local planar features extraction. The quality investigated in this thesis relates to the random errors or precision of individual points and do not deal with systematic errors or biases. The point cloud is first divided into smaller areas called patches, where it can be assumed that locally, such area is planar. A local plane is fitted to the patch points and the local noise level is estimated. The planar fitting methods considered in this thesis enabled to process huge amounts of data (few million points) with a reasonable time / memory consumption. In Chapter 3, three different planar fitting methods are presented and compared, namely a Ordinary Least Squares method, a Total Least Squares method and a Principal Component Analysis method. The quality of each local fit is described using standard deviation derived from Least Square Estimation. The main quality describers used in this work are presented in Chapter 3 and further put in practice in Chapter 5. It has been shown that the Ordinary Least Squares method is fast and provides a good quality analysis of the planar features. However, this method is dependent on the orientation of the plane. The second method described is the Total Least Squares method, which computes the planar features in a very accurate way regardless of the orientation of the plane. It is however a slow method and requires a lot of memory. A good trade-off method presented in this chapter is the Principal Component Analysis, which is fast and independent on the plane orientation. The quality description achieved by the latter is not as straightforward as the two previous methods.

7.1.3 What is scanning geometry and how does it affect the individual point quality?

Chapter 4 answers this question by defining the scanning geometry by using two parameters: the incidence angle and the range. The incidence angle is defined as the angle between one laser beam vector and the normal vector to the surface. The range is defined as the distance between the scanner and the surface. In this chapter, it is shown that the incidence angle and the range affect the individual point signal to noise ratio. The received signal magnitude of the measurements decreases with increasing incidence angle and range. The received signal magnitude influences the precision of the distance determination. It is shown that the shape of the footprint of the laser light on a surface depends on those two parameters. It is also shown that by considering the influence of scanning geometry on the signal to noise ratio, the increase in measurement noise with increasing incidence angle and increasing ranges is successfully modeled. The presented approach allows the quantification of the contribution of noise induced by the scanning geometry, based solely on point cloud data. No additional or external measurements are needed. The contribution of the two scanning geometry parameters on the point quality has been quantified using contribution coefficients.

The effect of the incidence angle on the range measurement is expressed as a coefficient $c_I(\alpha)$ of values ranging from 1 to 0 for incidence angles α ranging from $0°$ to $90°$, as defined in:

$$c_I(\alpha) = \cos\alpha = \cos\phi(a\cos\theta + b\sin\theta) + c\sin\phi \tag{7.1}$$

The received amount of power decreases with increasing scan range, *i.e.* the effect of the range to the total noise level is proportional to the square of the range. Assuming that ρ_{min} is the minimum range for which the backscattered signal can be detected, and ρ_{max} is the maximum range measurable without ambiguity, the contribution of the range on the measurement deterioration is modeled by a coefficient $c_R(\rho)$ of values ranging from 1 to 0 for ranges ρ ranging from ρ_{min} to ρ_{max}, as defined in: .

$$c_R(\rho) = \frac{\rho_{max}^2 - \rho^2}{\rho_{max}^2 - \rho_{min}^2} \tag{7.2}$$

where ρ_{min} and ρ_{max} are set depending on the laser scanner in use.

Both models of contribution express the contribution of the incidence angle and range on the measurement noise as a coefficient ranging from 1 to 0, where 1 means the measurement is reliable and 0 indicates a not reliable measurement. In this thesis, a measurement is considered reliable when the quality of the acquisition is good. In Chapter 5, the scanning geometry is further investigated in practical situations.

7.1.4 How does the scanning geometry affects the total point cloud quality in practice?

Chapter 5 answers this question by putting the original approach presented in Chapter 4 in practice. The effect of scanning geometry is quantified and tested on a reference test board and two point clouds sampling a standard closed room. The quantification of the scanning geometry contribution on the quality of individual points is demonstrated on scans of reference test boards placed at various incidence angles and ranges from the

TLS. It is shown that the theoretical models presented in Chapter 4 are consistent with this experimental assessment. The total point cloud error is defined as the mean patch variance for all patches considered in the scene. The investigation of the incidence angle effect showed that for the particular small room setting presented, the contribution of incidence angles to the noise budget decreases by approximately ~ 20% per point when the scanner is moved from one viewpoint located in the middle of the room to another viewpoint with on average more favorable incidence angles. Accordingly, it is shown that it is possible to reduce the total error of the measurements by placing the scanner at another position in the room, which is not necessarily an obvious placement. Using our approach, it shown that an optimization of the measurement set-up can be achieved. An example of such optimization process is presented in Chapter 6.

7.1.5 How can negative effects of the scanning geometry on the point quality be mitigated?

Chapter 6 answers this question by presenting a new method that determines near optimal view-points in a scene based on terrestrial laser scanner capabilities. First, a visibility algorithm is presented, which enables the determination of the area visible per considered view-point. The presented work used a simple 2D Cartesian gridding of the room to determine possible view-point locations. Based on every visibility polygon calculated for each possible view-point, a Greedy algorithm is used to determine a set of view-points that covers the entire scene. It is shown that by integrating the constraints of the scanning geometry influences as presented in Chapter 4 in a survey planning, the positions of the view-points can be on forehand localized to capture scans of the surroundings with good quality. From the results presented in Chapter 5, the theoretical number of points decreases dramatically for patch orientations greater than 70°. The constraints on the incidence angles are therefore set to a maximum of 70°. As the laser scanner in use for this study was the FARO LS880, the range constraint is set to the maximum measurable range, which is 80 m. The influence of an incidence angle constraint and of a range limitation is shown on two simulated rooms. Using this simple approach, an improvement of the measurement set-up can be easily achieved using a small amount of computations, memory and time.

7.2 Recommendations and future work

7.2.1 Research on other influencing factors

The methods developed in this study to quantify the contribution of the scanning geometry to the measurement noise will also make it easier to investigate other noise components. Adequate corrections of these other influencing factors, such as the surface properties, the atmospheric conditions and instrument calibration, should provide users with measurements of better quality.

Tests performed for this research should ideally be repeated using other reference surfaces with known reflectance behavior such as the Spectralon diffuse reflectance targets. Such tests could help to characterize the error behavior of a specific scanner with respect to reference materials and lead to a possible correction model adequate to that specific laser scanner. As a longer term research, the error behavior due to surface properties should be investigated in more detail, focusing on the physical properties of the laser beam (wavelength, pulse or phase based measurements).

A closer analysis of the correlation on the single point spherical measurements (θ,φ,ρ) is interesting. Currently, these single point measurements are assumed to be uncorrelated and well calibrated. However the spherical raw measurements are expected to be correlated.

The investigation on the received intensity and the possible correlation with respect to noise level is expected to provide a better understanding of the noise behavior. Currently the intensity measurement is not a standard calibrated product. The airborne laser scanning technique already makes use of the scanning geometry to correct accordingly the received intensity measurements. One could think of applying similar methods to terrestrial laser scanners. It is however known to be a rather difficult process as the raw intensity measurement is generally not provided, but a rescaled intensity measurement.

7.2.2 Investigate other TLS models

The presented models are investigated mainly by using the scanners Leica HDS6000 and FARO LS880 HE80. The currently presented range effect model is dependent on the used laser scanner model. This range effect parametrization could be optimized and made independent of the scanner model. Optimizing these parameters will require larger surveys involving different types of scanners.

7.2.3 Propagate point cloud quality to end-products

The propagation of the point cloud quality into further processing steps is expected to provide an end-product of better quality. One way could be to utilize the contribution coefficients derived in this thesis in processing steps such as segmentation or registration as a weighting coefficient per point to improve the final result quality. In this way, points acquired with a good quality could play a bigger role in the process. Another way could be to make use of the total error of a point cloud in the assessment of an end-product quality.

7.2.4 Evaluate measurement biases

Biases are deviations from a true value. The source of biases in laser scanning point cloud come from any of the four presented quality influencing factors. A bias can be device dependent as well as user dependent and surroundings dependent. The evaluation of biases in terrestrial laser scanners is an interesting research topic.

7.2.5 Improve view-point placement algorithm

In this work, a greedy approach was used to select near optimal view-points that cover the scene. Other set-coverage algorithms could provide better view-points that are better distributed in the scene, using *e.g.* least-squares optimization techniques.

Another application of view-point placement algorithm is to define a quality standard from which the measurement set-up will be derived. This threshold could for instance specify the desired maximum standard deviation achieved from a viewpoint.

Currently, the presented method uses a 2D discretized map of the scene at the height of the laser scanner. A possible extension of this method would be to consider the full 3D room and define the 3D visibility from a view-point. The integration of several realistic scanner heights would improve the determination of the optimal view-points.

An adaptive grid to the level of detail required per surface would improve the determination of the best view-points. Moreover, a finer grid would avoid view-points positions too close to each other, but it will be at the expense of longer processing times.

The presented method handles the incidence constraint and the range constraints as two uncorrelated factors. However, in practice these constraints are closely related. A combined constraint will provide a visibility from a view-point that is more realistic.

7.3 Future directions

At the time this research started, terrestrial laser scanners were mainly being used by research institutes and manufacturers. However, nowadays, terrestrial laser scanners are present in almost every field of work, *e.g.* forensics, architecture, civil engineering, gaming industry, movie industry. Mobile mapping systems, such as scanners capturing a scene while driving a car, or scanners mounted on drones are currently making use of the same range determination techniques used in terrestrial laser scanners. The number of applications that make use of 3D point clouds is rapidly growing. The need for a sound quality product is even more significant as it impacts the quality of a huge panel of end-products.

Bibliography

[1] Abbas, M. A., Lichti, D. D., Chong, A. K., Setan, H., and Majid, Z. (2014). An on-site approach for the self-calibration of terrestrial laser scanner. *In Measurement: Journal of the International Measurement Confederation*, volume 52:111–123.

[2] Adams, M. D. and Probert, P. J. (1996). The interpretation of phase and intensity data for AMCW light detection sensors for reliable ranging. *In International Journal of Robotics Research*, volume 15(5):441–458.

[3] Alda, J. (2003). *Laser and Gaussian Beam Propagation and Transformation*. Encyclopedia of Optical Engineering.

[4] Anonymous (2004). *Pacific Island Hydrology Course, 3 - Levelling and Surveying*. NIWA, Fiji.

[5] Anonymous (2013). *Chapter 5 - Encoder Primer*. NASA , Infrared Telescope Facility - Telescope Control System.

[6] Antova, G. (2015). Registration process of laser scan data in the field of deformation monitoring. *In Procedia Earth and Planetary Science*, volume 15:549–552.

[7] Arguelles-Fraga, R., Ordonez, C., Garcia-Cortes, S., and Roca-Pardinas, J. (2013). Measurement planning for circular cross-section tunnels using terrestrial laser scanning. *In Automation in Construction*, volume 31:1–9.

[8] Arora, S. and Barak, B. (2009). *Computational Complexity: A Modern Approach*. Cambridge University Press.

[9] Baatz, M. and Schape, A. (2000). Multiresolution segmentation: An optimization approach for high quality multi-scale image segmentation. In *Proceedings of the AGIT 2000*.

[10] Bae, K., Belton, D., and Lichti, D. (2005). A framework for position uncertainty of unorganised three-dimensional point clouds from near-monostatic Laser Scanners using covariance analysis. In *Proceedings of the ISPRS Workshop, Laser Scanning 2005*, volume 36, pages 7–12.

[11] Bae, K.-H. and Lichti, D. (2007). An on-site self-calibration method using planar targets for terrestrial laser scanners. In *Proceedings of the ISPRS Workshop, Laser Scanning 2007 and SilviLaser 2007*, volume 36-3/W52, pages 14–19.

[12] Baltsavias, E. P. (1999). Airborne Laser Scanning: Basic relations and formulas. *In ISPRS Journal of Photogrammetry and Remote Sensing*, volume 54:199–214.

[13] Beland, R. R. (1993). Propagation through atmospheric optical turbulence. *In Atmospheric Propagation of Radiation*, volume 2:157–232.

[14] Berg, M. d., Cheong, O., Kreveld, M. v., and Overmars, M. (2008). *Computational Geometry: Algorithms and Applications*. 3rd rev, Springer-Verlag.

[15] Besl, P. J. and McKay, N. D. (1992). A method for registration of 3D shapes. *In IEEE Transactions on Pattern Analysis and Machine Intelligence*, volume 14(2):239–256.

[16] Boehler, W., Heinz, G., and Marbs, A. (2001). The potential of non-contact close range laser scanners for cultural heritage recording. In *Proceedings of the International Symposium of CIPA*.

[17] Boehler, W., Heinz, G., Marbs, A., and Siebold, M. (2002). 3D scanning software - An introduction. In *Proceedings of the International Workshop on Scanning for Cultural Heritage Recording*.

[18] Borah, D. K. and Voelz, D. G. (2007). Estimation of Laser beam pointing parameters in the presence of atmospheric turbulence. *In Applied Optics*, volume 46(23):6010–6018.

[19] Bottino, A., Laurentini, A., and Rosano, L. (2007). A tight lower bound for art gallery sensor location algorithms. In *Proceedings of the IEEE Conference on Emerging Technologies and Factory Automation, 2007. ETFA.*, pages 434–440.

[20] Brown, O. W. and Hugenholtz, C. H. (2013). Quantifying the effects of terrestrial laser scanner settings and survey configuration on land surface roughness measurement. *In Geosphere*, volume 9(2):367–377.

[21] Bucksch, A., Lindenbergh, R., and van Ree, J. (2007). Error budget of Terrestrial Laser Scanning: Influence of the intensity remission on the scan quality. In *Proceedings of the GeoSiberia - 2007*, volume 1, pages 113–122.

[22] Chan, T. O. and Lichti, D. D. (2012). Cylinder-based self-calibration of a panoramic terrestrial laser scanner. *In International Archives of the Photogrammetry, Remote Sensing and Spatial Information Sciences*, volume 39-B5:169–174.

[23] Chan, T. O., Lichti, D. D., and Belton, D. (2015). A rigorous cylinder-based self-calibration approach for terrestrial laser scanners. *In ISPRS Journal of Photogrammetry and Remote Sensing*, volume 99:84–99.

[24] Cheok, G. S., Leigh, S., and Rukhin, A. (2002). *Technical report: Calibration experiments of a Laser Scanner*. National Institute of Standards and Technology.

[25] Chow, J. C. K., Lichti, D. D., Glennie, C., and Hartzell, P. (2013). Improvements to and comparison of static terrestrial lidar self-calibration methods. *In Sensors (Switzerland)*, volume 13(6):7224–7249.

[26] Chvatal, V. (1975). A combinatorial theorem in plane geometry. *In Combinatorial Theory*, volume 18(1):39–41.

[27] Chvatal, V. (1979). A greedy heuristic for the set-covering problem. *In Mathematics of Operations Research*, volume 4(3):233–235.

[28] Cifuentes, R., van der Zande, D., Salas, C., Farifteh, J., and Coppin, P. (2014). Correction of erroneous lidar measurements in artificial forest canopy experimental setups. *In Forests*, volume 5(7):1565–1583.

[29] Coren, F. and Sterzai, P. (2006). Radiometric correction in laser scanning. *In International Journal of Remote Sensing*, volume 27(15):3097 – 3104.

[30] Cormen, T., Leiserson, C., Rivest, R., and Stein, C. (2001). *Introduction To Algorithms*. MIT Press.

[31] Couto, M. C., de Souza, C. C., and De Rezende, P. J. (2007). An exact and efficient algorithm for the orthogonal art gallery problem. In *Proceedings of the Brazilian Symposium on Computer Graphics and Image Processing*, pages 87–94.

[32] Cuartero, A., Armesto, J., Rodriguez, P. G., and Arias, P. (2010). Error analysis of terrestrial laser scanning data by means of spherical statistics and 3D graphs. *In Sensors*, volume 10(11):10128–10145.

[33] Danson, F. M., Hetherington, D., Morsdorf, F., Koetz, B., and Allgower, B. (2007). Forest canopy gap fraction from terrestrial laser scanning. *In Geoscience and Remote Sensing Letters, IEEE*, volume 4(1):157–160.

[34] De Asis Lopez, F., Garcia-Cortes, S., Roca-Pardinas, J., and Ordonez, C. (2014a). Geometric optimization of trough collectors using terrestrial laser scanning: Feasibility analysis using a new statistical assessment method. *In Measurement: Journal of the International Measurement Confederation*, volume 47:92–99.

[35] De Asis Lopez, F., Ordonez, C., Roca-Pardinas, J., and Garcia-Cortes, S. (2014b). Point cloud comparison under uncertainty. application to beam bridge measurement with terrestrial laser scanning. *In Measurement: Journal of the International Measurement Confederation*, volume 51(1):259–264.

[36] Dorninger, P. and Nothegger, C. (2007). 3D segmentation of unstructured point clouds for building modelling. In *Proceedings of the ISPRS Working Group - Photogrammetric Image Analysis*, volume 34-3/W49A, pages 191–196.

[37] Dorsch, R. G., Husler, G., and Herrmann, J. M. (1994). Laser triangulation: fundamental uncertainty in distance measurement. *In Applied Optics*, volume 33(7):1306–1314.

[38] Du, Q. and Fowler, J. E. (2008). Low-complexity principal component analysis for hyperspectral image compression. *In International Journal of High Performance Computing Applications*, volume 22(4):438–448.

[39] Eggert, D. W., Lorusso, A., and Fisher, R. B. (1997). Estimating 3D rigid body transformations: a comparison of four major algorithms. *In Machine Vision and Applications*, volume 9(5):272–290.

[40] Eltner, A. and Baumgart, P. (2015). Accuracy constraints of terrestrial lidar data for soil erosion measurement: Application to a mediterranean field plot. *In Geomorphology*, volume 245:243–254.

[41] Erdem, U. M. and Sclaroff, S. (2006). Automated camera layout to satisfy task-specific and floor plan-specific coverage requirements. *In Computer Vision and Image Understanding*, volume 103(3):156–169.

[42] Fan, L., Powrie, W., Smethurst, J., Atkinson, P. M., and Einstein, H. (2014). The effect of short ground vegetation on terrestrial laser scans at a local scale. *In ISPRS Journal of Photogrammetry and Remote Sensing*, volume 95:42–52.

[43] Fan, L., Smethurst, J. A., Atkinson, P. M., and Powrie, W. (2015). Error in target-based georeferencing and registration in terrestrial laser scanning. *In Computers and Geosciences*, volume 83:54–64.

[44] Faro (2015). Laser Scanners Techsheets. Available online: http://www.faro.com/ (Techsheet Accessed in June 2015).

[45] Fisher, M. A. and Bolles, R. C. (1981). RANdom SAmple Consensus: A Paradigm for model fitting with applications to image analysis and automated cartography. *In Communications of the ACM*, volume 24(6):381–395.

[46] Friis, H. T. (1946). A note on a simple transmission formula. *In Proceedings of the IRE*, volume 34(5):254–256.

[47] Garcia-San-Miguel, D. and Lerma, J. (2013). Geometric calibration of a terrestrial laser scanner with local additional parameters: An automatic strategy. *In ISPRS Journal of Photogrammetry and Remote Sensing*, volume 79:122–136.

[48] Gold, P. O., Cowgill, E., Kreylos, O., and Gold, R. D. (2012). A terrestrial lidar-based workflow for determining three-dimensional slip vectors and associated uncertainties. *In Geosphere*, volume 8(2):431–442.

[49] Golub, G. H. and Loan, C. v. (1980). An Analysis of the Total Least Squares Problem. *In SIAM Journal on Numerical Analysis*, volume 17(6):883–893.

[50] Gonzalez-Banos, H. and Latombe, J.-C. (2001). A randomized art-gallery algorithm for sensor placement. In *Proceedings of the Symposium on Computational Geometry*, pages 232–240, 378674.

[51] Gordon, S., Lichti, D., Franke, J., and Stewart, M. (2004). Measurement of structural deformation using Terrestrial Laser Scanners. In *Proceedings of the FIG International Symposium on Engineering Surveys for Construction Works and Structural Engineering*.

[52] Gordon, S. J. and Lichti, D. D. (2004). Terrestrial laser scanners with a narrow field of view: The effect on 3D resection solutions. *In Survey Review*, volume 37(292):448–468.

[53] Gordon, S. J. and Lichti, D. D. (2007). Modeling Terrestrial Laser Scanner data for precise structural deformation measurement. *In Surveying Engineering*, volume 133(2):72–80.

[54] Gori, F., Folino, G., Jetten, M. S. M., and Marchiori, E. (2011). MTR: taxonomic annotation of short metagenomic reads using clustering at multiple taxonomic ranks. *In Bioinformatics*, volume 27(2):196–203.

[55] Gorte, B. (2007). Planar feature extraction in Terrestrial Laser Scans using gradient based range image segmentation. In *Proceedings of the ISPRS Workshop, Laser Scanning 2007 and SilviLaser 2007*, volume 36, pages 173–177.

[56] Gorte, B., Khoshelham, K., and Verbree, E. (2008). Indoor navigation by using segmentation of range images obtained by Laser Scanners. In *Proceedings of the ISPRS Congress, Silk Road for Information from Imagery*, volume 37, page 971.

[57] Gosliga, R. v., Lindenbergh, R., and Pfeifer, N. (2006). Deformation analysis of a bored tunnel by means of Terrestrial Laser Scanning. In *Proceedings of the ISPRS Commission V Symposium, Image Engineering and Vision Metrology*, volume 36-5.

[58] Grant, D., Bethel, J., and Crawford, M. (2012). Point-to-plane registration of terrestrial laser scans. *In ISPRS Journal of Photogrammetry and Remote Sensing*, volume 72:16–26.

[59] Gronwall, C., Steinvall, O., Gustafsson, F., and Chevalier, T. (2007). Influence of laser radar sensor parameters on range-measurement and shape-fitting uncertainties. *In Optical Engineering*, volume 46(10):106201–11.

[60] Gruen, A. and Akca, D. (2005). Least squares 3D surface and curve matching. *In International Archives of the Photogrammetry, Remote Sensing and Spatial Information Sciences*, volume 59(3):151–174.

[61] Hartley, R. and Zisserman, A. (2003). *Multiple view geometry in computer vision, 2nd edition*. Cambridge University Press, Cambridge, UK.

[62] Hebert, M. and Krotkov, E. (1992). 3D measurements from imaging Laser radars: How good are they? *In Image and Vision Computing*, volume 10:170–178.

[63] Hejbudzka, K., Lindenbergh, R., Soudarissanane, S., and Humme, A. (2010). Influence of atmospheric conditions on the range distance and number of returned points in leica scanstation 2 point clouds. In *Proceedings of the ISPRS Commission V Mid-Term Symposium on Close Range Image Measurement Techniques*, volume 38, pages 282–287.

[64] Hesse, C. and Kutterer, H. (2006). *Automated Form Recognition of Laser Scanned Deformable Objects*, volume 131, pages 103–111. Springer Berlin Heidelberg.

[65] Hoefle, B. and Pfeifer, N. (2007). Correction of Laser Scanning intensity data: Data and model-driven approaches. *In International Archives of the Photogrammetry, Remote Sensing and Spatial Information Sciences*, volume 62(6):415–433.

[66] Hoffmann, F., Kaufmann, M., and Kriegel, K. (1991). The art gallery theorem for polygons with holes. In *Proceedings of the Symposium on Foundations of Computer Science*, pages 39–48.

[67] Holst, C., Artz, T., and Kuhlmann, H. (2014). Biased and unbiased estimates based on laser scans of surfaces with unknown deformations. *In Journal of Applied Geodesy*, volume 8(3):169–183.

[68] Jelalian (1992). *Laser Radar Systems*. Artech House.

[69] Kaasalainen, S., Ahokas, E., Hyyppa, J., and Suomalainen, J. (2005). Study of surface brightness from backscattered Laser intensity calibration of Laser data. *In IEEE Geoscience and Remote Sensing Letters*, volume 2(3):255–259.

[70] Kaasalainen, S., Hyyppa, J., Litkey, P., Hyyppa, H., Ahokas, E., Kukko, A., and Kaartinen, H. (2007). Radiometric calibration of ALS intensity. In *Proceedings of the ISPRS Workshop, Laser Scanning 2007 and SilviLaser 2007*, volume 36.

[71] Kaasalainen, S., Krooks, A., Kukko, A., and Kaartinen, H. (2009). Radiometric calibration of terrestrial laser scanners with external reference targets. *In Remote Sensing*, volume 1(3):144–158.

[72] Karp, R. M. (1972). *Reducibility Among Combinatorial Problems*, pages 219–241. Springer Berlin Heidelberg.

[73] Kawashima, K., Yamanishi, S., Kanai, S., and Date, H. (2014). Finding the next-best scanner position for as-built modeling of piping systems. *In International Archives of the Photogrammetry, Remote Sensing and Spatial Information Sciences*, volume 40-5:313–320.

[74] Kersten, T. P., Mechelke, K., Sterberg, H., and Acevedo Pardo, C. (2004). Terrestrial Laserscanning System Mensi GS100/GS200 - Accuracy tests, experiences and projects at the Hamburg University of Applied Sciences. In *Proceedings of the ISPRS Workshop on Panoramic Photogrammetry Workshop*, volume 34, page 8.

[75] Kersten, T. P., Sternberg, H., and Mechelke, K. (2005). Investigations into the accuracy behaviour of the Terrestrial Laser Scanning system MENSI GS100. In *Proceedings of the Optical 3D Measurement Techniques*, volume I, pages 122–131.

[76] Kremen, T., Koska, B., and Pospsil, J. (2006). Verification of Laser Scanning systems quality. In *Proceedings of the FIG Congress, Shaping the Change*, volume 1.

[77] Krooks, A., Kaasalainen, S., Hakala, T., and Nevalainen, O. (2013). Correction of intensity incidence angle effect in terrestrial laser scanning. In *Proceedings of the ISPRS Workshop, Laser Scanning 2013*, volume 2, pages 145–150.

[78] Kukko, A., Kaasalainen, S., and Litkey, P. (2008). Effect of incidence angle on laser scanner intensity and surface data. *In Applied Optics*, volume 47(7):986–992.

[79] Labsphere (2014). Labsphere spectralon diffuse reflectance standards.

[80] Lague, D., Brodu, N., and Leroux, J. (2013). Accurate 3D comparison of complex topography with terrestrial laser scanner: Application to the Rangitikei canyon (N-Z). *In ISPRS Journal of Photogrammetry and Remote Sensing*, volume 82:10–26.

[81] Landa, Y., Tsai, R., and Cheng, L.-T. (2006). Visibility of point clouds and mapping of unknown environments. In *Proceedings of the Advanced Concepts for Intelligent Vision Systems*, volume 1, pages 1014–1025.

[82] Landes, T., Boulaassal, H., and Grussenmeyer, P. (2012). Quality assessment of geometric facade models reconstructed from TLS data. *In Photogrammetric Record*, volume 27(138):137–154.

[83] Lay, D. C. (2002). *Linear Algebra and Its Applications (3rd edition)*. Addison-Wesley.

[84] Leader, J. C. (1979). Analysis and prediction of Laser scattering from rough-surface materials. *In Optical Society of America (1917-1983)*, volume 69:610–628.

[85] Leica (2015a). Laser Scanners Techsheets. Available online: http://www.leica-geosystems.com/ (Techsheet Accessed in June 2015).

[86] Leica (2015b). Leica laser distance meters. Available online: http://www.leica-geosystems.us/ (Techsheet Accessed in June 2015).

[87] Li, W. X. and Mitchell, L. D. (1995). Laser Scanning system testing – Errors and improvements. *In Measurement: Journal of the International Measurement Confederation*, volume 16(2):91–101.

[88] Lichti, D. D. (2004). A resolution measure for Terrestrial Laser Scanners. In *Proceedings of the ISPRS Congress, Geo-Imagery Bridging Continents*, volume 35, pages 216–221.

[89] Lichti, D. D. (2007). Error modelling, calibration and analysis of an AM CW Terrestrial Laser Scanner system. *In International Archives of the Photogrammetry, Remote Sensing and Spatial Information Sciences*, volume 61(5):307–324.

[90] Lichti, D. D. (2008). A method to test differences between additional parameter sets with a case study in Terrestrial Laser Scanner self-calibration stability analysis. *In International Archives of the Photogrammetry, Remote Sensing and Spatial Information Sciences*, volume 63(2):169–180.

[91] Lichti, D. D. (2010). Terrestrial laser scanner self-calibration: Correlation sources and their mitigation. *In ISPRS Journal of Photogrammetry and Remote Sensing*, volume 65(1):93–102.

[92] Lichti, D. D., Chow, J., and Lahamy, H. (2011). Parameter de-correlation and model-identification in hybrid-style terrestrial laser scanner self-calibration. *In International Archives of the Photogrammetry, Remote Sensing and Spatial Information Sciences*, volume 66(3):317–326.

[93] Lichti, D. D. and Gordon, S. J. (2004). Error propagation in directly georeferenced Terrestrial Laser Scanner point clouds for cultural heritage recording. In *Proceedings of the FIG Working Week - The Olympic Spirit in Surveying*.

[94] Lichti, D. D. and Harvey, B. R. (2002). The effects of reflecting surface properties on time-of-flight Laser scanner measurements. In *Proceedings of the CIG Annual Geomatics Conference*.

[95] Lichti, D. D. and Jamtsho, S. (2006). Angular resolution of Terrestrial Laser scanners. *In Photogrammetric Record*, volume 21(114):141–160.

[96] Lichti, D. D., Jamtsho, S., El-Halawany, S. I., Lahamy, H., Chow, J., Chan, T. O., and El-Badry, M. (2012). Structural deflection measurement with a range camera. *In Journal of Surveying Engineering*, volume 138(2):66–76.

[97] Lichti, D. D. and Licht, M. G. (2006). Experiences with Terrestrial Laser Scanner modelling and accuracy assesment. In *Proceedings of the ISPRS Commission V Symposium, Image Engineering and Vision Metrology*, volume 36, pages 155–160.

[98] Lindenbergh, R., Pfeifer, N., and Rabbani, T. (2005). Accuracy analysis of the Leica HDS3000 and Feasibility of Tunnel Deformation monitoring. In *Proceedings of the ISPRS Workshop, Laser Scanning 2005*, volume 36, pages 24–29.

[99] Lindenbergh, R. C., Soudarissanane, S. S., De Vries, S., Gorte, B. G., and De Schipper, M. A. (2011). Aeolian beach sand transport monitored by terrestrial laser scanning. *In Photogrammetric Record*, volume 26(136):384–399.

[100] Milenkovic, M., Pfeifer, N., and Glira, P. (2015). Applying terrestrial laser scanning for soil surface roughness assessment. *In Remote Sensing*, volume 7(2):2007–2045.

[101] Mill, T., Ellmann, A., Aavik, A., Horemuz, M., and Sillamae, S. (2014). Determining ranges and spatial distribution of road frost heave by terrestrial laser scanning. *In Baltic Journal of Road and Bridge Engineering*, volume 9(3):225–234.

[102] Molnar, G., Pfeifer, N., Ressl, C., Dorninger, P., and Nothegger, C. (2009). On-the-job range calibration of terrestrial laser scanners with piecewise linear functions. *In Photogrammetrie-Fernerkundung-Geoinformation*, volume 2009(1):9–21.

[103] Nicodemus, F. E. (1965). Directional reflectance and emissivity of an opaque surface. *In Applied Optics*, volume 4(7):767–773.

[104] Nurunnabi, A., Belton, D., and West, G. (2014). Robust statistical approaches for local planar surface fitting in 3D laser scanning data. *In ISPRS Journal of Photogrammetry and Remote Sensing*, volume 96:106–122.

[105] Obermeyer, K. J. and Contributors (2008). The VisiLibity library. Available online: http://www.VisiLibity.org R-1.

[106] Obermeyer, K. J., Ganguli, A., and Bullo, F. (2010). Multi-agent deployment for visibility coverage in polygonal environments with holes. *In International Journal on Robust and Nonlinear Control*, volume 00:1–31.

[107] Okatani, I. S. and Deguchi, K. (2002). A method for fine registration of multiple view range images considering the measurement error properties. *In Computer Vision and Image Understanding*, volume 87:66–77.

[108] O'Rourke, J. (1987). *Art Gallery Theorems and Algorithms*. Oxford University Press, UK.

[109] Pal, N. R. and Pal, S. K. (1993). A review on image segmentation techniques. *In Pattern Recognition*, volume 26(9):1277–1294.

[110] Paquet, R. (2003). A method to predict accuracy of matching in least squares surface matching. In *Proceedings of the ISPRS Workshop, 3D reconstruction from airborne laserscanner and InSAR data*, volume 34-3/W13.

[111] Park, H. S., Lee, H. M., Adeli, H., and Lee, I. (2007). A new approach for health monitoring of structures: Terrestrial laser scanning. *In Computer-Aided Civil and Infrastructure Engineering*, volume 22(1):19–30.

[112] Pejic, M. (2013). Design and optimisation of laser scanning for tunnels geometry inspection. *In Tunnelling and Underground Space Technology*, volume 37:199–206.

[113] Pejic, M., Ogrizovic, V., Bozic, B., Milovanovic, B., and Marosan, S. (2014). A simplified procedure of metrological testing of the terrestrial laser scanners. *In Measurement: Journal of the International Measurement Confederation*, volume 53:260–269.

[114] Pesci, A. and Teza, G. (2008). Effects of surface irregularities on intensity data from laser scanning: an experimental approach. *In Annals of Geophysics*, volume 51(5/6):839–848.

[115] Pfeifer, N. and Briese, C. (2007). Laser scanning - principles and applications. In *Proceedings of the GeoSiberia - 2007*, pages 93–112.

[116] Pfeifer, N., Dorninger, P., Haring, A., and Fan, H. (2007). Investigating Terrestrial Laser Scanning intensity data: quality and functional relations. In *Proceedings of the International Conference on Optical 3-D Measurement Techniques VIII*, pages 328–337.

[117] Pfeifer, N., Hofle, B., Briese, C., Rutzinger, M., and Haring, A. (2008). Analysis of the backscattered energy in Terrestrial Laser Scanning data. In *Proceedings of the ISPRS Congress, Silk Road for Information from Imagery*, volume 37, pages 1045–1051.

[118] Pfeifer, N., Oude Elberink, S., and Filin, S. (2005). Automatic tie elements detection for laser scanner strip adjustment. In *Proceedings of the ISPRS Workshop, Laser Scanning 2005*, volume 36-3/W19, pages 174–179.

[119] Proakis, J. and Salehi, M. (2002). *Communication Systems Engineering*. Prentice Hall.

[120] Pu, S. and Vosselman, G. (2009). Knowledge based reconstruction of building models from terrestrial laser scanning data. *In ISPRS Journal of Photogrammetry and Remote Sensing*, volume 64(6):575–584.

[121] Rabbani, T., van den Heuvel, F. A., and Vosselman, G. (2006). Segmentation of point cloud using smoothness constraint. In *Proceedings of the ISPRS Commission V Symposium, Image Engineering and Vision Metrology*, volume 36-5, pages 248–253.

[122] Rade, L. and Westergren, B. (2005). *Mathematics handbook for science and engineering*. Birkhauser Boston, international 5th edition.

[123] Reed, M. K. and Allen, P. K. (1999). 3D modeling from range imagery: An incremental method with a planning component. *In Image and Vision Computing*, volume 17(2):99–111.

[124] Rees, W. G. (2001). *Physical Principles of Remote Sensing*. Scott Polar Research Institute, Cambridge.

[125] Rieger, P. (2014). Range ambiguity resolution technique applying pulse-position modulation in time-of-flight scanning lidar applications. *In Optical Engineering*, volume 53(6):061614.

[126] Riegl (2014). Laser Scanners Techsheets. Available online: http://www.riegl.com/ (Techsheet Accessed in November 2014).

[127] Roca-Pardinas, J., Arguelles-Fraga, R., de Asis Lopez, F., and Ordonez, C. (2014). Analysis of the influence of range and angle of incidence of terrestrial laser scanning measurements on tunnel inspection. *In Tunnelling and Underground Space Technology*, volume 43:133–139.

[128] Roggero, M. (2002). Object segmentation with region growing and principal component analysis. In *Proceedings of the ISPRS Symposium, Photogrammetric Computer Vision*, volume 34-3A/B, pages 289–194.

[129] Rosser, N. J., Petley, D. N., Lim, M., Dunning, S., and Allison, R. J. (2005). Terrestrial laser scanning for monitoring the process of hard rock coastal cliff erosion. *In Quarterly Journal of Engineering Geology and Hydrogeology*, volume 38(4):363–375.

[130] Rousseeuw, P. J. and Hubert, M. (2011). Robust statistics for outlier detection. *In Wiley Interdisciplinary Reviews: Data Mining and Knowledge Discovery*, volume 1(1):73–79.

[131] Rusu, R. B. and Cousins, S. (2011). 3D is here: Point Cloud Library (PCL). In *Proceedings of the IEEE International Conference on Robotics and Automation (ICRA)*.

[132] Salo, P., Jokinen, O., and Kukko, A. (2008). On the calibration of the distance measuring component of a Terrestrial Laser Scanner. In *Proceedings of the ISPRS Congress, Silk Road for Information from Imagery*, volume 37, pages 1067–1073.

[133] Salvi, J., Matabosch, C., Fofi, D., and Forest, J. (2006). A review of recent range image registration methods with accuracy evaluation. *In Image and Vision Computing*, volume 25:578–596.

[134] Santala, J. and Joala, V. (2003). On the calibration of a ground-based Laser scanner. In *Proceedings of the FIG Working Week - Still on the Frontline*.

[135] Santolaria, J., Guillomia, D., Cajal, C., Albajez, J., and Aguilar, J. (2009). Modelling and calibration technique of laser triangulation sensors for integration in robot arms and articulated arm coordinate measuring machines. *In Sensors*, volume 9(9):7374–7396.

[136] Schaefer, T., Weber, T., Kyrinovic, P., and Zamecnikova, M. (2004). Deformation measurement using Terrestrial Laser Scanning at the hydropower station of Gabcikovo. In *Proceedings of the INGEO 2004 and FIG Regional Central and Eastern European Conference on Engineering Surveying*.

[137] Schaer, P., Skaloud, J., Landtwing, S., and Legat, K. (2007). Accuracy estimation for Laser point cloud including Scanning geometry. In International Archives of Photogrammetry, Remote Sensing and Spatial Information Sciences, editor, *Proceedings of the Mobile Mapping Symposium*, volume 36.

[138] Schrijver, A. (1986). *Theory of linear and integer programming*. John Wiley and Sons, Inc.

[139] Schulz, T. and Ingensand, H. (2004). Terrestrial Laser Scanning - investigations and applications for high precision Scanning. In *Proceedings of the FIG Working Week - The Olympic Spirit in Surveying*.

[140] Sheng, Y. (2008). Quantifying the size of a lidar footprint: A set of generalized equations. *In IEEE Geoscience and Remote Sensing Letters*, volume 5(3):419–422.

[141] Silfvast, W. (2004). *Laser Fundamentals*. Cambridge University Press.

[142] Sithole, G. and Mapurisa, W. (2012). 3D object segmentation of point clouds using profiling techniques. *In South African Journal of Geomatics*, volume 1(1).

[143] Skeen, J. P. E. (2011). *TxDOT Survey Manual*. Texas Department of Transportation, Texas.

[144] Slavik, P. (1996). A tight analysis of the greedy algorithm for set cover. In *Proceedings of the Association for Computing Machinery Symposium on Theory of Computing*, volume 1, pages 435–441, 237991.

[145] Soudarissanane, S. and Lindenbergh, R. (2011). Optimizing terrestrial laser scanning measurement set-up. In *Proceedings of the ISPRS Workshop, Laser Scanning 2011*, volume 38.

[146] Soudarissanane, S., Lindenbergh, R., and Gorte, B. (2008). Reducing the error in Terrestrial Laser Scanning by optimizing the measurement set-up. In *Proceedings of the ISPRS Congress, Silk Road for Information from Imagery*, volume 37, pages 615–620.

[147] Soudarissanane, S., Lindenbergh, R., Menenti, M., and Teunissen, P. (2009). Incidence angle influence on the quality of terrestrial laser scanning points. In *Proceedings of the ISPRS Workshop, Laser Scanning 2009*, volume 38, pages 183–188.

[148] Soudarissanane, S., Lindenbergh, R., Menenti, M., and Teunissen, P. (2011). Scanning geometry: Influencing factor on the quality of terrestrial laser scanning points. *In International Archives of the Photogrammetry, Remote Sensing and Spatial Information Sciences*, volume 66(4):389–399.

[149] Soudarissanane, S., Van Ree, J., Bucksch, A., and Lindenbergh, R. (2007). Error budget of Terrestrial Laser Scanning: influence of the incidence angle on the scan quality. In *Proceedings of the 3D-NordOst 2007*, pages 73–81.

[150] Stewart, M. P., Penna, N. T., and Lichti, D. D. (2005). Investigating the propagation mechanism of unmodelled systematic errors on coordinate time series estimated using least squares. *In Geodesy*, volume 79:479–489.

[151] Tan, K. and Cheng, X. (2015). Intensity data correction based on incidence angle and distance for terrestrial laser scanner. *In Journal of Applied Remote Sensing*, volume 9(1):094094.

[152] Taylor, J. (1997). *An Introduction Error Analysis: The Study of Uncertainties in Physical Measurements*. Univ Science Books.

[153] Teunissen, P. (2001). GNSS ambiguity bootstrapping: theory and application. In *Proceedings of the International Symposium on Kinematic Systems in Geodesy, Geomatics and Navigation*, pages 246–254.

[154] Teunissen, P. J. G. (2000a). *Adjustment theory*. Delft University Press, Delft, The Netherlands.

[155] Teunissen, P. J. G. (2000b). *Testing theory*. Delft University Press, Delft, The Netherlands.

[156] Tomas, A. P., Bajuelos, A. L., and Marques, F. (2006). On visibility problems in the plane – solving minimum vertex guard problems by successive approximations. In *Proceedings of the International Symposium on Artificial Intelligence and Mathematics*, volume 1, pages 1–12.

[157] Torre de la, F. and Black, M. J. (2003). Robust principal component analysis for computer vision. *In Computer Vision and Image Understanding*, volume 91:53–71.

[158] Tozoni, D., de Rezende, P., and de Souza, C. (2013). *The Quest for Optimal Solutions for the Art Gallery Problem: A Practical Iterative Algorithm*, volume 7933 of *Lecture Notes in Computer Science*, chapter 29, pages 320–336. Springer Berlin Heidelberg.

[159] Van Goor, B., Lindenbergh, R., and Soudarissanane, S. (2011). Identifying corresponding segments from repeated scan data. In *Proceedings of the ISPRS Workshop, Laser Scanning 2011*, volume 38.

[160] Vanhaekendover, H., Lindenbergh, R., Ngan-Tillard, D., Slob, S., and Wezenberg, U. (2014). Deterministic in-situ block size estimation using 3D terrestrial laser data. In *Proceedings of the ISRM European Regional Symposium on Rock Engineering and Rock Mechanics: Structures in and on Rock Masses, EUROCK 2014*, pages 989–993. Taylor and Francis - Balkema.

[161] Vosselman, G. and Maas, H. G. (2010). *Airborne and Terrestrial Laser Scanning*. Whittles Publishing, Dunbeath, Scotland, UK.

[162] Wagner, W., Ullrich, A., Ducic, V., Melzer, T., and Studnicka, N. (2006). Gaussian decomposition and calibration of a novel small-footprint full-waveform digitising airborne laser scanner. *In International Archives of the Photogrammetry, Remote Sensing and Spatial Information Sciences*, volume 60(2):100–112.

[163] Wang, G., Zheng, B., Li, X., Houkes, Z., and Regtien, P. P. L. (2002). Modelling and calibration of the laser beam-scanning triangulation measurement system. *In Robotics and Autonomous Systems*, volume 40(4):267–277.

[164] Watt, P. J. and Donoghue, D. N. M. (2005). Measuring forest structure with terrestrial laser scanning. *In International Journal of Remote Sensing*, volume 26(7):1437–1446.

[165] Wehr, A. and Lohr, U. (1999). Airborne laser scanning - an introduction and overview. *In International Archives of the Photogrammetry, Remote Sensing and Spatial Information Sciences*, volume 54:68–82.

[166] Weichel, H. (1990). *Laser beam propagation in the atmosphere*. Tutorial texts in optical engineering. SPIE Optical Engineering Press, Bellingham, Washington, USA. Includes bibliographical references (p. 89-98).

[167] Zeibak, R. and Filin, S. (2007). Change detection via Terrestrial Laser Scanning. In *Proceedings of the ISPRS Workshop, Laser Scanning 2007 and SilviLaser 2007*, volume 36-3/W52, pages 430–435.

[168] Zhuang, H. and Roth, Z. S. (1995). Modeling gimbal axis misalignments and mirror center offset in a single-beam Laser tracking measurement system. *In International Journal of Robotics Research*, volume 14(3):211–224.

[169] Zitova, B. and Jan, F. (2003). Image registration methods: a survey. *In Image and Vision Computing*, volume 21:977–1000.

Curriculum Vitæ

Sylvie Shoba Soudarissanane (Dijkstra)

21-04-1983	Born in Orléans, France.

Education

2007-2015	Delft University of Technology (TU Delft) *Delft, The Netherlands* PhD in Geoscience and Remote Sensing department, Civil Engineering and Geosciences Faculty
2005-2007	Chalmers University of Technology *Göteborg, Sweden* Master's degree in Digital Communication Systems and Technology
2003-2007	Ecole Supérieure d'Ingénieurs en Electrotechnique et Electronique (ESIEE-Paris) *Noisy Le Grand, France* Master's degree in Electronic Engineering
2001-2003	Institut Universitaire Technologique (IUT) en Génie Electrique Informatique Industrielle (GEII) *Lieusaint, France* Bachelor's degrees in Industrial Network Management (RLI) and Electronics and Electrical Power (EEP) Double degree, both awarded with distinction
1998-2001	Lycée Militaire d'Autun *Autun, France* Degree awarded with merit (mention)

Work experience

2013-present	Nederlandse Organisatie voor Toegepast Natuurwetenschappelijk Onderzoek (TNO) *The Hague, The Netherlands* Scientist Innovator in Network Technology

PhD Community

2010-2011	PromooD President *Delft, The Netherlands* Chair(wo)man of the independent representative body of the 2000 PhD candidates at the Delft University of Technology (TU Delft)
2010-2011	PromooD Board member *Delft, The Netherlands* Board member Internal and Legal Affairs

Publications

Journal papers

S. Soudarissanane, R. Lindenbergh, M. Menenti and P. Teunissen, Scanning geometry: Influencing factor on the quality of terrestrial laser scanning points. In: ISPRS Journal of Photogrammetry and Remote Sensing, 2011. Volume 66, Issue 4, p.11.

R. Lindenbergh, S. Soudarissanane, S. de Vries, B. Gorte, M. de schipper. Eolian beach sand transport monitored by terrestrial laser scanning, In: Photogrammetric Record, 2011. Volume 26, Issue 136, p.384-399.

C. van der Sande, S. Soudarissanane and K. Khoshelham, Assessment of relative accuracy of AHN - 2 laser scanning data using planar features. In: Sensors, 2010. Volume 10, Issue 9, p.8198-8214 (First and second author are both having the same level of contribution in this paper. Because this paper suits the field of work of C. van Sande, we agreed to place him as first author.)

Conference Proceedings

S. Soudarissanane, R. Lindenbergh, Optimizing Terrestrial Laser Scanning Measurement set-up, In: Proc. of the IASPRS, LS 2011, Calgary, Canada. (2011)

K, Hejbudzka, R. Lindenbergh, S. Soudarissanane, A. Humme. Influence of atmospheric conditions on the range distance and number of returned points in Leica scanstation 2 point clouds, In: Proc. of the ISPRS Commission V Mid-Term Symposium on Close Range Image Measurement Techniques, XXXVIII, p.282-287. (2010)

R. Lindenbergh, S. Soudarissanane, S. de Vries, M. Coquet, M. de Schipper, K. Hejbudzka, K. Duijnmayer, B. van Goor, A. Cohen. Eolian Sand Transport Monitored By Terrestrial Laser Scanning, In: Proc. of the ISPRS Commission V Mid-Term Symposium on Close Range Image Measurement Techniques, XXXVIII, p.393-398. (2010)

S. Soudarissanane, C. van der Sande and K. Khoshelham, Accuracy assessment of airborne laser scanning strips using planar features, Presented at EUROCOW 2010: the International Calibration and Orientation Workshop, 10-12 February 2010, Castelldefels, Spain. (2010)

S. Soudarissanane, R. Lindenbergh, M. Menenti and P. Teunissen. Incidence angle influence on the quality of Terrestrial Laser Scanning points. In Proc. of the ISPRS Workshop, Laser Scanning 2009. Paris, France. (2009)

S. Soudarissanane; R. Lindenbergh; B. Gorte. Reducing the error in terrestrial laser scanning by optimizing the measurement set-up, In Proc. of the XXIst ISPRS Congress: Commission V, WG 3, Beijing, People's Republic of China, p.615-620. (2008) **[Best Poster Award.]**

S. Soudarissanane, J. van Ree, A. Bucksch and R. Lindenbergh. Error budget of terrestrial laser scanning: influence of the incidence angle on the scan quality. In: Proceedings 3D-NordOst, Berlin, Germany. (2007)